Chondrule-like objects and a Ca-Al-rich inclusion from comets or comet-like icy bodies

Takaaki Noguchi[a, *], Daisuke Nakashima[b,c], Takayuki Ushikubo[d,c], Wataru Fujiya[e], Noriaki Ohashi[f,e], John P. Bradley[g], Tomoki Nakamura[b], Noriko T. Kita[c], Peter Hoppe[h], Hidemi Ishibashi[i], Makoto Kimura[j], and Naoya Imae[j]

[a]Division of Earth and Planetary Science, Kyoto University, Kitashirakawaoiwake-cho, Sakyo-ku, Kyoto 606-8502, Japan

[b]Department of Earth Science, Tohoku University, 6-3 Aoba, Aramaki, Aoba-ku, Sendai 980-8578, Japan

[c]WiscSIMS, Department of Geoscience, University of Wisconsin-Madison, 1215 W Dayton St. Madison WI 53706, USA

[d]Kochi Institute for Core Sample Research, Japan Agency for Marine-Earth Science and Technology (JAMSTEC), 200 Monobe Otsu, Nankoku, Kochi 783-8502, Japan

[e]Earth Science Course, College of Science, Ibaraki University, 2-1-1 Bunkyo, Mito 310-8512, Japan

[f]NEC Networks and System Integration Corporation, Iidabashi First Tower, 2-6-1 Koraku, Bunkyo-ku, Tokyo 112-8560, Japan

[g]Hawaii Institute of Geophysics and Planetology, the University of Hawaii at Manoa, Honolulu, HI 96822, USA

[h]Particle Chemistry Department, Max Planck Institute for Chemistry, Hahn-Meitner-Weg 1, 55128 Mainz, Germany

[i]Department of Geoscience, Shizuoka University, 836, Ohya, Suruga-ku, Shizuoka 422-8529, Japan.

[j]National Institute of Polar Research, 10-3 Midori-cho, Tachikawa, Tokyo 190-8518, Japan.

*Corresponding author name: Takaaki Noguchi (noguchi.takaaki.2i@kyoto-u.ac.jp)

ABSTRACT

Chondrules and Ca-Al-rich inclusions (CAIs) have been considered characteristic constituents of chondritic meteorites, although the outward transportation of CAIs has been theoretically pointed out. Stardust samples recovered by the Stardust mission from the 81P/Wild2 comet contained chondrule-like objects (CLOs) and refractory inclusions that include CAIs and amoeboid olivine aggregates (AOAs). However, it was not proven that the CLOs, AOAs, and CAIs coexist with fine-grained materials equivalent to chondritic porous interplanetary dust particles (CP IDPs) containing abundant glass with embedded metal and sulfides (GEMS). Here we report on two type II CLOs, containing <90 Mg# in ferromagnesian silicates, enclosed in GEMS-rich CP Antarctic micrometeorites (AMMs) (CP IDPs that reached the surface of the Earth) and one igneous object rich in kosmochloric (Ko-rich: $NaCrSi_2O_6$-rich) high-Ca pyroxene and Fe-bearing olivine (KOOL) that is enclosed in a CP IDP. KOOL grains have also been found in Stardust samples and CP IDPs. These three igneous objects are embedded in fine-grained matrices that do not show any evidence of aqueous alteration. The low Mg# and elevated $\Delta^{17}O$ of olivine and pyroxene in these CLOs and the KOOL grain are consistent with previously studied CLOs from comet 81P/Wild 2 and a giant cluster IDP. These results support the view that CP IDP- and CP AMM-like

materials constitute samples from comets or comet-like icy bodies. The CLOs were formed in oxidizing environment beyond the snow line and then transferred to the comet-forming region. In contrast, a spinel-hibonite (SHIB) fragment found in an AMM experienced aqueous alteration of its rim. The SHIB fragment contains ultrarefractory oxides and refractory metal nuggets and has a ^{26}Mg excess like typical meteoritic CAIs. The mineralogy of the fine-grained matrix is very similar to CP IDPs and CP AMMs. However, because "GEMS" in the matrix lacks Fe-Ni metal and amorphous silicate in it contains Fe, it is clear that the matrix weakly experienced aqueous alteration. Olivine / (Olivine + low-Ca pyroxene) ratios in the matrices of the four samples range from 0.4 to 0.6, which are comparable with those of anhydrous CP IDPs and CP MMs (around 0.5), and those of P- and D-type asteroids and Jupiter-family comets (around 0.5).

Keywords

Chondrules, CAI, oxygen isotopes, isotope anomalies, GEMS

1. INTRODUCTION

The NASA Stardust mission revealed that the comet 81P/Wild 2 belonging to Jupiter family comets (JFCs) contains refractory grains including Ca-Al-rich inclusions (CAIs), amoeboid olivine aggregates (AOAs), Al-rich chondrules, and chondrules (Zolensky et al., 2006; McKeegan et al., 2006; Simon et al., 2008; Nakamura et al., 2008; Matzel et al., 2010; Joswiak et al., 2012, 2014, and 2017; Ogliore et al., 2012).

The refractory inclusions and chondrules are one of the major constituents of chondritic meteorites. Most refractory inclusions were probably formed by condensation from gas with a roughly solar composition at temperatures >1350 K, depending on the total pressures and their bulk chemical composition (e.g., Alexander et al., 2022), and some experienced melting and crystallization. Although there are constraints on where they formed, it likely was in the protoplanetary disk, close to the Sun. Chondrules are estimated to have formed by melting pre-existing dust aggregates at peak temperatures of ~1700–2100 K in the protoplanetary disk (e.g., Hewins and Radomsky, 1990).

The main characteristics of the refractory grains and chondrules returned by Stardust are described below. The CAI, Inti, is composed of anorthite, Al- and Ti-rich high-Ca pyroxene (fassaite), spinel, and mellite with minor osbornite and perovskite (Joswiak et al., 2017), and its ^{16}O-rich isotopic composition with $\delta^{18}O \approx \delta^{17}O = -40‰$ is similar to meteoritic

CAIs (Simon et al., 2008). The refractory grain, Coki, is composed of anorthite with minor spinel, which does not show ^{26}Mg excess, suggesting later formation than the canonical CAIs (Matzel et al., 2010). Chondrules recovered by Stardust include both type I chondrules (containing olivine and pyroxene with ≥ 90 Mg# = 100 × Mg / [Mg+Fe]) and type II chondrules (containing olivine and pyroxene with < 90 Mg#). Type II chondrules are more abundant than type I chondrules (e.g., Nakamura et al., 2008; Gainsforth et al., 2015). The relationship between $\Delta^{17}O = \delta^{17}O - 0.52 \times \delta^{18}O$ and Mg# of olivine and pyroxene is similar to the chondrule minerals in CR chondrites (e.g., Nakamura et al., 2008; Nakashima et al., 2012b; Defouilloy et al., 2017). Their presence in cometary material indicates a large-scale outward transport of inner solar system material to the cold outer solar system region where cometary nuclei formed (>30 au) (e.g., Ciesla, 2007).

Previous studies suggest that the cometary materials may contain these objects. A considerable number of CAIs and related mineral fragments as well as an amoeboid olivine aggregate (AOA) have been reported as constituents of anhydrous interplanetary dust particles (IDPs) and anhydrous Antarctic micrometeorites (AMMs), thought to be of cometary origins (e.g., Christoffersen and Buseck, 1986; Zolensky, 1987; McKeegan, 1987; Joswiak et al., 2017; Greshake et al., 1996; Engrand et al., 1999). The CAIs contained some

of the following minerals: diopsidic high-Ca pyroxene, spinel, anorthite, Al- and Ti-rich high-Ca pyroxene (fassaite), perovskite, hibonite, gehlenite-rich melilite, corundum, and with/without forsterite ± enstatite rim. An amoeboid olivine aggregate (AOA) contained forsterite, anorthite, ± spinel, and high-Ca pyroxene. The mineralogies of these CAIs are similar to fluffy Type A CAIs containing abundant melilite, spinel, perovskite, high-Ca pyroxene, and subordinate hibonite (e.g., Brearley and Jones, 1998 and references therein). Still, the grain sizes of the constituent minerals are much smaller than those in fluffy CAIs in meteorites. Chondrule-like objects were also identified in giant cluster IDPs (e.g., Zhang et al., 2021) and an AMM containing abundant GEMS (glass with embedded metal and sulfide) (Noguchi et al., 2017). Furthermore, the presence of crystalline silicates in comets and the outer parts of protoplanetary disks has already hinted at a large-scale outward transport of inner disk material to the cold outer disk region (e.g., Nuth et al., 2000; Bockelee-Morvan et al., 2002; Keller and Gail, 2004).

Anhydrous chondritic porous ("CP") IDPs recovered from the stratosphere have been regarded as cometary dust. However, it has not yet been proven whether they are of cometary origin (e.g., Davidson et al., 2012). CP IDPs contain abundant GEMS, which appear as 100-500 nm-sized spheroidal objects composed of amorphous silicate containing nanometer-sized

Fe-Ni metal and sulfide (Bradley, 2014; Ishii et al., 2008). Unfortunately, it is unclear whether the samples returned from 81P/Wild 2 comet contain GEMS (Ishii et al. 2008). GEMS-like objects in the fine-grained debris abutting terminal particles are likely deceleration debris during the capture of 81P/Wild 2 particles in aerogel, although there is no isotopic data (Ishii, 2019).

Mid-infrared (MIR) spectroscopic studies of asteroids and comets led some researchers to dispute this conventional point of view on the origins of CP IDPs and their equivalent AMMs (e.g., Vernazza et al., 2015; 2017; 2021). They proposed that pyroxene-rich CP IDPs were derived from low-density B-, C-, and G-type (hereafter BCG-type) asteroids instead of JFCs. They argued that such asteroids may have a pyroxene-rich CP IDP-like crust and an aqueously altered interior. Vernazza et al. (2015) argued that olivine-rich IDPs may originate from JFCs and P- and D-type (hereafter PD-type) asteroids. However, it is known that olivine-rich (olivine class) IDPs are a diverse collection of genetically different IDPs (Christoffersen and Buseck, 1986). Despite these problems, CP IDPs originating from icy asteroids is a viable hypothesis.

In this study, we report on two CP AMMs (CP IDPs that reached the Earth's surface: Noguchi et al., 2015), one CP IDP containing chondrule-like objects (CLOs), an igneous

object without any evidence of aqueous alteration, and a weakly hydrated CP AMM containing a refractory inclusion referred to as a hybrid IDP (e.g., Germani et al. 1990, Rietmeijer 1991; Nakamura et al. 2005) that reached the surface of the earth. As described above, consensus on the building blocks of JFC, BCG-type, and PD-type asteroids has yet to be realized. The comparison between olivine and low-Ca pyroxene ratios in the matrices of the four samples and the ratios of these minerals in the celestial bodies described above may enable more definitive determination of the provenance of CP IDPs/AMMs to particular classes of asteroids and comets. The discussion may also contribute to the discussion on the occurrence of CLOs and refractory inclusions in these bodies.

2. MATERIALS AND METHODS

2.1 Samples

About 200 AMMs have been recovered from ~200 kg of surface snow near the Dome Fuji Station collected in 2003 and 2005. Because the Dome Fuji Station stands on the crest of an ice dome (altitude 3810 m), the highest temperature is below –30 ^{o}C and the annual mean snow precipitation is ~10 cm/year (Kameda et al., 2008). The low temperature prevents

AMMs from suffering significant terrestrial weathering, and the low precipitation rate concentrates AMMs relative to terrestrial dust. We melted the snow and filtered the water in a clean room (class 1000). The highest temperature during snow melting was well below 10 ^{o}C, which helped minimize the alteration of the AMMs during isolation (Noguchi et al., 2022). We collected AMMs larger than ~25-μm in diameter from the residues on the Isopore membrane filter®. Identification of AMMs was based on their morphologies and chemical composition. We used a JEOL JSM-5600LV scanning electron microscope (SEM) with an Oxford ISIS 300 energy dispersive spectrometer (EDS) at Ibaraki University to characterize the AMMs. It operated at 15 kV acceleration voltage and ~0.3 nA beam current on the probe current detector. We also observed six IDPs collected in 1997 by the same SEM-EDS, and the IDP L2036 #20 that contains an igneous object.

2.2 Ultramicrotomy

Three AMMs, D03IB64, D05IB66, D05IB84, and an IDP L2036 #20, were embedded in epoxy resin and ultramicrotomed into ~100-nm ultrathin sections using a Reichert Ultracut N ultramicrotome at Ibaraki University. D05IB66 was ultramicrotomed at Kyushu University.

For the first three samples, we used Gilder HEX TEM grids with thin formvar support films. After retrieving the ultrathin sections onto the TEM grids, the grids were thinly coated with carbon to prevent degradation of the formvar in the electron beam. For D05IB66, we used LAAD 100-mesh grids with 100-nm-thick carbon support films.

2.3 SEM observation of the cross-sections of the samples

The potted butts (remainder after ultramicrotomy) were observed by field-emission scanning electron microscopes (FE-SEM) equipped with EDS at the University of Tokyo and Kyushu University. We performed electron backscatter diffraction (EBSD) mapping to confirm the common crystallographic relationships among the “bars” of olivine in D03IB64 using the FE-SEM at the University of Tokyo.

2.4 (Scanning) transmission electron microscopy

The ultrathin sections of all four samples were investigated using JEOL JEM-2000FX TEM equipped with EDAX DX4 EDS at Ibaraki University, scanning (S)TEMs Thermo Fisher Scientific Tecnai G2 20F TEM equipped with EDAX Exact Genesis EDS at Kyushu University, JEOL JEM-ARM 200F equipped with JEOL JED-2300T EDS at Kyushu

University, and a Super STEM Titan (Thermo Fisher Scientific) with EDAX Genesis EDX at Laurence Livermore Laboratory. The quantitative analyses of minerals were performed using the Cliff-Lorimer method using Tecnai G2 20F. K factors for Na, Mg, Al, P, S, K, Ca, Ti, Mn, Cr, Fe, and Ni for silicates and those for Fe and Ni for metal and sulfide were experimentally determined using many mineral standards including synthetic kosmochlor for k_{NaSi}, olivine from Miyakejima, Japan for k_{MgSi}, adularia from St. Gotthard, Switzerland for K_{AlSi} and K_{AlSi}, apatite from Durango, Mexico for k_{PCa} ($k_{PSi} = k_{PCa} \times k_{CaP}$), haüyne from Niedermendig, Germany for k_{SSi}, titanite from Tormiq Valley, Pakistan for k_{CaSi} and k_{TiSi}, synthetic tephroite for k_{MnSi}, olivine from DSDP Hole 735B for k_{FeSi}, synthetic Ni olivine for k_{NiSi}, troilite in Cape York iron meteorite for k_{FeS}, and millerite from Sarany, Russia for k_{NiS}. Typical detection limits of these elements are ~0.1wt.%.

2.5 Electron microprobe analysis

The chemical compositions of minerals and glass in the coarse-grained objects in the four samples were determined using a field emission electron microprobe analyzer (FE-EPMA) JEOL JXA-8530F at Kyushu University. We selected a 12 kV acceleration voltage and 6 nA on the probe current detector for silicates to minimize the X-ray excitation volume

during analysis, enabling chemical compositions from the small areas (~2 μm in diameter) to be determined. The measurement time for each analysis was ~6 minutes. ZAF oxide correction was used for quantitative analysis. The standards for Na, Mg, Al, Si, P, S, K, Ca, Ti, Mn, and Fe were commercial standards, MINM25-53 Mineral Mount, purchased from ASTIMEX Science Ltd. The standard for Ni was also a commercial standard purchased from JEOL Co. Ltd. The standard for Cr was synthetic Cr_2O_3. The detection limits of SiO_2, TiO_2, Al_2O_3, Cr_2O_3, FeO, NiO, MnO, MgO, CaO, Na_2O, K_2O, P_2O_5, Y_2O_3, ZrO_2, and V_2O_3 are 0.09, 0.21, 0.09, 0.18, 0.24, 0.24, 0.22, 0.10, 0.12, 0.08, 0.11, 0.12, 0.45, 0.17, and 0.18wt.%, respectively. The EPMA control software resolved the overlapping correction factors for V and Ti.

The chemical compositions of Fe-Ni sulfides in the coarse-grained objects in D03IB66, D05IB66, and L2036#20 were obtained using a FE-EPMA JEOL JXA-iHP200F at the Institute of Space and Astronautical Science, Japan Aerospace Exploration Agency. We also selected 12 kV acceleration voltage and 1 nA for sulfide analysis on the probe current detector. The low acceleration voltage reduced the excitation volume, which enabled us to obtain chemical compositions from the small areas (~2 μm in diameter). The measurement time for each analysis was ~2 minutes. ZAF metal correction was used for quantitative analysis. The

standard for Fe and Ni was Invar36 alloy; the standards for Co and S were commercial standards purchased from Micro-Analysis Consultants Ltd. Sulfur, Fe, Co, and Ni detection limits are 0.02, 0.09, 0.10, and 0.10 wt.%, respectively.

2.6 Re-embedding the potted butts and preparation of the polished samples

After electron microprobe analysis, the potted butts of D03IB64, D05IB84, and L2036 #20 were re-embedded in epoxy along with a San Carlos olivine crystal (the standard for oxygen isotopic analysis at the WiscSIMS laboratory). And the potted butt of D05IB66 was embedded in epoxy resin without an olivine standard. Each potted butt was carefully polished manually until the ultramicrotomed surface was once again exposed on the polished surface. After polishing, each potted butt was cut into 2-mm-thick epoxy discs (6 or 8 mm in diameter) to fit the sample holder of the SIMS instrument.

2.7 SIMS oxygen isotopic analysis

Three 6-mm epoxy disks containing the samples D03IB64, D05IB84, and L2036 #20 were mounted in a custom-made sample holder (25 mm in diameter) with seven holes (each 6 mm in diameter). This setup has been shown to minimize the surface topography effects in

high-precision SIMS stable isotope analyses of cometary particles (Nakashima et al., 2011). The oxygen isotope analyses of the three samples were performed using a CAMECA IMS-1280 ion microprobe at the University of Wisconsin-Madison (Valley and Kita, 2009; Kita et al., 2009). The three samples were analyzed in two separate sessions: D03IB64 and D05IB84 in the 1st session and L2036 #20 in the 2nd session. The analytical conditions and measurement procedures were similar to those of Nakamura et al. (2008) and Nakashima et al. (2012a, b). We used a focused $^{133}Cs^{+}$ primary beam accelerated to a total of 20 keV, set to ~1.5 μm × 2.5 μm and intensity of ~11 pA in the 1st session, and ~2 μm × 3 μm and intensity of ~3 pA in the 2nd session. The 10 keV secondary O^{-} ions were detected simultaneously using the multi-collection system with one Faraday Cup (for $^{16}O^{-}$) and two electron multipliers (EM, for $^{17}O^{-}$ and $^{18}O^{-}$ on an axial detector and multi-collection array, respectively). The mass resolving powers were set to ~5,000 (at 10% height) for the axial EM detecting $^{17}O^{-}$ to eliminate the interference from $^{16}OH^{-}$ and ~2,200 (at 10% height) for the other detectors. The total analytical time per spot was about 30 minutes, including pre-sputtering (8 min), automatic retuning of the secondary beam (2 min), and analysis (counting time for 60 sec × 20 cycles; 20 min). A typical count rate for $^{16}O^{-}$ was ~ 1×10^{7} cps in the 1st session and 5×10^{6} cps in the 2nd session. All sample analyses were bracketed by a total

of 6 spot analyses on San Carlos olivine grains ($\delta^{18}O_{VSMOW}$ = 5.32‰ in Kita et al., 2010) that were mounted in the epoxy disks within 1 mm of the samples to correct instrumental bias on the oxygen isotope ratio analyses. The analytical 2SD uncertainties of bracketing standard analyses are 1.2 - 2.0‰ in $\delta^{18}O$, 0.9 - 1.4‰ in $\delta^{17}O$, and 0.5 - 1.2‰ in $\Delta^{17}O$ (Table S1). This external reproducibility is assigned as the uncertainty of the sample analyses. The contribution of the tailing of $^{16}OH^-$ interference to $^{17}O^-$ signal was corrected by the method described in Heck et al. (2010), though the contribution was negligibly small (≤ 0.5‰). We analyzed two olivines (Fo_{100} and Fo_{60}), two low-Ca pyroxenes (En_{97} and En_{85}), diopside, glass, hibonite, and spinel standards in the same sessions for correction of matrix-dependent instrumental bias of olivine, high-Ca pyroxene, glass, and spinel (Valley and Kita, 2009; Kita, et al., 2010). The instrumental biases estimated from the above mineral standards (matrix effect) are within a few ‰ in $\delta^{18}O$. After the SIMS analysis, the analyzed points were inspected by FE-SEM at the University of Tokyo. One out of the five analyses of D05IB84 AMM and five out of eleven analyses of L2036#20 IDP were rejected because they overlapped with perovskite, sulfide, and glass, which induce instrumental mass fractionation and depress the $^{16}O^-$ count rates.

The oxygen isotope analyses of D05IB66 AMM were performed using a CAMECA

IMS-1280HR ion microprobe at Kochi Institute for Core Sample Research, JAMSTEC. A focused Cs^+ primary beam was set to 3 μm × 2 μm and an intensity of ~20 pA. The field aperture was set at 2 mm × 2 mm, corresponding to 10 μm × 10 μm for the field of view of the secondary ion image. Other parameters of the instrument were the same as described above. The total analytical time per spot was about 9 minutes, including pre-sputtering (30 sec), automatic retuning of the secondary beam (40 sec), and analysis (counting time for 8 sec × 50 cycles; 400 sec). A typical count rate for $^{16}O^-$ was 1.1-1.5 × 10^7 cps. The same San Carlos olivine and pyroxene standards (En_{97}, En_{85}, and diopside, Table EA2-2 in Kita et al., 2010) were measured for the matrix corrections. After the SIMS analysis, the analyzed points were verified by FE-SEM observation at Kyushu University.

2.8 SIMS Al-Mg isotopic analysis

After oxygen isotopic analysis, D05IB084 was polished again carefully to obtain a flat surface. Al-Mg isotope analyses were performed using a CAMECA 1280 SIMS at the University of Wisconsin-Madison. For the SIMS Al-Mg isotope analyses of Al-rich phases, overlapping analysis areas with adjacent Mg-rich phases would result in several analytical problems, including lower $^{27}Al/^{24}Mg$ ratios and reduction of excess ^{26}Mg, inaccurate

instrumental bias corrections, and potential artifacts from the quasi-simultaneous arrival (QSA) effect (Slodzian et al., 2004). To avoid hitting adjacent different phases, we employed FIB (focused ion beam) marking at the selected locations of CAIs before the SIMS analyses, using procedures described in Nakashima et al. (2012b). A Zeiss 1500XB CrossBeam workstation equipped with a gallium ion source at the University of Wisconsin was used to remove the surface coating (carbon coating ~ 20 nm) from both unknown and standard mounts. A 30 keV focused Ga^+ ion beam of 5 pA was scanned within a 1 μm × 1 μm square on the sample surface for 120 sec, so only the surface coating was removed without significant milling of minerals from the sample surface. This 1 μm square region was later identified by secondary $^{27}Al^+$ ion imaging in SIMS before Al-Mg isotope analysis.

Magnesium isotope ratios and $^{27}Al/^{24}Mg$ ratios of spinel and hibonite in CAIs were analyzed. The analytical conditions and measurement procedures were generally similar to those in Nakashima et al. (2012b) and Nakashima et al. (2015), otherwise described below. The 6-mm epoxy disk containing the CAI was mounted in the 7-hole disk used for oxygen isotope analyses in this study (see above). Before each Al-Mg isotope analysis, secondary $^{27}Al^+$ ion images of FIB squares were obtained using an O^- ion beam of ~2 μm diameter (~3 pA) that was scanned over an area of 10 μm × 10 μm. The primary beam was set as Köhler

illumination mode with mass and beam apertures of 20 μm and 100 μm diameters, respectively. The secondary $^{27}Al^{+}$ ions were produced only from FIB squares, where the surface coating was removed and detected as scanning ion images using a fixed position mono-collector electron multiplier (mono-EM) at the ion optical axis. After recognizing the FIB square (within a few minutes of sputtering), we moved the stage to relocate the FIB square to the center of the 10 μm × 10 μm raster area where the Al-Mg isotope analysis was made. New 10 μm × 10 μm $^{27}Al^{+}$ ion images were taken after each SIMS analysis to confirm the positions of analyzed spots.

For Al-Mg isotope analysis, an O^{-} primary beam was set to ~2 μm and intensity of ~3-4 pA (same settings for $^{27}Al^{+}$ ion imaging) without raster. The primary beam size was set by the size of the mass aperture, which was initially 20 μm and enlarged during the analysis session as it was sputtered by intense O^{-} primary ions. The primary beam intensity was readjusted and kept constant at ~4 pA by changing the primary ion lens (L2) voltage before each spot analysis. The secondary $^{24}Mg^{+}$, $^{25}Mg^{+}$, $^{26}Mg^{+}$, and $^{27}Al^{+}$ ions were detected using the mono-EM in magnet peak switching mode. The intensities of $^{24}Mg^{+}$ and $^{27}Al^{+}$ were ~1 × 10^{5} cps and 2 × 10^{5} cps for spinel, and ~1 × 10^{4} cps and 2 × 10^{5} cps for hibonite, respectively. A single analysis took ~3.5 hours for spinel and 5 hours for hibonite, including 900 sec of

pre-sputtering to stabilize Mg ion intensity, ~60 sec for automatic centering of the secondary optics, and 200 cycles of switching between $^{24}Mg^{+}$, $^{25}Mg^{+}$, $^{26}Mg^{+}$, and $^{27}Al^{+}$ (counting times of 5, 20, 20, and 1 sec, respectively, with 2 sec waiting time) for spinel and 300 cycles for hibonite. The individual SIMS pits were carefully examined by FE-SEM for cracks and overlapping phases.

An isotope mass fractionation correction (instrumental and natural) was applied to the SIMS-measured Mg isotope ratios to estimate an excess ^{26}Mg (Ushikubo et al., 2013). The terrestrial Mg isotope ratios of ($^{25}Mg/^{24}Mg$) = 0.12663 and ($^{26}Mg/^{24}Mg$) = 0.13932 (Kita et al., 2012) are used as a reference for data reduction of the measured Mg isotope ratios. The fractionation-corrected $\delta^{26}Mg^{*}$ values were calculated using an exponential law with the coefficient $\beta = 0.514$ (Catanzaro et al., 1966) from the evaporation experiments of Schrader et al. (2008) using the following formula (Ushikubo et al., 2013):

$$\delta^{26}Mg^{*} = \delta^{26}Mg - [(1 + \delta^{25}Mg/1000)1/\beta - 1] \times 1000 \ (‰).$$

We analyzed terrestrial spinel and hibonite standards before and after the unknown sample analyses. Mg isotope ratios and $^{27}Al/^{24}Mg$ ratios between the FIB squares and regular

carbon coated areas are indistinguishable within analytical uncertainty, indicating that FIB marking does not cause any instrumental bias exceeding the analytical uncertainty (the spinel standard shows a variation in Mg isotope ratios, which is described later in detail). The relative sensitivity factors, RSF = $(^{27}Al/^{24}Mg)_{SIMS}/(^{27}Al/^{24}Mg)_{EPMA}$, were estimated using the spinel and hibonite standards. The reproducibility of the $^{27}Al/^{24}Mg$ ratios of the standard was 3% (2SD), which is propagated as uncertainty to those of $^{27}Al/^{24}Mg$ ratios of individual spot analyses (Table S1). The average and 2SE (= 2SD/√(n)) of $\delta^{26}Mg^{*}$ values of the hibonite standard are –0.34 ± 0.56‰ (n = 6; Table S1), and there is no significant mass independent instrumental fractionation on Mg isotope analyses of the hibonite standard beyond the analytical uncertainty. The spinel standard shows a significant mass-independent instrumental fractionation, showing negative bias on measured $\delta^{26}Mg^{*}$ values from –3‰ to –6‰ (Table S1; Fig. S1). Because we found the negative bias was due to the QSA effect (Slodzian et al., 2004) on the spinel data, we corrected them according to the method described in the supplementary material.

During the analysis of the 2nd spot of the hibonite in the refractory inclusion in D05IB84, we observed a drop of $^{27}Al/^{24}Mg$ ratio (from 30 to 10), accompanied by an increase of Mg count rates (from 1×10^4 cps to 4×10^4 cps for ^{24}Mg), starting at the 142nd cycle of a

total of 300 cycles without a significant change of ^{27}Al count rates. In spinel, the Al_2O_3 content (71wt.%) is comparable to that in hibonite (82wt.%), but the MgO content (28wt.%) is ten times as large as that in hibonite (2.9wt.%). Therefore, the drop in the $^{27}Al/^{24}Mg$ ratio and increase in Mg count rates are probably caused by overlapping analysis areas with adjacent spinel when the SIMS pit was gradually enlarged. However, it is not evident from the SEM image. We removed the data of cycles with a reduced $^{27}Al/^{24}Mg$ ratio (cycles 142-300) from the finalized isotope ratios (Table S1).

2.9 NanoSIMS analysis to search for presolar grains

We analyzed the carbon, nitrogen, and oxygen isotopic compositions of the matrix of D03IB64 with the NanoSIMS 50 ion probe at the Max Planck Institute for Chemistry (Hoppe et al., 2013). The ultrathin sections of D03IB64 on a grid were attached to a special jig of 1/2 inch in diameter, which was subsequently mounted into a standard NanoSIMS sample holder.

In the C- and N-isotope analyses, we simultaneously recorded secondary ion images (256 × 256 pixels) of $^{12}C^-$, $^{13}C^-$, $^{12}C^{14}N^-$, $^{12}C^{15}N^-$, and $^{28}Si^-$, produced by scanning a Cs^+ primary ion beam (~1 pA, 100 nm in diameter) over 5 × 5 to 25 × 25 μm^2 areas in a multi collection mode. The mass resolving power was set such that $^{13}C^-$ and $^{12}C^{15}N^-$ were

sufficiently separated from isobaric interferences such as $^{12}CH^-$, $^{13}C^{14}N^-$, or $^{11}B^{16}O^-$. We acquired a series of four ion image planes for each ultrathin section and summed them up with drift correction among sequential ion images. The measurement time was approximately 45 minutes (10,000 μs per pixel and image plane). The bulk C and N isotopic compositions were calculated by integrating signals from regions of interest in ion images, which were selected by masking pixels with count rates lower than 10% of the highest count rate in the $^{12}C^-$ ion image. The total analyzed area was 352 μm^2. We used a doped silicon carbide standard with a known C isotopic composition to normalize the C isotopic compositions of D03IB64. The isotopic composition of the standard was assumed to be identical to that of the air. Hotspots with C and/or N isotopic anomalies with a significance of more than 4σ were identified from ion ratio images.

For the O isotope analyses, we simultaneously recorded secondary ion images (256 × 256 pixels) of $^{16}O^-$, $^{17}O^-$, $^{18}O^-$, $^{28}Si^-$, and $^{27}Al^{16}O^-$, produced by scanning a Cs^+ primary ion beam (~1 pA, 100 nm in diameter) over 4 × 4 to 6 × 6 μm^2 areas in multi collection mode. The mass resolving power was set such that $^{17}O^-$ was sufficiently separated from $^{16}OH^-$. We acquired a series of two ion image planes for each ultrathin section and summed them up with drift correction between these ion images. The measurement time was approximately

23 minutes (10,000 μs per pixel and image plane). The total analyzed area was 93 μm^2. We used the fine-grained matrix in Acfer 094, an ungrouped primitive chondrite, as a reference for normal isotopic compositions. We selected regions of interest in ion images by masking pixels with count rates lower than 10% of the highest count rate in the $^{16}O^-$ ion image.

3. RESULTS

3.1 Morphology and internal structure of the samples

Fig. 1 shows the morphology of the three AMMs and the one IDP investigated in this study. Their dimensions range from ~25 to ~50 μm across. These four samples' ultrathin (~100 nm thick) sections comprise coarse-grained objects and sub-μm-sized fine-grained porous matrices. However, the coarse-grained objects were broken into tiny shards. Most of them were lost during ultramicrotomy (Fig. 2). The detailed mineralogy of the porous fine-grained matrices will be described in section 3.7.

3.2 Petrography of the coarse-grained objects in the samples

Back-scattered electron (BSE) images of the coarse-grained (>10 μm across) igneous objects in two AMMs and one IDP, and the coarse-grained refractory object in an AMM are

shown in Fig. 3. Their irregular morphologies suggest that they are fragments of larger objects. The textures of the objects, including the presence of interstitial glass (Figs. 3a-c), are similar to meteoritic chondrules. These igneous objects are as small as microchondrules (e.g., Krot et al., 1997; Dobrică and Brearley, 2016; Suttle et al., 2019). However, their textures are considerably different from the igneous objects in this study. The texture of the igneous object in D05IB66 is similar to some of the agglomeratic chondrules (e.g., Schrader et al., 2018S). The term chondrule-like objects (CLOs) have been used for years to describe the igneous objects similar to our samples in the Stardust samples (Nakamura et al., 2008), the micrometeoroid recovered from the international space station (Noguchi et al., 2011), interplanetary dust particles (Zhang et al., 2021), and Ryugu samples (Nakamura et al., 2022; Nakashima et al., 2023). Therefore, to avoid the misconception that the igneous objects investigated in this study are entirely different from similar objects that have been described in the previous studies, we use the same terminology, CLOs in this study.

The texture of the CLO in the AMM D03IB64 (Fig. 3a) contains abundant skeletal olivine. Figure 4 compares a backscatter electron (BSE) image of a part of this CLO and the electron backscatter diffraction (EBSD) map of the corresponding area with pole-figure images of olivine. The skeletal olivine has the same crystallographic orientation and

comprises a single crystal. This igneous object has a thin olivine shell (Fig. 3a). Meteoritic barred olivine (BO) chondrules are composed of a few comb-like olivine single crystals that appear as parallel bars in the cross-sections with a continuous shell of olivine, which is a part of the comb-like olivine crystals (e.g., Lauretta et al. 2006). These features are common to this CLO, although the olivine in the object is skeletal rather than barred. Therefore, this CLO could be called a BO-like CLO. The olivine in this BO-like CLO is bright in the BSE image, suggesting Fe-rich. There are some voids in the object. A pyrrhotite grain exists on its surface. Sub-μm-sized chromian spinel crystals and a small amount of P- and Fe-enriched (up to ~32wt.% P_2O_5 and ~40wt.% FeO, with ~13wt.% SiO_2, ~6wt.% Al_2O_3, ~1wt.% CaO, ~5wt.% Na_2O, and ~2wt.% K_2O) amorphous material was sporadically found on the surface of the CLO. No phyllosilicate was identified in this section or its interior (ultrathin sections). A BO-like CLO has also been described in a giant cluster IDP (Zhang et al., 2021).

The CLO in the AMM D05IB66 (Fig. 3b) has a micro-porphyritic texture. This object can be classified as a POP CLO. Because only a small amount of interstitial glass exists between the olivine and low-Ca pyroxene crystals, the degree of melting of this CLO was likely low during its formation. The large (>10 μm across) low-Ca pyroxene crystals have dark cores and bright rims in the BSE image, suggestive of magnesian cores and ferroan rims.

In contrast, all olivine crystals are bright in the BSE image, suggesting Fe-rich. Pyrrhotite crystals are present on the surface of this POP CLO. No evidence of aqueous alteration was found in this CLO.

The igneous object in the IDP L2036 #20 shown in Fig. 3c also has a micro-porphyritic texture. This object contains abundant bright olivine and high-Ca pyroxene as seen in the BSE image, suggesting Fe-rich. Iron-nickel sulfide exists within and on the surface of the object. Therefore, this igneous object is similar to a POP CLO. However, because this igneous object contains Ko-rich ($NaCrSi_2O_6$-rich) high-Ca pyroxene, which will be described in section 3.4, we call it a KOOL grain here. KOOL grains are polycrystalline objects found in 81P/Wild2 samples and 8 CP IDPs, which are composed Ko-rich high-Ca pyroxene, Fe-rich olivine and additional phases such as Cr-rich spinel, aluminosilicate glass, and albitic plagioclase (Joswiak et al., 2009). No evidence of aqueous alteration was found in this object.

The coarse-grained object in the AMM D05IB84 (Fig. 3d) is a refractory inclusion. It comprises ~10-μm long hibonite laths and micro- to sub-micrometer-sized anhedral perovskite crystals, both enclosed in spinel. Its texture and the chemical compositions of individual phases are almost the same as that of spinel-hibonite-perovskite inclusions often found in CM chondrites (Ireland, 1988; Simon et al., 2006; Liu et al., 2009; Kööp et al.,

2016). This object can be called a SHIB (spinel-hibonite) fragment, according to Ireland (1988). Unlike CLOs and KOOL grain, a part of the SHIB fragment shows evidence of weak aqueous alteration: the replacement by phyllosilicate on its rim (Fig. 3d). The phyllosilicate will be described in section 3.6.

3.3 Bulk and glass chemical compositions of the two CLOs and the KOOL grain

Figure 5a shows the Si and CI chondrite normalized bulk elemental abundances of the two CLOs and the KOOL grain. For comparison, the ranges of the Si and CI chondrite normalized bulk elemental abundances of type I and type II chondrules in MET 00526 L/LL3.05 and MET 00426 CR2 chondrites (Berlin et al., 2009; Berlin et al., 2011), type II chondrules in PRE 95404 R3 chondrite (Miller et al., 2017), those of the KOOL grain Coki-A in the Stardust sample returned from 81P/Wild 2 comet and some IDPs (Joswiak et al., 2009) are also plotted. The elemental abundances of the CLOs and the KOOL grain were calculated from the chemical compositions of the minerals and glass and their modal abundances (Tables S2, S3). In the case of the CLO in D05IB66, we calculated its "bulk" elemental abundances in two ways: one includes, and the other excludes the large Mg-rich cores of the low-Ca pyroxene crystals, which have distinct oxygen isotopic compositions (see

section 3.7).

Similarly, Fig. 5b shows the Si and CI chondrite normalized elemental abundances of interstitial glass in these objects. For comparison, the ranges of the Si and CI chondrite normalized elemental abundances of igneous glass in type I and type II chondrules in MET 00526 L/LL3.05 and MET 00426 CR2 chondrites (Berlin et al., 2009; Berlin et al., 2011) and those of the KOOL grains (Joswiak et al., 2009) are also plotted for comparison.

The bulk elemental abundances of the two CLOs and the KOOL grain are almost within the ranges of meteoritic chondrules and KOOL grains (Fig. 5a). The elemental abundance patterns of the BO-like CLO and the KOOL grain are like each other. The bulk compositions of the BO-like CLO and the KOOL grain are within the ranges of type II chondrules in L/LL3.05, CR2, and R3, and KOOL grains (Fig. 5a). In contrast, the Na and K abundances in the POP CLO are much lower than those in the BO-like CLO and the KOOL grain, but within the ranges of the type II chondrules in L/LL3.05. However, its K abundance is slightly lower than the lowest range of the type II chondrules in L/LL3.05 (Fig. 5a). These differences may be related to the different modal abundances of the Na- and K-containing Si- and Al-rich interstitial glass between them. The modal abundances of the interstitial glass in the BO-like CLO and the KOOL grain are 33% and 47%, respectively. In contrast, the

modal abundance of the interstitial glass in the POP CLO is only 4% (it rises to only 6% even if the relict low-Ca pyroxene is excluded from the modal abundance calculation).

Sodium and K abundances in the interstitial glass in the two CLOs and the KOOL grain are almost within the range of meteoritic chondrules, as shown in Fig. 5b. The high Mg abundance in the glass of the BO-like CLO is probably the effect of the neighboring olivine crystals. Even the widest area of the interstitial glass is ~1 μm wide (Fig. 3a), which is smaller than the diameter of the X-ray activation volume, ~2 μm, using EPMA operated at 12 kV acceleration voltage.

3.4 Mineral chemistries of the two CLOs and the KOOL grain

Figures 6 and 7 show the major and minor element abundances in olivine and pyroxene in the two CLOs and the KOOL grain, as well as the matrix olivine and low-Ca pyroxene. The chemical compositions of three igneous objects were obtained using FE-EPMA (Table 1), and those in the fine-grained matrices were obtained using EDS in the (S)TEM. Because the chemical compositions of the matrix silicates are described in section 3.10, here we describe the chemical compositions of the three igneous objects.

Figure 6a shows a histogram of fayalite (Fa) mol% in olivine in the two CLOs and the

KOOL grain and that in the matrix olivines in all the samples investigated. Figure 6b shows a histogram of ferrosilite (Fs) mol% in low-Ca pyroxene in the POP CLO and the matrix pyroxenes in all the investigated samples. The BO-like CLO and the POP CLO contain homogeneous olivine with Fa_{22-23} (N=2) and that with Fa_{20-21} (N=5) (Fig. 6a). In contrast, low-Ca pyroxene in the POP CLO shows a wide compositional variation: cores with ~Wo_1~Fs_1 and rims with $Wo_{3-4}Fs_{12-16}$ (N=12) (Figs. 6a to c), where Wo means wollastonite (Wo) mol%. The KOOL grain contains homogeneous olivine with Fa_{29-31} (N=2). The high-Ca pyroxenes in it have $Wo_{34-41}En_{49-51}$ (N=3) (Fig. 6c). The high-Ca pyroxene contains about 15-25mol% of the Ko component (Fig. 6d). The MnO vs. FeO and Cr_2O_3 vs FeO diagrams show that olivine and low-Ca pyroxene in the two CLOs and KOOL grain are plotted within the compositional fields of olivine in CP and CS IDPs, the fine-grained matrices of primitive chondrites, and the Wild2 samples (Fig. 7).

Figure 8 shows the relationship between the molar Fe/Mg and Fe/Mn ratios of olivine in the two CLOs and the KOOL grain investigated in this study, those of olivine in two CLOs, Torajiro and Iris, and a KOOL Puki grain recovered from comet 81P/Wild2 by the Stardust mission (Nakamura et al., 2008; Gainsforth et al., 2015), those in CLOs and mineral fragments (MFs) in a giant cluster IDP U2-20GCA (Zhang et al., 2021), and those in a CLO

recovered from the International Space Station (ISS) (Noguchi et al., 2011). The compositional fields of olivine in type II chondrules in CM2s, CR2s, and L/LL3s (Schrader et al., 2015; Schrader and Davidson, 2017 and 2022) are also plotted for comparison.

Figure 9 shows the major element compositions of Fe-Ni sulfide in the two CLOs, the KOOL grain, and those in the matrices of the four samples. Because the chemical compositions of Fe-Ni sulfide in the matrices are described in section 3.5, here we describe the chemical compositions of the Fe-Ni sulfides in the three igneous objects. Most Fe-Ni sulfides in the BO-like CLO contain <3 atomic% Ni except for a grain with ~10 atomic% Ni. The Fe-Ni sulfides in the POP CLO contain <5 atomic% Ni. In contrast, Fe-Ni sulfides in the KOOL grain have variable Ni contents ranging from 2.1 to 21.9 atomic% Ni. The compositional fields of monosulfide solid solution (Mss), high-temperature pentlandite, and liquid (sulfide melt) at 800 ºC are indicated in the diagram of L2036 #20 (Kitakaze et al., 2011). The chemical compositions of Fe-Ni sulfide in the KOOL grain overlap with those of Mss and high-temperature pentlandite (Fig. 9). Many Fe-Ni sulfide crystals in the POP CLO and the KOOL grain contain detectable amounts of Co when they were measured using FE-EPMA (~0.1 to ~0.44 wt.%) (Fig. S2).

3.5 Ultra-refractory SHIB fragment

The SHIB hibonite contains 0.1 wt.% Y_2O_3 according to the EPMA analysis (Table 1). However, it is heterogeneous on a sub-micrometer scale. Its EDS spectrum shows a small Zr Kα peak but not a Y Kα peak (Fig. S3a). The perovskite contains 2.1 wt.% ZrO_2 and 1.4 wt.% Y_2O_3 based on EPMA analysis (Table 1 and Fig. S3b). The spinel contains 0.51 wt.% V_2O_5 and 0.28 wt.% TiO_2 (Table 1 and Fig. S3c). The hibonite and perovskite contain Ti-bearing Zr-rich oxide inclusions (Figs. S3d, e) and <50-nm-sized refractory metal nuggets (RMNs) containing Os, Ir, Mo, and Ru (Figs. 3f, g, S4). Nanobeam electron diffraction patterns and lattice fringes show that the RMNs have a hexagonal crystal symmetry. The trace elements in hibonite and perovskite, Zr-rich oxide, and RMNs indicate that the SHIB fragment is an ultra-refractory inclusion (Ireland, 1988).

3.6 Aqueous alteration of the SHIB fragment

The periphery of the SHIB fragment shows evidence of aqueous alteration (Figs. S5a,b). Because perovskite crystals are embedded in phyllosilicates (Fig. S5b), phyllosilicates enclosing perovskite were altered to phyllosilicates during aqueous alteration. However, what mineral was replaced by the phyllosilicates needs to be clarified. The

phyllosilicates show ~1-nm lattice fringes, suggestive of saponite (Fig. S5c). The edge of the SHIB fragment directly attaches to the fine-grained matrix (Fig. S5b). A small (<50 nm) Hg- and S-rich phase is embedded in phyllosilicates (Fig. S5d), which may be cinnabar. Still, we were unable to obtain its diffraction pattern. Minor amounts of phyllosilicate and aggregates of <20-nm-sized Fe-Mg oxide grains were also observed in the matrix. The latter is common among hydrated fine-grained AMMs that experienced moderate heating during atmospheric entry. The aggregates are probably thermally decomposed Fe-Mg carbonate (Noguchi et al., 2003).

3.7 Mineralogy of the fine-grained matrices of the four samples

TEM images of the ultrathin sections of the four samples (Fig. 2) show that the fine-grained matrices are highly porous, up to >50% porosity. These matrices seem to contain both abundant GEMS and enstatite whiskers/platelets (Fig. 10a to g), and their textures seem to be indistinguishable from those of CP IDPs (Bradley, 2014; Ishii et al., 2008). Comparison among the high angle annular dark field–scanning transmission electron microscopy (HAADF-STEM) images and the corresponding Fe, Ni, S, and Si elemental maps of GEMS in D03IB64, D05IB66, and L2036 #20 (Fig. 11a to c) shows the following: the GEMS grains

containing both Fe-Ni metal and Fe(-Ni) sulfide; the variable relative amounts of Fe-Ni metal and Fe(-Ni) sulfide among samples, and the Fe-poor amorphous silicate in the GEMS grains. In contrast, in the case of D05IB84, the same comparison reveals that the GEMS in D05IB84 does not contain Fe-Ni metal but contains only Fe-Ni sulfide and Fe-rich amorphous silicate as shown in Fig. 11d. Given the absence of Fe-Ni metal, the GEMS in D05IB84 is not a GEMS grain *sensu stricto*.

The Olivine / (Olivine + Low-Ca pyroxene) ratios in the matrices of D03IB66, D05IB66, L2036 #20, and D05IB84 are 0.5 (n=24), 0.4 (n=18), 0.6 (n=29), and 0.6 (n=22), respectively. Olivine and pyroxene in the matrices of the samples except for D05IB66 contain abundant solar flare tracks (Table 2; Figs. 10h to j). The number densities of solar flare tracks in D03IB64, L2036#20, and D05IB84 are $>8 \times 10^{10}$, $3–4 \times 10^{10}$, and 3×10^{10} tracks/cm^2, respectively.

The matrix olivines in the four samples are heterogeneous $Fa_{\sim 0–\sim 48}$, and there is a small peak in the bin $Fa_{0\text{-}1}$ in the histogram (Fig. 6a). The matrix low-Ca pyroxenes are also heterogeneous $Fs_{\sim 0–\sim 33}$, and most of them are $<Fs_5$, and most have $<Fs_2$ (Fig. 6b). All four samples contain minor high-Ca pyroxene (Fig. 6c).

Figure 7 shows the FeO vs. MnO contents and the FeO vs. Cr_2O_3 contents in olivine

and low-Ca pyroxene in the matrices of the four investigated samples. They are in the compositional fields of olivine in IDPs, the matrices of primitive chondrites, and the Wild 2 samples (Klöck et al., 1989; Zolensky et al., 2006; Frank et al., 2014). Some olivine and low-Ca pyroxene crystals are low-iron manganese-enriched (LIME) chemical compositions (Klöck et al., 1989) (Fig.7a).

In Fig. 9, Fe-Ni sulfides in the matrices of the four samples are plotted with those in the CLOs and the KOOL grain. Almost all the Fe-Ni sulfides in them are poor in Ni (<5 atomic%). D05IB84 experienced weak aqueous alteration, as described in section 3.6. However, the compositions of Fe-Ni sulfides in it are more similar to those in the other three samples that do not show evidence of aqueous alteration. Their sulfide compositions are distinct from those in CS (or hydrated) IDPs, in which the compositions of Fe-Ni sulfides continuously range from pyrrhotite to pentlandite (Zolensky and Thomas, 1995).

3.8 Oxygen isotopic compositions of the two CLOs and the KOOL grain

Oxygen isotopic compositions of olivine and pyroxene in the two CLOs and the KOOL grain are shown in Figs. 12a to c. In the case of the BO-like CLO (Fig. 12a), oxygen isotopic compositions of the mixture of olivine and interstitial glass were obtained because the sizes

of olivine grains are smaller than the $^{133}Cs^{+}$ primary beam sizes as shown in the BSE image in Fig. 12a. Their O isotopes plot near the intersection between the Primitive chondrule mineral (PCM) and the Terrestrial fractionation (TF) lines and all of them are below the TF line. Because of the matrix effect of SIMS measurements, the $\delta^{18}O$ value of the mixtures of olivine and glass tends to be slightly smaller (<~2‰) when the correction factor of olivine is applied (see the electronic annex EA1 of Ushikubo et al., 2012). Thus, the $\delta^{18}O$ values of the BO-like CLO presented in Fig. 12a may be several permille smaller than the actual values. Olivine and low-Ca pyroxene compositions in the POP CLO (Fig. 12b) are plotted along or near the PCM line. The magnesian (~Fs_1 in Fig. 6a) cores of low-Ca pyroxene crystals (#4 and 6) are richer in ^{16}O with $\Delta^{17}O$ of –6.8 to –5.6‰ (vertical displacement from the TF line) than that in the rims of low-Ca pyroxene and olivine (Table 3). In contrast, a ferroan (Fs_{12-16}) rim of a low-Ca pyroxene crystal (#1, 5, 7) and olivine crystals have $\Delta^{17}O$ of ~–0.9 to –0.4‰ (Table 3). The areas between the magnesian cores and ferroan rims of the low-Ca pyroxene crystals (#2 and 3) have intermediate with $\Delta^{17}O$ of ~–3.0 to –2.5‰ (Table 3). The compositions of olivine and high-Ca pyroxene grains in the KOOL grain plot above the TF line and the PCM lines with $\Delta^{17}O$ of +1.9 to +3.4‰ (Fig. 12c; Table 3). The high-Ca pyroxene crystals have $\delta^{18}O$ values of +6.5 to +7.6‰, larger than most olivine crystals in this object.

The relationships between oxygen isotopes and Mg# of olivine and pyroxene in the two CLOs and the KOOL grain is shown in Fig. 13. Two exceptionally low values (–6.8 and –5.6‰) correspond to the relict low-Ca pyroxene crystals in the POP CLO (Fig. 12b). The occurrence of $\Delta^{17}O$ ~-5‰ for Mg# >95 and positive $\Delta^{17}O$ for Mg# <90 is qualitatively similar to the trend seen in the 81P/Wild 2 cometary chondrules (Defouilloy et al., 2017) and CLOs and large mineral fragments in a giant cluster IDP (Zhang et al., 2021) (Fig. 13).

3.9 Oxygen isotopic compositions of the SHIB fragment

The oxygen isotopic compositions of spinel in the SHIB fragment are shown in Fig. 12e. The numbers on the BSE image of the SHIB fragment correspond to those on the corresponding three oxygen isotopic diagrams. The $\Delta^{17}O$ values of spinel grains range from –22‰ to –24‰, and the $\delta^{18}O$ values range from –44.8‰ to –46.8‰ (Fig. 12e; Table 3). Considering oxygen isotopic ratios and mineralogy, the SHIBs in CMs are the most similar refractory inclusions to this SHIB fragment (e.g., Kööp et al., 2016).

3.10 Aluminum-magnesium isotope signature of the SHIB fragment

The Mg-Al isotopic systematics of spinel and hibonite in the SHIB fragment are shown

in Fig. 12f. Resolvable ^{26}Mg excesses are observed in hibonite (Fig. 12f, Table 4). The inferred initial $(^{26}Al/^{27}Al)_0$ ratio is $(5.0 \pm 0.8) \times 10^{-5}$ (2σ), which is consistent with the canonical ^{26}Al abundance of CAIs in chondrites (Jacobsen et al., 2008; Liu et al., 2012). Given that the canonical value of $(^{26}Al/^{27}Al)_0$ is 5.25×10^{-5} and with $t_{1/2}$ of ^{26}Al = 0.705 Myr (Larsen et al., 2011; Norris et al., 1983) the formation time of the inclusion is estimated as 0.05 + 0.17/ -0.14 Myr after the formation of the oldest CAIs in CV chondrites (Larsen et al., 2011).

3.11 Isotopic anomalies in the fine-grained matrix of D03IB64

To assess the primitiveness of the fine-grained matrices of these samples, we selected AMM D03IB64 because its matrix does not show any evidence of aqueous alteration and contains tiny silicates with high track density. Because tracks can be easily erased during atmospheric heating, it is inferred that this AMM did not experience the erasure temperature of ~550 ^{o}C of tracks in olivine (Fraundorf et al., 1982).

We performed C, N, and O isotope mapping of the matrix. Whereas the bulk C and N isotopic ratios are indistinguishable from the terrestrial compositions, a few isotopically anomalous areas with elevated $\delta^{15}N$ values ($\delta^{15}N = \{(^{15}N/^{14}N)_{sample} / (^{15}N/^{14}N)_{Air} - 1\}$ in per

mil) were found in ion images (Fig. 14a). The average $\delta^{15}N$ value of the hotspots in D03IB64 is approximately 400‰. We also found one presolar silicate grain (Fig. 14b). This grain has a significant ^{17}O enrichment as well as a significant ^{18}O depletion relative to the surrounding matrix, with $\delta^{17}O = +620 \pm 110$ ‰ and $\delta^{18}O = -280 \pm 30$ ‰, which are consistent with those of O isotope Group 1 grains (Nittler et al., 1997). Its identification as a silicate rather than an oxide was qualitatively made based on the observed the $^{28}Si^{-}/^{27}Al^{16}O^{-}$ ratio relative to the normal matrix grains. The size of the presolar grain was estimated to be ~300 nm from the number of pixels of the area with O isotopic anomalies.

4. DISCUSSION

4.1 Comparison of petrography and mineralogy of the two CLOs and the KOOL grain with those of meteoritic chondrules

The CLOs and the KOOL grain investigated in this study are small fragments of larger objects, similar to the case of Stardust samples. However, there is a sampling bias for Stardust samples due to the capture method, which inevitably destroyed many grains (Noguchi et al., 2007).

As described in section 3.4, the BO-like CLO in D03IB64 can be classified as type II

CLO based on the chemical compositions of its olivine grains. Its Si- and CI-normalized bulk elemental abundances are within the ranges of the type II chondrules in L/LL3, R3, and CR2 chondrites, but its abundance pattern does not match the range of a specific chondrite group. The KOOL grain in L2036#20 shows bulk Na and K abundances near or above the upper limits of the Na and K abundances in type II meteoritic chondrules and of the KOOL grain Coki-A in a Wild2 sample (Fig. 5a). The Si- and CI-normalized Na and K abundances of interstitial glass in the KOOL grain are also at the upper end of the abundances in type II meteoritic chondrules (Fig. 5b).

In both the BO-like CLO and the KOOL grain, K is more enriched than Na relative to their CI abundances (Fig. 5), which is common to the type II chondrules in MET 00526 L/LL3 and MET 00426 CR2 (Berlin, 2009), and the KOOL grain Coki-A (Joswiak et al., 2009). The same tendency may support the idea that KOOL grains in IDPs and Wild2 samples are one of the precursors of type II chondrules (Joswiak et al., 2009).

The POP CLO in D05IB66 contains homogeneous olivine with Fa_{20-21} and low-Ca pyroxene with magnesian cores with $>En_{97}$ and ferroan rims with En_{80-82} (Figs. 6a, b). However, because there is a gap between the magnesian cores and the ferroan rims in the three-oxygen isotopic diagram (Fig. 12b), the magnesian cores are relict grains that survived

partial melting of their precursor. In addition, its bulk chemical composition excluding the magnesian relict crystals, is within the range of type II chondrules in L/LL3 (Fig. 5a). The deficient (4%) modal abundance of interstitial glass in this CLO suggests that it was probably only partially melted in an environment that was similar to the formation environment of the type II chondrules.

The FeO versus MnO (wt.%) diagram shows that olivine and low-Ca pyroxene in the CLOs and the KOOL grain overlaps with those in the matrices in which they are embedded (Fig. 7a). The distribution of the ferromagnesian silicates in Fig. 7a is similar to olivine in both chondrules and matrices in CR and L/LL3.0-3.05 meteorites as well as olivine in the Wild 2 samples (Frank et al., 2014) and FeO-poor low-Ca pyroxene in IDPs (Klöck et al., 1989) (Fig. 7a). In a FeO versus Cr_2O_3 wt.% diagram olivine crystals in the two CLOs are plotted on or around the solar ratio line (Fig. 7b), which is similar to those in CLOs in a giant cluster IDP (Zhang et al., 2021). The low-Ca pyroxenes in the two CLOs are enriched in Cr_2O_3 relative to the solar ratio line (Fig. 7b). The very low (~0.1wt.%) Cr_2O_3 contents in the olivines in the KOOL grain (Fig. 7b) are probably related to the prior crystallization of Ko-rich high-Ca pyroxene, which seems more likely than co-crystallization (Figs. 6d and 7b). During the crystallization of these phases, Cr_2O_3 in the melt was selectively distributed to

high-Ca pyroxene, which made the high-Ca pyroxene Ko-ich.

In the molar Fe/Mn versus Fe/Mg diagram, olivine crystals in the BO-like CLO and the KOOL grain plot around the median value of that in L/LL3 chondrites and at the lowest molar Fe/Mn end of the compositional field of CR2 chondrites (Fig. 8), although there is an ambiguity on the exact $\delta^{18}O$ values of the BO-like CLO as described in section 3.7. The KOOL grain investigated is plotted near the Puki KOOL grain found among 81P/Wild 2 samples (Joswiak et al., 2012) (Fig. 8). The oxygen isotope compositions of olivine in these objects plot just below or above the PCM line like that in OCs (Figs. 12a, c). Around zero $\Delta^{17}O$ values in the BO-like CLO are common to olivine in type II chondrules in CR2s and some olivines in IDPs, AMMs, and Wild2 samples (Figs. 12a, d) (e.g., Tenner et al., 2015; Miller et al., 2017; Aléon et al., 2009; Nakashima et al., 2012a, b; Zhang et al., 2021; Engrand et al., 1999; Gounelle et al., 2005). In contrast, the positive $\Delta^{17}O$ values in the KOOL grain are common to the olivines in type II chondrules in L/LL3s (probably also to OCs in general) and Rs and also found in the olivines in IDPs and Wild2 samples including the KOOL grain Puki (Figs. 12c, d) (e.g., Kita et al., 2010; Miller et al., 2017; Aléon et al., 2009; Nakashima et al., 2012a, b; Defouilloy et al., 2017; Zhang et al., 2021), although few chondrules have $\Delta^{17}O$ values as high as the KOOL grain.

Chondrule olivines in CH-CBs have $\Delta^{17}O$ values as high as those in the KOOL grain. Although the high $\Delta^{17}O$ values of type I porphyritic chondrules in CHs might reflect oxygen isotopic ratios of organic material that acted as reducing agents during chondrule formation, type II chondrules in CHs have possibly formed from a similar reservoir to that for type II chondrules in CRs (Nakashima et al., 2024). Non-porphyritic Fe-rich chondrules in CHs might be formed by mechanisms different from ferromagnesian chondrules in the other chondrites because they have fractionated (SiO_2-bearing) bulk chemical compositions (Nakashima et al., 2020). In CBs, impact origins of chondrules are favored (e.g., Krot et al., 2005).

The olivine crystals in the POP CLO plot near the lowest molar Fe/Mn edge of the compositional field of olivine in L/LL3 chondrites (Fig. 8), where the olivine crystals in the Wild 2 CLO Torajiro are also plotted (Nakamura et al., 2008). These values are similar to the compositions of olivine in the CLO captured at the ISS (Noguchi et al., 2011). Oxygen isotope ratios of olivine in this CLO plot along the PCM line (Fig. 10b) like the chondrules in the primitive carbonaceous chondrites such as Acfer 094 and CR2s (Ushikubo et al., 2012; Tenner et al., 2015). Considering both features, the precursor material of the POP CLO may be similar to but slightly different from that of chondrules in CR2 chondrites.

745

746 **4.2 Abundant Fe-bearing sulfides and no Fe-Ni metal in the two CLOs and the KOOL**

747 **grain**

748 Schrader et al. (2021) showed that unequilibrated OCs with 3.00-3.1 and CR2

749 chondrites contain Fe sulfide near troilite chemical compositions. Unequilibrated R3.2 clasts

750 in Mount Prestrud (PRE) 95404 R chondrite contain Fe-Ni sulfides with the solar Ni to Co

751 ratio on the rims of chondrules and in chondrule-sized sulfide nodules (Miller et al., 2017).

752 The R3.2 clasts contain abundant sulfide as sulfide nodules and sulfide-rims on chondrules.

753 Since the thermal metamorphism experienced by these clasts is expected to have been weak,

754 the chondrules with sulfide rims would be helpful in discussing the formation conditions for

755 the CLOs and the KOOL grain. Miller et al. (2017) showed that Rs were formed in an

756 environment with high fS_2. They proposed that the increased surface density of the protosolar

757 disk near the snow line may enhance the formation of H_2S via hydrogenation of S on grain

758 surfaces, and H_2S might corrode metallic Fe to incorporate S in it (e.g., Lauretta et al., 1997).

759 The two CLOs contain pyrrhotite, and the KOOL grain contains Fe-Ni sulfides with

760 compositions consistent with monosulfide solid solution (Mss in Fig. 9). None of them

761 contain either Fe-Ni metal or magnetite. The above mentioned scenario could apply to the

formation of the CLOs and the KOOL grain. Monosulfide solid solution can be formed by the gas-solid reaction between H_2S-H_2 gas and Fe-Ni metal (Lauretta et al., 1997), which probably occurred during their formation. During the melting of the precursor materials of the CLOs and the KOOL grain, a part of Fe-Ni metallic melts in the precursors was probably oxidized and incorporated in ferromagnesian silicates during crystallization. The remaining Fe-Ni metallic melts might be sulfurized by the reaction with H_2S gas, which might have been formed efficiently by hydrogenating S on grain surfaces at low temperatures (e.g., Herbst et al., 1989). In addition, the following possibilities could be considered: (1) there was no metallic Fe in their precursors because the CLOs and the KOOL grain were so small, (2) they lost their metallic Fe very efficiently but some sulfide remained dissolved in the melt until it reached sulfide saturation as a result of cooling and crystallization.

4.3 Crystallization sequences of the two CLOs and the KOOL grain

Crystallization sequences of the two CLOs and the KOOL grain and the two CLOs Torajiro and Iris found in the Wild 2 samples (Nakamura et al., 2008; Gainsforth et al., 2015) for comparison were calculated using MELTS (Ghiorso and Sack 1995; Asimow and Ghiorso 1998) although f_{S_2} was not able to incorporate in the calculation (Figs S6 to S8). We

calculated weighted averages of the chemical compositions of phases measured using FE-EPMA for each igneous object investigated in this study to obtain the bulk chemical compositions of the two CLOs and the KOOL grain (Tables S2 and S3). In the case of Torajiro, the weighted average of EDS data of phases was obtained from their relative areas in a BSE image in Nakamura et al. (2008), and we used the estimated bulk chemical composition of Iris in Gainsforth et al. (2015) (Table S3). Crystallization sequences were calculated to the temperatures just above the solidus except for the KOOL grain. In this case, the crystallization calculation was stopped at 700 ºC because melt existed at such a low temperature due to the enrichment of alkaline elements in melt. Equilibrium crystallization under 1 bar was assumed according to Gainsforth et al. (2015), which means relatively slow crystallization. Crystallization sequences were calculated at QMF ±0, –2, and –4, these values correspond approximately IW +3.5, +1.5, –0.5 at 1200 ºC (Myers and Eugster, 1983).

The results show that the equilibrium crystallization calculations using MELTS can reproduce the minerals in the POP CLO excluding magnesian relict low-Ca pyroxene that did not melt during CLO formation (Fig. S6b) and Torajiro (Fig. S6d) qualitatively. Calculated modal abundances of olivine, low-Ca pyroxene, and mesostasis (glass) of the POP CLO at 1200 ºC are ~40%, ~50%, and ~10% irrespective of different oxygen buffers and the

real modal abundances are 45%, 48%, and 7%, respectively, and calculated Mg# of olivine at 1200 ºC is ~75–77, which is similar to the observed Mg# value ~73 (Fig. S6b). Similarly, calculated modal abundances of spinel, olivine, low-Ca pyroxene, and mesostasis (glass) of Torajiro at 1200 ºC are ~10%, 40%, ~40%, and ~10% irrespective of different oxygen buffers and the real modal abundances are 6%, 36%, 52%, and 7%, respectively, and calculated Mg# of olivine at 1200 ºC is ~80-82, which is similar to the observed Mg# value 78 (Fig. S6d). The real chemical compositions of glass in the POP CLO (indicated by red stars) are plotted near the calculated trends of the melt compositions during crystallization (Fig. S6b). These diagrams suggest that these objects experienced near-equilibrium crystallization, which probably resulted from partial melting and crystallization under slow cooling rates.

In contrast, the equilibrium crystallization calculation of the BO-like CLO and the KOOL grain cannot reproduce the minerals in them. Abundant low-Ca pyroxene and plagioclase (and high-Ca pyroxene in the case of BO-like CLO at the QMF +0) in the equilibrium crystallization calculation are not contained in them (Figs. S6a, c). In the case of the BO-like CLO, the calculation suggests that rapid cooling and rapid crystallization of silicate melt from above liquidus might prohibit crystallization of low-Ca pyroxene from the melt, which is plausible because crystallization of low-Ca pyroxene requires a reaction

between olivine and melt. More skeletal shapes of olivine crystal in this BO-like CLO than typical meteoritic BO chondrules suggest that it might experience more rapid cooling and/or a larger supercooling during crystallization than most meteoritic BO chondrites because olivine in the BO-like CLO resembles skeletal olivine chondrules in CB and CH chondrites (Krot et al., 2006). In the KOOL grain, Ko-rich high-Ca pyroxene could crystallize at a higher temperature than low-Ca pyroxene and plagioclase although the MELTS program does not consider the Ko component to crystallize high-Ca pyroxene.

Figure S7 shows the crystallization calculation of these objects in the case of suppression of crystallization of low-Ca pyroxene and plagioclase (and high-Ca pyroxene in the case of BO-like CLO at the QMF +0). The calculated modal abundances are similar to the real values (Table S2). The compositional changes of glasses during the crystallization calculations of Figs. S6a and d, and S7 are shown in Fig. S8. Their compositions are qualitatively similar to the chemical compositions of the real glasses in these objects.

In conclusion, the crystallization calculations suggest that the BO-like CLO was formed during rapid cooling, the POP CLO was formed during slow cooling, and the KOOL grain crystallized from melt, but its crystallization condition is still unclear.

4.4 Oxygen isotopic ratios of the two CLOs and the KOOL grain

The relationship between Mg# and $\Delta^{17}O$ of olivine and low-Ca pyroxene in the two CLOs and the KOOL grain overlap with those in CLOs in a giant cluster IDP and Wild 2 samples (Fig. 12). They also overlap with those in type II chondrules in CR chondrites (Tenner et al., 2015; Schrader et al., 2013; 2014; 2017; Connolly and Huss, 2010; Marrocchi et al., 2022), Tagish Lake C2 (Ushikubo and Kimura, 2021), and Tagish Lake-like C2 chondrites (Yamanobe et al., 2018). These results are consistent with the above discussion.

There are also differences between the CLOs (and KOOL grains) in the AMMs, the IDP, a giant cluster IDP (Zhang et al., 2021), and Wild2 samples (Nakamura et al., 2008; Nakashima et al., 2012b; Defouilloy et al., 2017), and type II chondrules in CR chondrites (Tenner et al., 2015). Firstly, type II CLOs are more abundant than type I: 100% (n=2, this study), 70% (n=27; Zhang et al., 2021), and 43% (n=21; McKeegan et al., 2006; Nakashima et al., 2012a; Ogliore et al., 2012; Defouilloy et al., 2017) in AMMs, IDPs, and Wild 2 samples, respectively. In contrast, type II chondrules occupy 3.5% of the chondrules in CR2 chondrites (Schrader et al., 2011). Both elevated dust-to-gas ratio and elevated H_2O ice abundance in dust are required to make the type II chondrules in CR chondrites (Tenner et al., 2015). Higher abundances of type II CLOs as well as the KOOL grain in the AMMs,

IDPs, and Wild 2 samples than type II chondrules in CR2 chondrites suggest that not only Wild 2 comet but also parent bodies of the AMMs and IDPs contain CLOs formed in the regions richer in ^{16}O-poor H_2O ice than of the forming area of CR chondrules in the early solar system. Type II chondrules in CR chondrites, which have high $\Delta^{17}O$ and low Mg# of ferromagnesian silicates, were formed under the influence of water ice (Tenner et al., 2015). In other words, CLOs formed further from the Sun than CR chondrules might be selectively transferred to the accretion area of the comets or comet-like icy bodies. The transfer of the CLOs, which formed in oxidizing environments beyond the snow line of the solar system, to the comet-forming region might be a common process in the early solar system history.

4.5 Ultrarefractory SHIB fragment and comparison with SHIBs in CM chondrites

The SHIB fragment in D05IB84 (Fig. 3d) has a texture that is very similar to SHIB inclusions of the most common type (bladed laths of hibonite enclosed in spinel) found in CM chondrites (e.g., Brearley and Jones, 1998 and references therein). It shows a ^{26}Mg excess with a $(^{26}Al/^{27}Al)_0$ ratio of $(5.0 \pm 0.8) \times 10^{-5}$ (2σ) and ^{16}O-rich composition with $\delta^{18}O \approx \delta^{17}O = -46‰$ (Figs. 3d, 12e, f), which are also common to SHIBs in CM chondrites (e.g., Simon et al., 2006). In addition, this SHIB fragment is ultrarefractory because hibonite

contains a detectable amount of Y (Fig. S3, Table 1). In addition, ultrarefractory oxides such as Zr oxide and refractory metal nuggets (RMNs) are included in spinel, hibonite, and perovskite (Fig. S3). Some SHIBs in Murchison showed the ultrarefractory-enriched REE patterns (Ireland, 1988). The chemical compositions of RMNs in SHIBs in Murchison were presented in Schwander et al. (2015). The RMNs in Murchison contain abundant Pt, Mo, Os, Ir, and Ru with minor Ni, W, Re, and Rh (Schwander et al., 2015). The RMN in the SHIB fragment also contains Mo, Os, Ir, and Ru but does not contain detectable amounts of Re, W, and Pt. The abundance of refractory siderophile elements in the Murchison SHIBs are quite variable (Fig. S4), so it is reasonable that Re, W, and Pt are below detection. Therefore, it would not say that there is a compositional difference between the RMN in the SHIB fragment and those in the Murchison SHIBs. The SHIB fragment could be almost equivalent to an ultrarefractory SHIB in CM chondrites.

4.6 Fine-grained matrices that are indistinguishable from CP IDPs and CP AMMs

The fine-grained matrices of two AMMs, D03IB64 and D05IB66, containing CLOs and an IDP L2036#20 containing a KOOL grain are highly porous and contain minerals that are the same as those in CP IDPs and CP AMMs (e.g., Ishii et al., 2008; Bradley, 2014) (Figs.

2a-c). Neither the coarse-grained igneous objects nor the fine-grained matrices show evidence of aqueous alteration (Figs. 3, 10, 11). In addition, we found one presolar silicate grain with an O isotopic anomaly (Fig. 14b). This grain has a significant ^{17}O enrichment as well as a significant ^{18}O depletion relative to the surrounding matrix, consistent with O isotope Group 1 grain (Nittler et al., 1997). The inferred concentration of presolar grains in the fine-grained matrix of D03IB64 is ~920ppm. However, a direct comparison to the concentrations for primitive chondrites is difficult because of the limited measurement area (93 μm^2) and because only one presolar grain with oxygen isotope anomaly was found. However, the presence of the presolar silicate confirms the primitiveness of D03IB64.

The $\delta^{15}N$ values of the hotspots in D03IB64 range from 367.0 to 530.5‰ (Fig. 14a), which is lower than the maximum $\delta^{15}N$ value of hotspots in insoluble organic matter (IOM) from CR chondrites (~1800‰) (Busemann et al., 2006) and that of hotspots in the matrix of CR2 chondrites (~2475‰) (Floss and Stadermann, 2009) and C2 chondrite Bells (~2400‰) (De Gregorio et al., 2013). However, given the small areas analyzed here, a direct comparison between the AMM and the primitive meteorites is impossible.

4.7 Effects of weak aqueous alteration on the fine-grained matrix and the SHIB

fragment

The fine-grained matrix of D05IB84 is almost the same as the matrices mentioned above. Still, it contains aqueously altered GEMS-like objects, which lack nanometer-sized Fe-Ni metal, and the amorphous silicate in "GEMS" contains a detectable amount of Fe (Figs. 10, 11). Fine-grained matrices containing abundant non-porous Fe-bearing amorphous silicate were reported from some chondrites such as ALH 77307 CO3.0, Acfer 094 ungrouped C, Paris CM2, Asuka 12169 CM3.0 chondrites (Brearley, 1993; Greshake, 1997; Leroux et al., 2015; Noguchi et al., 2021). However, highly porous lithology is relatively rare. Clasts or patches containing the Fe-bearing GEMS-like objects embedded in Acfer 094, LaPaz Icefield 02342 CR2, and the asteroid Ryugu grains were reported (Matsumoto et al., 2019; Nittler et al., 2019; Nakamura et al., 2023). Although the GEMS-like objects are mineralogically different from true GEMS (Bradley, 2019; Ohtaki et al., 2021; Villalon et al., 2021), the GEMS-like objects in such highly porous lithology with enstatite whiskers/platelets may be called the aqueously altered GEMS-like objects in D05IB84. In contrast, non-porous GEMS-like objects could experience the melting of ice grains existing between minerals, weak aqueous alteration, and compaction.

In D05IB84, the SHIB fragment contains an alteration product on its rim, and

perovskite grains are embedded in phyllosilicates in the altered rim (Figs. 3d, S5b). Melilite might be a precursor mineral before aqueous alteration because a rare melilite-bearing SHIBs was reported from Murchison CM chondrite (Kööp et al., 2016). In contrast, the fine-grained matrix surrounding the SHIB fragment contains aqueously altered GEMS-like objects that do not contain phyllosilicate (Fig. 10d). In one of the least aqueously altered CM chondrite Asuka 12169 (subtype 3.0), melilite in CAIs does not show any evidence of aqueous alteration on the FE-SEM scale (Kimura et al., 2020) and the fine-grained matrix of this meteorite contains abundant non-porous Fe-bearing amorphous silicate and does not contain phyllosilicate except for proto-tochilinite-cronstedtite-intergrowths (TCIs) (Noguchi et al., 2021). Frank et al. (2023) found that a melilite-rich CAI was embedded in the heavily altered Ivuna CI chondrite, and they suggested that the CAI was incorporated in the host after aqueous activity. Conversely, in this case, the SHIB fragment that experienced moderate aqueous alteration might be incorporated in the fine-grained matrix that experienced a much lower degree of aqueous alteration. There are two possibilities for the way of incorporation: regolith gardening of a single parent body composed of different degrees of aqueous alteration and mixing of a more hydrated impactor and a less hydrated host, as Frank et al. (2023) has suggested.

Refractory inclusions found among the Wild2 samples are mineralogically similar to type C CAIs defined by Lin and Kimura (1998) and Krot et al. (2004). The Wild2 refractory inclusions are composed of high-Ca pyroxene (diopside), Al- and Ti-rich high-Ca pyroxene (fassaite), with minor spinel, anorthite, and sometimes, and with or without osbornite (Zolensky et al. 2006; Simon et al. 2008; Matzel et al. 2010; Joswiak et al. 2012). ^{26}Al-^{26}Mg isotope systematics of one of them, Coki, were measured, and the Coki does not show any excess ^{26}Mg (Matzel et al., 2010). In addition, a CLO Iris also does not show any excess of ^{26}Mg (Ogliore et al., 2012). These data suggest that the Wild2 comet nucleus contains late-formed CAIs with little ^{26}Al, whereas the parent body of the SHIB fragment contains CAIs with the canonical ^{26}Al/^{27}Al ratio. This is consistent with the fact that the parent body of the SHIB fragment underwent aqueous alteration, which requires its accretion early enough to incorporate a substantial amount of ^{26}Al.

4.8 Possible parent bodies

Jupiter family comets are likely the principal source of dust in the zodiacal cloud (Nesvorný et al., 2010). Interplanetary dust particles (IDPs) in the zodiacal cloud are thought to originate from comets *and* asteroids because they include both anhydrous CP IDPs and

hydrated “CS” IDPs (Ishii et al., 2008; Bradley, 2014). Olivine/(Olivine+Low-Ca pyroxene) ratios of the four samples, from 0.4 to 0.6, are consistent with those of anhydrous “CP” IDPs (Zolensky and Barrett, 1994) and CP MMs (Noguchi et al., 2015), which are comparable with those of P- and D-type asteroids and comets, from 0.4 to 0.8 (Vernazza et al., 2015) and with comets, from 0.3 to 0.5 (Harker et al., 2023).

Keller and Flynn (2021) propose that IDPs with solar flare track densities of $>10^{10}$ tracks/cm^2 have exposure ages >1 Myr and were therefore ejected from objects in the trans-Neptunian objects and not from comets or asteroids. However, collisional lifetimes impose limitations on how far particles can survive from their sources; the required ~10^7-year orbital lifetime of IDPs from the Edgeworth-Kuiper Belt exceeds their expected collisional lifetimes by three orders of magnitude (Dohnyani, 1978; Grün et al., 1985). There are alternative explanations for such high-track densities in IDPs: temporal variations in solar activity, contributions from exposure to the galactic cosmic rays on parent body regolith before ejection, trapping in mean-motion resonances with Earth and other planets (Reach, 2010), and pre-accretion irradiation that may contribute to the high-track densities observed in the silicate minerals in dust grains from Jupiter family comets (Engrand et al., 2023). Further studies are needed to clarify the significance of track densities in determining parent body

origins.

5. CONCLUSIONS

We identified two CLOs, a KOOL grain, and a SHIB fragment from three AMMs and a CP IDP. The two CLOs-bearing and the SHIB fragment-bearing AMMs were found among ~200 AMMs preserved in the surface snow collected near the Dome Fuji Station. Because the two CLOs contain ferromagnesian silicates with <90 Mg#, they belong to the type II category of meteoritic chondrules. The CLOs are enclosed in highly porous fine-grained matrices containing abundant true GEMS (containing Fe-Ni metal) and enstatite whisker/platelets. The KOOL grain is also enclosed in a highly porous fine-grained matrix containing abundant true GEMS and enstatite whisker/platelets. None of the matrices show evidence of aqueous alteration. KOOL grains are also found in Stardust samples and CP IDPs (Joswiak et al., 2009). The low Mg# and elevated $\Delta^{17}O$ of olivine and pyroxene in these CLOs and the KOOL grain are consistent with previously studied CLOs from comet 81P/Wild 2 and a giant cluster IDP (e.g., Nakamura et al., 2008; Nakashima et al., 2012b; Zhang et al., 2021). These results support the view that CP IDP- and CP AMM-like materials constitute comet or comet-like icy bodies. The CLOs formed in oxidizing environment

beyond the snow line, and were then transferred to the comet-forming region. These processes were common in the early solar system history.

In contrast, the SHIB fragment experienced aqueous alteration on its rim. The SHIB fragment contains ultrarefractory oxides and RMNs and has a ^{26}Mg excess like typical meteoritic CAIs. The mineralogy of the fine-grained matrix is very similar to CP IDPs and CP AMMs. However, because "GEMS" in the matrix lacks Fe-Ni metal and amorphous silicate in it contains Fe, "GEMS" is not GEMS *sensu stricto*. It is clear that the matrix experienced aqueous alteration, by which the nanometer-sized Fe metal grains in GEMS were oxidized. The amorphous silicate in GEMS incorporated the Fe cations (Fig. 11d). Because the degree of aqueous alteration experienced by the SHIB fragment and that of the matrix are different, it is inferred that the SHIB fragment was incorporated into the matrix material after the aqueous alteration was finished.

Olivine/pyroxene ratios of the B-, C-, and G-type asteroids, P- and D-type asteroids, and comets obtained from mid-infrared spectra are considerably different (Vernazza et al., 2015). Olivine/low-Ca pyroxene ratios in the matrices of the four samples are within the range of P- and D-type asteroids and comets. They might have originated from these bodies.

Acknowledgments

The authors acknowledge H. Motoyama and JARE parties for collecting snow near the Dome Fuji Station, Antarctica. S. Nishida, M. Osonoi, and T. Saeki are appreciated for their support in collecting these AMMs. We thank NASA for providing IDPs. We are grateful to K. Ozawa for obtaining an EBSD map of D03IB64 and to K. Shimada and R. Kanemaru for obtaining FE-EPMA data of all the CLOs and the SHIB fragment. We thank C. M. O'D. Alexander, C. Engrand, and D. Schrader for their detailed comments, which were of great help in revising the manuscript. This study is supported by JSPS KAKENHI Grant Numbers 17340157, 13440158, and 19H00725 to TN, 17K18814 to TU, 18K03729 to MK, and by the Astrobiology Center Program of the National Institutes of Natural Sciences (NINS) (AB281011, AB291008, and AB301004 to TN).

Data Availability

Data are available through Mendeley Data at doi: 10.17632/5ycc5gs9rs.3.

Appendix A. Supplementary Material

The Supplementary Material contains: a detailed description of the correction method for the QSA effect; Table S1: detailed data table of the Mg isotope analyses of spinel and hibonite in D05IB84, and hibonite standards; Table 2: modal abundances of silicates and oxide in CLOs and a KOOL grain; Table S3: 100% normalized calculated bulk chemical compositions of the CLOs and the KOOL grain; Fig. S1: comparison between $\delta^{26}Mg^{*}$ values and surface density of O^{-} primary beam on the spinel standard; Fig. S2: Ni and Co contents in sulfide in the POP CLO and the KOOL grain; Fig. S3: ultra-refractory signatures of the SHIB fragment in D05IB84; Fig. S4: the CI and Ir normalized elemental abundances in an RMN in the SHIB fragment; Fig. S5: Phyllosilicate on the periphery of the SHIB fragment in AMM D05IB84; Fig. S6: equilibrium crystallization sequences of two CLOs and the KOOL grain as well as the CLO Trajiro; Fig. S7: crystallization sequences of the BO-like CLO and the KOOL with suppression of cyrsltallization of low-Ca pyroxene and plagioclase; Fig. S8: trends of chemical compositions of melt during crystallization. (a) the BO-like CLO shown in Fig. 7a, (b) the POP CLOs shown in Fig. 6b, (c) the KOOL grain shown in Fig. 7b, and the CLO Trajiro shown in Fig. S6d. Supplementary material to this article can be found online at https://data.mendeley.com/datasets/5ycc5gs9rs/2.

References

Aléon, J., Engrand, C., Leshin, L.A., McKeegan, K.D. (2009) Oxygen isotopic composition of chondritic interplanetary dust particles: A genetic link between carbonaceous chondrites and comets. Geochim. Cosmochim. Acta 73, 4558–4575.

Alexander, C.M.O'D., Wynn, J.G., Bowden, R. (2022) Sulfur abundances and isotopic compositions in bulk carbonaceous chondrites and insoluble organic material: Clues to elemental and isotopic fractionations of volatile chalcophiles. Meteorit. Planet. Sci. 57, 334–351.

Asimow, P.D., Ghiorso, M.S. (1998) Algorithmic modifications extending MELTS to calculate subsolidus phase relations. Am. Mineral. 83, 1127–1132.

Berlin, J. (2009) Mineralogy and bulk chemistry of chondrules. Ph.D. thesis, University of New Mexico, U.S.A.

Berlin, J., Jones, R.H., Brearley, A.J. (2011) Fe-Mn systematics of type IIA chondrules in unequilibrated CO, CR, and ordinary chondrites. Meteorit. Planet. Sci. 46, 513–533.

Bockelée-Morvan, D., Gautier, D., Hersant, F., Huré, J.-M., Robert, F. (2002) Turbulent radial mixing in the solar nebula as the source of crystalline silicates in comets. Astron. Astrophys. 384, 1107–1118.

Bradley, J.P. (2014) 1.8 Early Solar Nebula Grains - Interplanetary Dust Particles. In Meteorites and cosmochemical processes, Treatise of Geochemistry vol. 1, Davis, A. M. Ed. 287–308 (Elsevier, Amsterdam, ed. 2).

Bradley, J.P. (2019) GEMS and the devil in their details. Nat. Astron. 3, 603–5.

Brearley, A.J. (1993) Matrix and fine-grained rims in the unequilibrated CO3 chondrite, ALHA77307: Origins and evidence for diverse, primitive nebular dust components. Geochim. Cosmochim. Acta 57, 1521–1550.

Brearley, A.J., Jones R.H. (1998) Chondritic meteorites, in Papike, J.J. (Ed.), Planetary Materials, Reviews in Mineralogy vol. 36, Mineralogical Society of America, Washington, DC, pp. C1-C398.

Busemann, H., Young, A.F., Alexander, C.M.O'D., Hoppe, P., Mukhopadhyay, S., Nittler, L.R. (2006) Interstellar chemistry recorded in organic matter from primitive meteorites. Science 312, 727–730.

Catanzaro, E.J., Murphy, T.J., Garner, E.L., Shields, W.R. (1966) Absolute isotopic abundance ratios and atomic weights of magnesium. J. Res. Natl. Bur. Stand. 70a, 453–458.

Chaumard, N., Defouilloy, C., Kita, N.T. (2018) Oxygen isotope systematics of chondrules

in the Murchison CM2 chondrite and implications for the CO-CM relationship. Geochim. Cosmochim. Acta, 228, 220–242.

Christoffersen, R., Buseck, P.R. (1986) Refractory minerals in interplanetary dust. Science 234, 190–192.

Ciesla, F.J. (2007) Outward transport of high-temperature materials around the midplane of the solar nebula. Science 318, 613–615.

Clayton R. N., Onuma N., Grossman L., Mayeda T.K. (1977) Distribution of the presolar component in Allende and other carbonaceous chondrites. Earth Planet. Sci. Lett. 34, 209–224.

Connolly, Jr., H.C., Huss, G.R. (2010) Compositional evolution of the protoplanetary disk: Oxygen isotopes of type-II chondrules from CR2 chondrites. Geochim. Cosmochim. Acta 74, 2473–2483.

Davidson, J., Busemann, H., Franchi, I.A. (2012) A NanoSIMS and Raman spectroscopic comparison of interplanetary dust particles from comet Grigg-Skjellerup and non-Grigg Skjellerup collections. Meteorit. Planet. Sci. 47, 1748–1771.

Defouilloy, C., Nakashima, D., Joswiak, D. J., Brownlee, D.E., Tenner, T.J. Kita, N.T. (2017) Origin of crystalline silicates from Comet 81P/Wild 2: Combined study on their oxygen

isotopes and mineral chemistry. Earth Planet. Sci. Lett. 465, 145–154.

De Gregorio, B.T., Stroud, R.M., Nittler, L.R., Alexander, C.M.O'D., Bassim, N.D., Cody, G.D., David Kilcoyne, A. L., Sandford, S.A., Milam, S.N., Nuevo, M., Zega, T.J. (2013) Isotopic and chemical variation of organic nanoglobules in primitive meteorites. Meteorit. Planet. Sci. 48, 904–928.

Dobrică, E., Brearley, A. J. (2016) Microchondrules in two unequilibrated ordinary chondrites: Evidence for formation by splattering from chondrules during stochastic collisions in the solar nebula. Meteorit. Planet. Sci. 51, 884–905.

Dohnanyi, J. S. (1978) Particle Dynamics. In Cosmic Dust, McDonnel, J. A.M. Ed. 527–605 (Wiley, Chichester).

Engrand, C., McKeegan, K.D., Leshin, L.A. (1999) Oxygen isotopic compositions of individual minerals in Antarctic micrometeorites: Further links to carbonaceous chondrites. Geochim. Cosmochim. Acta 63, 2623–2636.

Engrand, C., Charon, E., Le Guillou, C., Leroux, H., Duprat, J., Dartois, E., Rojas, J., Bernard, S., Delauche, L., Sansberro, I., Fray, N., Cottin, H., Baklouti, D., Briois, C., Bardyn, A., Paquette, J., Silèn, J., Stenzel, O.J., Hilchenbach, M. (2023) Evidence of pre-accretion irradiation of cometary minerals in the inner solar system. 86th Ann. Meet. Meteorit. Soc.

#6234.

Floss, C., Stadermann, F.J. (2009) High abundances of circumstellar and interstellar C-anomalous phases in the primitive CR3 chondrites QUE 99177 AND MET 00426. Astrophys. J. 697, 1242–1255.

Frank, D. R., Zolensky, M.E., Le, L. (2014) Olivine in terminal particles of Stardust aerogel tracks and analogous grains in chondrite matrix. Geochim. Cosmochim. Acta 142, 240–259.

Frank, D. R., Huss, G.R., Zolensky, M.E., Nagashima, K., Le, L. (2023) Calcium-aluminum-rich inclusion found in the Ivuna CI chondrite: Are CI chondrites a good proxy for the bulk composition of the solar system? Meteorit. Planet. Sci. 58, 1495–1511.

Fraundorf, P., Lyons, T., Schubert, P. (1982) The survival of solar flare tracks in interplanetary dust silicates on deceleration in the Earth's atmosphere. J. Geophys. Res. 87, A409–A412.

Gainsforth, Z., Butterworth, A.L., Stodolna, J., Westphal, A.J., Huss, G.R., Nagashima, K., Ogliore, R., Brownlee, D.E., Joswiak, D., Tyliszczak, T., Simonovici, A.S. (2015) Constraints on the formation environment of two chondrule-like igneous particles from comet 81P/Wild 2. Geochim. Cosmochim. Acta 50, 976–1004.

Germani, M.S., Bradley J.P., Brownlee D.E. (1990) Automated thin-film analyses of hydrated

interplanetary dust particles in the analytical electron microscope. Earth Planet. Sci. Lett. 101, 162–179.

Ghiorso, M.S., Sack, R.O. (1995) Chemical mass transfer in magmatic processes IV. A revised and internally consistent thermodynamic model for the interpolation and extrapolation of liquid-solid equilibria in magmatic systems at elevated temperatures and pressures. Contrib. Mineral. Petrol., 119, 197–212.

Gounelle, M., Engrand, C., Maurette, M., Kurat, G., McKeegan, K.D. (2005) Small Antarctic micrometeorites: A mineralogical and in situ oxygen isotope study. Meteorit. Planet. Sci. 40, 917–932.

Greshake, A., Hoppe, P., Bischoff, A. (1996) Mineralogy, chemistry, and oxygen isotopes of refractory inclusions from stratospheric interplanetary dust particles and micrometeorites. Meteorit. Planet. Sci. 31, 739–748.

Greshake, A. (1997) The primitive matrix components of the unique carbonaceous chondrite Acfer 094: A TEM study. Geochim. Cosmochim. Acta 61, 437–455.

Grün E., Zook, H. A., Fechtig, H., Giese, R. H. (1985) Collisional balance of the meteoritic complex. Icarus 62, 244–272.

Harker, D.E., Wooden, D.H., Kelley, M.S.P., Woodward, C.E. (2023) Dust properties of

comets observed by Spitzer. Astrophys. J. 4, 242–272.

Heck, P.R., Ushikubo, T., Schmitz, B., Kita, N.T., Spicuzza, M.J., Valley, J.W. (2010) A single asteroidal source for extraterrestrial ordovician chromite grains from Sweden and China: High-precision oxygen three-isotope SIMS analysis. Geochim. Cosmochim. Acta 74, 497–509.

Herbst, E., DeFrees, D.J., Koch, W. (1987) Can interstellar H_2S be formed via gas-phase reactions? Calculations concerning the rates of the ternary and radiative association reactions between HS^+ and H_2. Mon. Not. R. Astr. Soc. 237, 1057–1065.

Hertwig, A., Defouilloy, C., Kita, N.T. (2018) Formation of chondrules in a moderately high dust enriched disk: evidence from oxygen isotopes of chondrules from the Kaba CV3 chondrite. Geochim. Cosmochim. Acta 224, 116–131.

Hewins R. H., Radomsky, P.M. (1990) Temperature conditions for chondrule formation. Meteoritics 25, 309–318.

Hoppe, P., Cohen, S., Meibom, A. (2013) NanoSIMS: Technical Aspects and Applications in Cosmochemistry and Biological Geochemistry. Geostandards and Geoanalytical Research 37, 111–154.

Hynes, K.M., Gyngard, F. (2009) The presolar grain data base: http://presolar.wustl.edu/~pgd.

Lunar Planet. Sci. Conf. 40, #1198.

Ireland, T.R. (1988) Trace-element abundances in hibonites from the Murchison carbonaceous chondrite: Constraints on high-temperature processes in the solar nebula. Geochim. Cosmochim. Acta 52, 2841–2854.

Ishii, H.A., Bradley, J.P., Dai, Z., Chi, M., Kearsley, A.T., Burchell, M.J., Browning, N.D., Molster, F. (2008) Comparison of comet 81P/Wild 2 dust with interplanetary dust from comets. Science 319, 447–450.

Ishii, H. A. (2019) Comparison of GEMS in interplanetary dust particles and GEMS-like objects in aerogel. Meteorit. Planet. Sci. 54, 202–219.

Jacobsen, B., Yin, Q., Moynier, F., Amelin, Y., Krot, A.N., Nagashima, K., Hutcheon, I.D., Palme, H. (2008) ^{26}Al-^{26}Mg and ^{207}Pb-^{206}Pb systematics of Allende CAIs: Canonical solar initial 26Al/27Al ratio reinstated. Earth Planet. Sci. Lett. 272, 353–364.

Joswiak, D.J., Brownlee, D.E., Matrajt, G., Westphal, A.J., Snead, C.J. (2009) Kosmochloric Ca-rich pyroxenes and FeO-rich olivines (Kool grains) and associated phases in Stardust tracks and chondritic porous interplanetary dust particles: Possible precursors to FeO-rich type II chondrules in ordinary chondrites. Meteorit. Planet. Sci. 44, 1561–1588.

Joswiak, D.J., Brownlee, D.E., Matrajt, G., Westphal, A.J., Snead, C.J., Gainsforth, Z. (2012)

Comprehensive examination of large mineral and rock fragments in Stardust tracks: Mineralogy, analogous extraterrestrial materials, and source regions. Meteorit. Planet. Sci. 47, 471–524.

Joswiak, D.J., Nakashima, D., Brownlee, D.E., Matrajt, G., Ushikubo, T., Kita, N.T., Messenger, S., Ito, M. (2014) Terminal particle from Stardust track 130: probable Al-rich chondrule fragment from comet Wild 2. Geochim. Cosmochim. Acta 144, 277–298.

Joswiak, D.J., Brownlee, D.E., Nguyen, A.N., Messenger, S. (2017) Refractory minerals in comet samples. Meteorit. Planet. Sci. 52, 1612–1648.

Kameda, T., Motoyama, H., Fujita, S., Takahashi, S. (2008) Temporal and spatial variability of surface mass balance at Dome Fuji, East Antarctica, by the stake method from 1995 to 2006. J. Glaciol. 54, 107–116.

Keller, C., Gail, H-P. (2004) Radial mixing in protoplanetary accretion disks. Astron. Astrophys. 415, 1177–1185.

Keller, L.P., Flynn, G. J. (2021) Evidence for a significant Kuiper belt dust contribution to the zodiacal cloud. Nat. Astron. **6**, 731-735.

Kimura, M., Imae, N., Komatsu, M., Barrat, J.A., Greenwood, R.C., Yamaguchi, A., Noguchi, T. (2020) The most primitive CM chondrites, Asuka 12085, 12169, and 12236, of

subtypes 3.0–2.8: Their characteristic features and classification. Polar Sci. 26, 100565.

Kita, N.T., Ushikubo, T., Fu, B., Valley, J.W. (2009) High precision SIMS oxygen isotope analysis and the effect of sample topography. Chem. Geol. 264, 43–57.

Kita, N.T., Nagahara, H., Tachibana, S., Tomomura, S., Spicuzza, M.J., Fournelle, J.H., Valley, J.W. (2010) High precision SIMS oxygen three isotope study of chondrules in LL3 chondrites: Role of ambient gas during chondrule formation. Geochim. Cosmochim. Acta 74, 6610–6635.

Kita, N.T., Ushikubo, T., Knight, K.B., Mendybaev, R.A., Davis, A.M., Richter, F.M., Fournelle, J.H. (2012) Internal ^{26}Al-^{26}Mg isotope systematics of a type B CAI: Remelting of refractory precursor solids. Geochim. Cosmochim. Acta 86, 37–51.

Kitakaze, A., Sugaki, A., Itoh, H., Komatsu, R. (2011) A revision of phase relations in the system Fe–Ni–S from 650 ºC to 450 ºC. Can. Mineral. 49, 1687–1710.

Klöck, W., Thomas, K.L., McKay, D.S., Palme, H. (1989) Unusual olivine and pyroxene composition in interplanetary dust and unequilibrated ordinary chondrites. Nature 339, 126–128.

Kööp, K., Nakashima, D., Heck, P.R., Kita, N.T., Tenner, T.J., Krot, A.N., Nagashima, K., Park, C., Davis, A.M. (2016) New constraints on the relationship between ^{26}Al and

oxygen, calcium, and titanium isotopic variation in the early solar system from a multielement isotopic study of spinel-hibonite inclusions. Geochim. Cosmochim. Acta 148, 151–172.

Krot, A.N., Rubin, A., Keil, K., Wasson, J. T. (1997) Microchondrules in ordinary chondrites: Implications for chondrule formation. Geochim. Cosmochim. Acta 61, 467–473.

Krot A.N., MacPherson G.J., Ulyanov A.A., Petaev M.I. (2004) Fine-grained, spinel-rich inclusions from the reduced CV chondrites Efremovka and Leoville: I. Mineralogy, petrology, and bulk chemistry. Meteorit. Planet. Sci. 39, 1517–53.

Krot, A.N., Amelin, Y., Cassen, P., Meibom, A. (2005) Young chondrules in CB chondrites from a giant impact in the early Solar System. Nature, 436, 989–992.

Krot, A.N., Ivanova, M.A., Ulyanov, A.A. (2006) Chondrules in the CB/CH-like carbonaceous chondrite Isheyevo: Evidence for various chondrule-forming mechanisms and multiple chondrule generations. Geochemistry 67, 283–300.

Krot, A.N., Nagashima, K., Yoshitake, M., Yurimoto, H. (2010) Oxygen isotopic compositions of chondrules from the metal-rich chondrites Isheyevo (CH/CB_b), MAC 02675 (CB_b) and QUE 94627 (CB_b). Geochim. Cosmochim. Acta 74, 2190–2211.

Larsen, K.K., Trinquier, A., Paton, C., Schiller, M., Wielandt, D., Ivanova, M.A., Connelly,

J.N., Nordlund, Å., Krot, A.N., Bizzarro, M. (2011) Evidence for magnesium isotope heterogeneity in the solar protoplanetary disk. Astrophys. J. 735, L37–44.

Lauretta, D.S., Lodders, K., Fegley, B. (1997) Experimental simulations of sulfide formation in the solar nebula. Science 277, 358–360.

Lauretta, D.S., Nagahara, H., Alexander, C.M.O'D. (2006) Petrology and origin of ferromagnesian silicate chondrules. In Meteorites and the Early Solar System, Lauretta, D.S., McSween, H.Y. Eds. (The University of Arizona Press, Tucson), pp. 431–459.

Leroux, H., Cuvillier, P., Zanda, B., Hewins, R.H. (2015) GEMS-like material in the matrix of the Paris meteorite and the early stages alteration of CM chondrites. Geochim. Cosmochim. Acta 170, 247–267.

Lin Y, Kimura M. (1998) Anorthite-spinel-rich inclusions in the Ningqiang carbonaceous chondrite: genetic links with type A and C inclusions. Meteorit. Planet. Sci. 33, 435–46.

Liu, M-C., McKeegan, K.D., Goswami, J.N., Marhas, K.K., Sahijpal, S., Ireland, T.R., Davis, A.M. (2009) Isotopic records in CM hibonites: Implications for timescales of mixing of isotope reservoirs in the solar nebula. Geochim. Cosmochim. Acta 73, 5051–5079.

Liu, M.-C., Chaussidon, M., Göpel, C., Lee, T. (2012) A heterogeneous solar nebula as sampled by CM hibonite grains. Earth Planet. Sci. Lett. 327–328, 75–83.

Marrocchi, Y., Piralla, M., Regnault, M., Batanova, V., Villeneuve, J., Jacquet, E. (2022) Isotopic evidence for two chondrule generations in CR chondrites and their relationships to other carbonaceous chondrites. Earth Planet. Sci. Lett. 593, 117683.

Matsumoto, M., Tsuchiyama, A., Nakato, A., Matsuno, J., Miyake, A., Kataoka, A., Ito, M., Tomioka, N., Kodama, Y., Uesugi, K., Takeuchi, A., Nakano, T., Vaccaro, E. (2019) Discovery of fossil asteroidal ice in primitive meteorite Acfer 094. Sci. Adv. 5, eaax5078.

Matzel, J.E.P., Ishii, H.A., Joswiak, D., Hutcheon, I.D., Bradley, J.P., Brownlee, D., Weber, P.K., Teslich, N., Matrajt, G., McKeegan, K., MacPherson, G.J. (2010) Constraints on the formation age of cometary material from the NASA Stardust mission. Science 328, 483–486.

McKeegan, K.D. (1987) Oxygen isotopes in refractory stratospheric dust particles: Proof of extraterrestrial origin. Science 237, 1468-1471.

McKeegan, K.D., Aléon J., Bradley, J., Brownlee, D., Busemann, H., Butterworth, A., Chaussidon, M., Fallon, S., Floss, C., Gilmour, J., Gounelle, M., Graham, G., Guan, Y., Heck, P.R., Hoppe, P., Hutcheon, I.D., Huth, J., Ishii, H., Ito, M., Jacobsen, S., B., Kearsley, A., Leshin, L. A., Liu, M.-C., Lyon, I., Marhas, K., Marty, B., Matrajt, G., Meibom, A., Messenger, S., Mostefaoui, S., Mukhopadhyay, S., Nakamura-Messenger,

K., Nittler, L., Palma, R., Pepin, R.O., Papanastassiou, D. A., Robert, F., Schlutter, D., Snead, S. J., Stadermann, F. J., Stroud, R., Tsou, P., Westphal, A., Young, E. D., Ziegler, K., Zimmermann, L., Zinner, E. (2006) Isotopic compositions of cometary matter returned by Stardust. Science 314, 1724–1728.

Miller, K.E., Lauretta, D.S., Connolly Jr., H.C., Berger, E.L., Nagashima, K., Domanik, K. (2017) Formation of unequilibrated R chondrite chondrules and opaque phase. Geochim. Cosmochim. Acta 209, 24–50.

Myers, J., and Eugster, H.P. (1983) The system Fe-Si-O: Oxygen buffer calibrations to 1500K. Contrib. Mineral. Petrol. 82, 75-90.

Nagashima, K., Krot, A.N., Huss, G.R. (2015) Oxygen-isotope compositions of chondrule phenocrysts and matrix grains in Kakangari K-grouplet chondrite: implication to a chondrule- matrix genetic relationship. Geochim. Cosmochim. Acta 151, 49–67.

Nakamura, K., Messenger, S., Keller, L.P. (2005) TEM and NanoSIMS study of hydrated/anhydrous phase mixed IDPs: cometary or asteroidal origin? Lunar Planet. Sci. Conf. 36, abstract #1824.

Nakamura, T., Noguchi, T., Tsuchiyama, A., Ushikubo, T., Kita, N.T., Valley, J.W., Zolensky, M.E., Kakazu, Y., Sakamoto, K., Mashio, E., Uesugi, K., Nakano, T. (2008)

Chondrulelike objects in short-period comet 81P/Wild 2. Science 321, 1664–1667.

Nakamura, T., Matsumoto, M., Amano, K., Enokido, Y., Zolensky, M.E., Mikouchi, T., Genda, H., Tanaka, S., Zolotov, M.Y., Kurosawa, K., Wakita, S., Hyodo, R., Nagano, H., Nakashima, D., Takahashi, Y., Fujioka, Y., Kikuiri, M., Kagawa, E., Matsuoka, M., Brearley, A.J., Tsuchiyama, A., Uesugi, M., Matsuno, J., Kimura, Y., Sato, M., Milliken, R.E., Tatsumi, E., Sugita, S., Hiroi, T., Kitazato, K., Brownlee, D., Joswiak, D.J., Takahashi, M., Ninomiya, K., Takahashi, T., Osawa, T., Terada, K., Brenker, F.E., Tkalcec, B.J., Vincze, L., Brunetto, R., Aléon-Toppani, A., Chan, Q. H. S., Roskosz, M., Viennet, J.-C., Beck, P., Alp, E.E., Michikami, T., Nagaashi, Y., Tsuji, T., Ino, Y., Martinez, J., Han, J., Dolocan, A., Bodnar, R.J., Tanaka, M., Yoshida, H., Sugiyama, K., King, A. J., Fukushi, K., Suga, H., Yamashita, S., Kawai, T., Inoue, K., Nakato, A., Noguchi, T., Vilas, F., Hendrix, A. R., Jaramillo-Correa, C., Domingue, D. L., Dominguez, G., Gainsforth, Z., Engrand, C., Duprat, J., Russell, S.S., Bonato, E., Ma, C., Kawamoto, T., Wada, T., Watanabe, S., Endo, R., Enju, S., Riu, L., Rubino, S., Tack, P., Takeshita, S., Takeichi, Y., Takeuchi, A., Takigawa, A., Takir, D., Tanigaki, T., Taniguchi, A., Tsukamoto, K., Yagi, T., Yamada, S., Yamamoto, K., Yamashita, Y., Yasutake, M., Uesugi, K., Umegaki, I., Chiu, I., Ishizaki, T., Okumura, S., Palomba, E.,

Pilorget, C., Potin, S.M., Alasli, A., Anada, S., Araki, Y., Sakatani, N., Schultz, C., Sekizawa, O., Sitzman, S.D., Sugiura, K., Sun, M., Dartois, E., De Pauw, E., Dionnet, Z. Djouadi, Z., Falkenberg, G., Fujita, R., Fukuma, T., Gearba, I. R., Hagiya, K., Hu, M.Y., Kato, T., Kawamura, T., Kimura, M., Kubo, M.K., Langenhorst, F., Lantz, C., Lavina, B., Lindner, M., Zhao, J., Vekemans, B., Baklouti, D., Bazi, B., Borondics, F., Nagasawa, S., Nishiyama, G., Nitta, K., Mathurin, J., Matsumoto, T., Mitsukawa, I., Miura, H., Miyake, A., Miyake, Y., Yurimoto, H., Okazaki, R., Yabuta, H., Naraoka, H., Sakamoto, K., Tachibana, S., Connolly Jr., H. C., Lauretta, D. S., Yoshitake, M., Yoshikawa, M., Yoshikawa, K., Yoshihara, K., Yokota, Y., Yogata, K., Yano, H., Yamamoto, Y., Yamamoto, D., Yamada, M., Yamada, T., Yada, T., Wada, K., Usui, T., Tsukizaki, R., Terui, F., Takeuchi, H., Takei, Y., Iwamae, A., Soejima, H., Shirai, K., Shimaki, Y., Senshu, H., Sawada, H., Saiki, T., Ozaki, M., Ono, G., Okada, T., Ogawa, N., Ogawa, K., Noguchi, R., Noda, H., Nishimura, M., Namiki, N., Nakazawa, S., Morota, T., Miyazaki, A., Miura, A., Mimasu, Y., Matsumoto, K., Kumagai, K., Kouyama, T., Kikuchi, S., Kawahara, K., Kameda, S., Iwata, T., Ishihara, Y., Ishiguro, M., Ikeda, H., Hosoda, S., Honda, R., Honda, C., Hitomi, Y., Hirata, N., Hirata, N., Hayashi, T., Hayakawa, M., Hatakeda, K., Furuya, S., Fukai, R., Fujii, A., Cho, Y., Arakawa, M., Abe,

M., Watanabe, S., and Tsuda, Y. (2022) Formation and evolution of carbonaceous asteroid Ryugu: Direct evidence from returned samples. Science 379, eabn8671. https://doi.org/science.eabn8671.

Nakashima, D., Ushikubo, T., Rudraswami, N.G., Kita, N.T., Valley, J.W., Nagao, K. (2011) Ion microprobe analyses of oxygen three-isotope ratios of chondrules from the Sayh al Uhaymir 290 chondrite using a multiple-hole disk. Meteorit. Planet. Sci. 46, 857–874.

Nakashima, D., Ushikubo, T., Zolensky, M.E., Kita, N.T. (2012a) High precision oxygen three-isotope analyses of anhydrous chondritic interplanetary dust particles. Meteorit. Planet. Sci. 47, 197–208.

Nakashima, D., Ushikubo, T., Joswiak, D.J., Brownlee, D.E., Matrajt, G., Weisberg, M.K., Zolensky, M.E., Kita, N.T. (2012b) Oxygen isotopes in crystalline silicates of comet Wild 2: A comparison of oxygen isotope systematics between Wild 2 particles and chondritic materials. Earth Planet. Sci. Lett. 357–358, 355–365.

Nakashima, D., Ushikubo, T., Kita, N.T., Weisberg, M.K., Zolensky, M.E., Ebel, D.S. (2015) Late formation of a comet Wild 2 crystalline silicate particle, Pyxie, inferred from Al-Mg chronology of plagioclase. Earth Planet. Sci. Lett. 410, 54–61.

Nakashima, D., Kimura, M., Yamada, K., Noguchi, T., Ushikubo, T., Kita, N. (2020) Oxygen

isotope study of the Asuka-881020 CH chondrite I: Non-porphyritic chondrules. Geochim. Cosmochim. Acta 290, 180-200.

Nakashima, D., Nakamura, T., Zhang, M., Kita, N., Mikouchi, T., Yoshida, H., Enokido, Y., Morita, T., Kikuiri, M., Amano, K., Kagawa, E., Yada, T., Nishimura, M., Nakato, A., Miyazaki, A., Yogata, K., Abe, M., Okada, T., Usui, T., Yoshikawa, M., Saiki, T., Tanaka, S., Nakazawa, S., Terui, F., Yurimoto, H., Noguchi, T., Yabuta, H., Naraoka, H., Okazaki, R., Sakamoto, K., Watanabe, S., Tachibana, S., Tsuda, Y. (2023) Chondrule-like objects and Ca-Al-rich inclusions in Ryugu may potentially be the oldest Solar System materials. Nature Comm. 4, 532.

Nakashima, D., Noguchi, T., Ushikubo, T., Kimura, M., Kita, N. (2024) Oxygen isotope study of the Asuka-881020 CH chondrite II: Porphyritic chondrules. Geochim. Cosmochim. Acta 373, 292–307.

Nesvorný, D., Jenniskens, P., Levinson, H.L., Bottke, W.F., Vokrouhlicky, D., Gounelle, M. (2010) Cometary origin of the zodiacal cloud and carbonaceous micrometeorites. Implications for hot debris disk. Astrophys. J. 713, 816–836.

Nittler, L.R., Alexander, C.M.O'D., Gao, X., Walker, R. M., Zinner, E. (1997) Stellar sapphires: The properties and origins of presolar Al_2O_3 in meteorites. Astrophys. J. 483,

475–495.

Nittler, L.R., Stroud, R.M., Trigo-Rodríguez, J.M., De Gregorio, B.T., Alexander, C.M.O'D., Davidson, J., Moyano-Cambero, C.E., and Tanbakouei, S. (2019) A cometary building block in a primitive asteroidal meteorite. Nat. Astron. 3, 659–66.

Noguchi, T., Nakamura, T., Nozaki, W. (2003) Mineralogy of phyllosilicate-rich micrometeorites and comparison with Tagish Lake and Sayama meteorites. Earth Planet. Sci. Lett. 202, 229–246.

Noguchi, T., Nakamura, T., Okudaira, K., Yano, H., Sugita, S., and Burchell, M.J. (2007) Thermal alteration of hydrated minerals during hypervelocity capture to silica aerogel at the flyby speed of Stardust. Meteoritics Planet. Sci., 42, 357–372.

Noguchi, T., Nakamura, T., Ushikubo, T., Kita, N.T., Valley, J.W., Yamanaka, R., Kimoto, Y., Kitazawa, Y. (2011) A chondrule-like object captured by space-exposed aerogel on the international space station. Earth. Planet. Sci. Lett. 309, 198–206.

Noguchi, T., Ohashi, N., Tsujimoto, S., Mitsunari, T., Bradley, J.P., Nakamura, T., Toh, S., Stephan, T., Iwata, N., Imae, N. (2015) Cometary dust in Antarctic ice and snow: Past and present chondritic porous micrometeorites preserved on the Earth's surface. Earth Planet. Sci. Lett. 410, 1–11.

Noguchi, T., Yabuta, H., Itoh, S., Sakamoto, N., Mitsunari, T., Okubo, A., Okazaki, R., Nakamura, T., Tachibana, S., Terada, K., Ebihara, M., Imae, N., Kimura, M., Nagahara, H. (2017) Variation of mineralogy and organic matter during the early stages of aqueous activity recorded in Antarctic micrometeorites. Geochim. Cosmochim. Acta 208, 119–144.

Noguchi, T., Yasutake, M., Tsuchiyama, A., Miyake, A., Kimura, M., Yamaguchi, A., Imae, N., Uesugi, K., Takeuchi, A. (2021) Mineralogy of fine-grained matrix, fine-grained rim, chondrule rim, and altered mesostasis of a chondrule in Asuka 12169, one of the least altered CM chondrites. Polar Sci. 29, 100727.

Noguchi, T., Matsumoto, R., Yabuta, H., Kobayashi, H., Miyake A., Naraoka. H., Okazaki, R., Imae, N., Yamaguchi, A., David Kilcoyne, A.L., Takeichi, Y., Takahashi, Y. (2022) Antarctic micrometeorite composed of CP and CS IDP-like material: A micro-breccia originated from a partially ice-melted comet-like small body. Meteorit. Planet. Sci. 57, 2042–2062.

Norris, T.L., Gancarz, A.J., Rokop, D.J., Thomas, K.W. (1983) Half-life of ^{26}Al. J. Geophys. Res. 88, B331–333.

Nuth, III, J.A., Hill, H.G.M., Kletetschka, G. (2000) Determining the ages of comets from

the fraction of crystalline dust. Nature 406, 257–276.

Ogliore, R.C., Huss, G.R., Nagashima, K., Butterworth, A.L., Gainsforth, Z., Stodolna, J., Westphal, A.J., Joswiak, D., Tyliszczak, T. (2012) Incorporation of a late-forming chondrule into comet Wild 2. Astrophys. J. 745, L19–24.

Ohtaki, K.K., Ishii, H.A., Bradley, J.P., Villalon, K.L., Davis, A.D., Stephan, T., Bustillo, K.C., Ciston, J. (2021) Search for meteoritic GEMS I: Comparison of amorphous silicates in Paris and Acfer 094 chondrite matrices and in anhydrous chondritic interplanetary dust particles. Geochim. Cosmochim. Acta 310, 320–45.

Reach, W.T. (2010) Structure of the Earth's circumsolar dust ring. Icarus 209, 848–850.

Rietmeijer, F.J.M. (1991) Aqueous alteration in five chondritic porous interplanetary dust particles. Earth Planet. Sci. Lett. 102, 148–157.

Schrader, D.L., Connolly, Jr., H.C., Lauretta, D.S. (2008) Opaque phases in type-II chondrules from CR2 chondrites: Implications for CR chondrite parent body formation. Geochim. Cosmochim. Acta 72, 6124–6140.

Schrader, D.L., Connolly, Jr., H.C., Lauretta, D.S., Nagashima, K., Huss, G.R., Davidson, J., Domanik, K.J. (2011) The formation and alteration of the Renazzo-like carbonaceous chondrites I: Implications of bulk-oxygen isotopic composition. Geochim. Cosmochim.

Acta 75, 308–325.

Schrader, D.L., Connolly, Jr., H.C., Lauretta, D.S., Nagashima, K., Huss, G.R., Davidson, J., Domanik, K.J. (2013) The formation and alteration of the Renazzo-like carbonaceous chondrites II: Linking O-isotope composition and oxidation state of chondrule olivine. Geochim. Cosmochim. Acta 101, 302–327.

Schrader, D.L., Nagashima, K., Krot, A.N., Ogliore, R.C., Hellebrand, E. (2014) Variations in the O-isotope composition of gas during the formation of chondrules from the CR chondrites. Geochim. Cosmochim. Acta 132, 50–74.

Schrader, D.L., Connolly, Jr., H.C., Lauretta, D.S., Zega, T.J., Davidson, J., Domanik, K.J. (2015) The formation and alteration of the Renazzo-like carbonaceous chondrites III: Toward understanding the genesis of ferromagnesian chondrules. Meteorit. Planet. Sci. 50, 15–50.

Schrader, D.L., Davidson, J. (2017) CM and CO chondrites: A common parent body or asteroidal neighbors? Insights from chondrule silicates. Geochim. Cosmochim. Acta 214, 157–171.

Schrader, D.L., Nagashima, K., Krot, A.N., Ogliore, R.C., Yin, Q-Z., Amelin, Y., Stirling, C.H., Kaltenbach, A. (2017) Distribution of ^{26}Al in the CR chondrite chondrule-forming

region of the protoplanetary disk. Geochim. Cosmochim. Acta 201, 275–302.

Schrader, D.L., Nagashima, K., Waitukaitis, S.R., Davidson, J., McCoy, T.J., Connolly, Jr., H.C., Lauretta, D.S. (2018) The retention of dust in protoplanetary disks: Evidence from agglomeratic olivine chondrules from the outer Solar System. Geochim. Cosmochim. Acta 223, 405–421.

Schrader, D.L., Davidson, J., McCoy, T.J., Zega, T.J., Russell, S.S., Domanik, K.J., King, A.J. (2021) The Fe/S ratio of pyrrhotite group sulfides in chondrites: An indicator of oxidation and implications for return samples from asteroids Ryugu and Bennu. Geochim. Cosmochim. Acta 303, 66–91.

Schrader, D.L., Davidson, J. (2022) Prolonged early migration of dust from the inner Solar System to the comet-forming region. Earth Planet. Sci. Lett. 589, 117552.

Schwander, D., Kööp, L., Berg, T., Schönhense, G., Heck, P.R., Davis, A.M., Ott, U. (2015) Formation of refractory metal nuggets and their link to the history of CAIs. Geochim. Cosmochim. Acta 168, 70–87.

Simon, S. B., Grossman, L., Hutcheon, I.D., Phinney, D.L., Weber, P., Fallon, S.J. (2006) Formation of spinel-, hibonite-rich inclusions found in CM2 carbonaceous chondrites. Am. Mineral. 91, 1675–1687.

Simon, S.B., Joswiak, D.J., Ishii, H.A., Bradley, J.P., Chi M., Grossman L., Aléon, J., Brownlee, D.E., Fallon S., Hutcheon, I.D., Matrajt, G., McKeegan, K.D. (2008) A refractory inclusion returned by Stardust from comet 81P/Wild2. Meteorit. Planet. Sci. 43, 1861–1877.

Slodzian, G., Hillion, F., Stadermann, F.J., Zinner, E. (2004) QSA influences on isotopic ratio measurements. Applied Surface Science 231–232, 874–877.

Suttle, M.D., Genge, M.J., Salge, T., Lee, M.R., Folco, L., Góral, T., Russell, S.S., Lindgren, P. (2019) A microchondrule-bearing micrometeorite and comparison with microchondrules in CM chondrites. Meteorit. Planet. Sci. 54, 1303–1324.

Tenner T.J., Ushikubo T., Kurahashi E., Kita N.T. Nagahara H. (2013) Oxygen isotope systematics of chondrule phenocrysts from the CO3.0 chondrite Yamato 81020: evidence for two distinct oxygen isotope reservoirs. Geochim. Cosmochim. Acta 102, 226–245.

Tenner, T.J., Nakashima, D., Ushikubo, T., Kita, N.T., Weisberg, M.K. (2015) Oxygen isotope ratios of FeO-poor chondrules in CR3chondrites: Influence of dust enrichment and H_2O during chondrule formation. Geochim. Cosmochim. Acta 148, 228–250.

Ushikubo, T., Kimura, M., Kita, N.T., Valley, J.W. (2012) Primordial oxygen isotope reservoirs of the solar nebula recorded in chondrules in Acfer 094 carbonaceous

chondrite. Geochim. Cosmochim. Acta 90, 242–264.

Ushikubo, T., Nakashima, D., Kimura, M., Tenner, T.J., Kita, N.T. (2013) Contemporaneous formation of chondrules in distinct oxygen isotope reservoirs. Geochim. Cosmochim. Acta 109, 280–295.

Ushikubo, T., Kimura, M. (2021) Oxygen-isotope systematics of chondrules and olivine fragments from Tagish Lake C2 chondrite: Implications of chondrule-forming regions in protoplanetary disk. Geochim. Cosmochim. Acta 293, 328–343.

Valley, J., Kita, N.T. (2009) Chapter 2: In situ oxygen isotope geochemistry by ion microprobe. in Fayek, M. (Ed.) Secondary ion mass spectrometry in the earth sciences: Gleaning the big picture from a small spot, Mineralogical Association of Canada Short Course 41, Fayek, M. Ed. (Mineralogical Association of Canada, Toronto), pp. 19–63.

Vernazza, P., Marsset, M., Beck, P., Binzel, R.P., Birlan, M., Brunetto, R., Demeo, F.E., Djouadi, Z., Dumas, C., Merouane, S., Mousis, O., Zanda, B. (2015) Interplanetary dust particles as samples of icy asteroids. Astrophys. J. 806, 204.

Vernazza, P., Castillo-Rogez, J., Beck, P., Emery, J., Brunetto, R., Delbo, M., Marsset, M., Marchis, F., Groussin, O., Zanda, B. (2017) Different origins of different evolution? Decoding the spectral diversity among C-type asteroids. Astronom. J. 153, 72 (10pp).

Vernazza, P. Ferrais, M., Jorda, L., Hanuš, J., Carry, B., Marsset, M., Brož, M., Fetick, R., Viikinkoski, M., Marchis, F., Vachier, F., Drouard, A., Fusco, T., Birlan, M., Podlewska-Gaca, E., Rambaux, N., Neveu, M., Bartczak, P., Dudziński, G., Jehin, E., Beck, P., Berthier, J., Castillo-Rogez, J., Cipriani, F., Colas, F., Dumas, C., Ďurech, J., Grice, J., Kaasalainen, M., Kryszczynska, A., Lamy, P., Le Coroller, H., Marciniak, A., Michalowski, T., Michel, P., Santana-Ros, T., Tanga, P., Vigan, A., Witasse, O., Yang, B., Antonini, P., Audejean, M., Aurard, P., Behrend, R., Benkhaldoun, Z., Bosch, J. M., Chapman, A., Dalmon, L., Fauvaud, S., Hamanowa, H., Hamanowa, H., His, J., Jones, A., Kim, D.-H., Kim, M.-J., Krajewski, J., Labrevoir, O., Leroy, A., Livet, F., Molina, D., Montaigut, R., Oey, J., Payre, N., Reddy, V., Sabin, P., Sanchez, A. G., Socha, L. (2021) VLT/SPHERE imaging survey of the largest main-belt asteroids: Final results and synthesis. Astronom. Astrophys. 654, A56.

Villalon, K.L., Ohtaki, K.K., Bradley, J.P., Ishii, H.A., Davis, A.M., Stephan, T. (2021) Search for meteoritic GEMS II: Comparison of inclusions in amorphous silicates from the Paris Chondrite and from anhydrous chondritic interplanetary dust particles. Geochim. Cosmochim. Acta 310, 346–62.

Weisberg M.K., Ebel D.S., Connolly, Jr., H.C., Kita N.T., Ushikubo T. (2011) Petrology and

oxygen isotope compositions of chondrules in E3 chondrites. Geochim. Cosmochim. Acta 75, 6556–6569.

Yamanobe, M., Nakamura, T., Ushikubo, T. (2018) Oxygen isotope reservoirs in the outer asteroid belt inferred from oxygen isotope systematics of chondrule olivines and isolated forsterite and olivine grains in Tagish Lake-type carbonaceous chondrites, WIS 91600 and MET 00432. Polar Sci. 15, 29–38.

Zhang, M., Defouilloy, C., Joswiak, D.J., Brownlee, D.E., Nakashima, D., Siron, G., Kitajima, K., Kita, N.T. (2021) Oxygen isotope systematics of crystalline silicates in a giant cluster IDP: A genetic link to Wild 2 particles and primitive chondrite chondrules. Earth Planet. Sci. Lett. 564, 116928.

Zolensky, M.E. (1987) Refractory interplanetary dust particles. Science 237, 1466-1468.

Zolensky, M.E., Barett, R. (1994) Olivine and pyroxene compositions of chondritic interplanetary dust particles. In Analysis of interplanetary dust, AIP Conference Proceedings 310, Zolensky, M.E., Wilson, T.L., Rietmeijer, F.J.M., Flynn, G.J. Eds. (American Institute of Physics, New York), pp. 105–114.

Zolensky M. E., Thomas K. (1995) Iron and iron-nickel sulfides in chondritic interplanetary dust particles. Geochim. Cosmochim. Acta 59, 4707–4712.

Zolensky, M.E., Zega, T.J., Yano, H., Wirick, S., Westphal, A.J., Weisberg, M.K., Weber, I., Warren, J.L., Velbel, M.A., Tsuchiyama, A., Tsou, P., Toppani, A., Tomioka, N., Tomeoka, K., Teslich, N., Taheri, M., Susini, J., Stroud, R., Stephan, T., Stadermann, F.J., Snead, C.J., Simon, S.B., Simionovici, A., See, T.H., Robert, F., Rietmeijer, F.J.M., Rao, W., Perronnet, M.C., Papanastassiou, D.A., Okudaira, K., Ohsumi, K., Ohnishi, I., Nakamura-Messenger, K., Nakamura, T., Mostefaoui, S., Mikouchi, T., Meibom, A., Matrajt, G., Marcus, M.A., Leroux, H., Lemelle, L., Le, L., Lanzirotti, A., Langenhorst, F., Krot, A.N., Keller, L.P., Kearsley, A.T., Joswiak, D., Jacob, D., Ishii, H., Harvey, R., Hagiya, K., Grossman, L., Grossman, J.N., Graham, G.A., Gounelle, M., Gillet, Ph., Genge, M.J., Flynn, G., Ferroir, T., Fallon, S., Ebel, D.S., Dai, Z.R., Cordier, P., Clark, B., Chi, M., Butterworth, A.L., Brownlee, D.E., Bridges, J.C., Brennan, S., Brearley, A., Bradley, J.P., Bleuet, P., Bland, P.A., Bastien, R. (2006) Mineralogy and petrology of comet 81P/Wild 2 nucleus samples. Science 314,1735–1739.

Zolensky, M., Nakamura-Messenger, K., Rietmeijer, F., Leroux, H., Mikouchi, T., Ohsumi, K., Simon, S., Grossman, L., Stephan, T., Weisberg, M., Velbel, M., Zega, T., Stroud, R., Tomeoka, K., Ohnishi, I., Tomioka, N., Nakamura, T., Matrajt, G., Joswiak, D., Brownlee, D., Langenhorst, F., Krot, A., Kearsley, A., Ishii, H., Graham, G., Dai, Z., Chi,

M., Bradley, J., Hagiya, K., Gounelle, M., Keller, L., Bridges, J. (2008) Comparing Wild 2 particles to chondrites and IDPs. Meteorit. Planet. Sci. 43, 261–272.

Tables

Table 1

Chemical compositions of minerals and glass obtained by electron microprobe analyzer given in wt.%.

Sample	Mineral	Types	SiO_2	TiO_2	ZrO_2	Al_2O_3	Cr_2O_3	V_2O_3	Y_2O_3	FeO	NiO	MnO	MgO	CaO	Na_2O	K_2O	P_2O_5	SO_3	Total	Mg/(Mg+Fe)
D03IB64	Olivine	BO CLO	36.61	0.11	n. m.	0.83	0.18	n. m.	n. m.	19.73	b. d.	0.45	37.37	0.45	0.17	b. d.	b. d.	b. d.	95.9	0.771
D03IB64	Glass	BO CLO	52.1	0.16	n. m.	12.67	0.22	n. m.	n. m.	10.98	0.04	0.15	17.27	2.54	2.4	0.27	0.06	0.05	98.91	0.737
D05IB66	Olivine	POP CLO	38.18	0.1	n. m.	0.54	0.32	n. m.	n. m.	19.69	0.14	0.35	39.22	0.34	b. d.	b. d.	b. d.	b. d.	98.87	0.78
D05IB66	Olivine	POP CLO	39.07	b. d.	n. m.	b. d.	0.25	n. m.	n. m.	18.62	b. d.	0.69	40.02	0.22	b. d.	b. d.	b. d.	b. d.	98.88	0.793
D05IB66	Low-Ca pyroxene	POP CLO	59.58	0.11	n. m.	0.52	0.5	n. m.	n. m.	0.57	b. d.	0.1	38.6	0.48	b. d.	b. d.	b. d.	b. d.	100.45	0.992
D05IB66	Low-Ca pyroxene	POP CLO	54.53	0.09	n. m.	2.13	1.06	n. m.	n. m.	9.91	b. d.	0.48	29.8	1.37	b. d.	b. d.	b. d.	b. d.	99.37	0.843
D05IB66	Glass	POP CLO	56.92	0.2	n. m.	19.4	b. d.	n. m.	n. m.	3.03	b. d.	0.17	8.08	7.96	4.86	0.17	b. d.	b. d.	100.8	0.826
L2036 #20	Olivine	KOOL grain	36.98	b. d.	n. m.	b. d.	0.1	n. m.	n. m.	26.04	b. d.	0.53	33.36	0.44	b. d.	b. d.	b. d.	b. d.	97.45	0.695
L2036 #20	High-Ca pyroxene	KOOL grain	53.26	0.37	n. m.	0.48	3.08	n. m.	n. m.	4.49	b. d.	0.28	16.37	18.15	1.86	b. d.	b. d.	b. d.	98.34	0.867
L2036 #20	Glass	KOOL grain	63.36	0.28	n. m.	10.8	b. d.	n. m.	n. m.	3.72	b. d.	0.14	7.01	1.67	6.19	2.04	2.46	b. d.	97.65	0.77
D05IB084	Spinel	SHIB	0.06	0.28	n. m.	70.99	b. d.	0.51	n. m.	0.1	b. d.	b. d.	27.92	b. d.	b. d.	b. d.	b. d.	b. d.	99.87	0.998
D05IB084	Hibonite	SHIB	0.75	4.06	b. d.	84.84	b. d.	0.35	0.11	b. d.	b. d.	b. d.	2.14	7.65	b. d.	b. d.	b. d.	b. d.	99.88	-
D05IB084	Perovskite	SHIB	0.36	53.95	2.05	0.81	b. d.	b. d.	1.42	0.31	b. d.	b. d.	b. d.	36.32	b. d.	b. d.	b. d.	b. d.	95.22	-

CLO: chondrule-like object, n. n.: not measured, b. d.: below detection limits

Table 2

Solar flare track densities in the four samples.

Sample name	Track density (no. of grains)	Measured minerals in matrix	Coarse-grained object
D03IB64	$>8 \times 10^{10}$ cm^{-2} (n = 5)	High-Ca pyroxene, olivine	BO CLO
L2036#20	$3–4 \times 10^{10}$ cm^{-2} (n = 2)	Low-Ca pyroxene, olivine	KOOL grain
D05IB66	Not identified	-	POP CLO
D05IB84	3×10^{10} cm^{-2} (n = 2)	Low-Ca pyroxene	SHIB

Table 3
Oxygen three-isotope ratios measured by ion microprobe from 2-micrometer spots*.

Sample	Mineral	SIMS spot	$\delta^{18}O$ ‰	2SD ‰	$\delta^{17}O$ ‰	2SD ‰	$\Delta^{17}O$	2SD ‰
D03IB064	Olivine + Glass	1	2.2	1.2	1.0	0.9	-0.2	0.5
D03IB064	Olivine + Glass	2	1.5	1.2	0.0	0.9	-0.8	0.5
D03IB064	Olivine + Glass	3	-1.4	1.2	-0.7	0.9	0.0	0.5
D03IB064	Olivine + Glass	4	0.7	1.2	-1.8	0.9	-2.1	0.5
D03IB064	Olivine + Glass	5	0.7	1.2	0.1	0.9	-0.3	0.5
D05IB66	Olivine	21	3.7	1.1	1.5	1.54	-0.4	1.6
D05IB66	Low-Ca pyroxene	22	0.7	1.1	-2.6	1.54	-3.0	1.6
D05IB66	Low-Ca pyroxene	23	1.6	1.1	-1.6	1.54	-2.5	1.6
D05IB66	Low-Ca pyroxene	24	-5.7	1.1	-8.5	1.54	-5.6	1.6
D05IB66	Low-Ca pyroxene	25	3.3	1.1	0.8	1.54	-0.9	1.6
D05IB66	Low-Ca pyroxene	26	-5.8	1.1	-9.9	1.54	-6.8	1.6
D05IB66	Olivine	27	4.1	1.1	1.3	1.54	-0.8	1.6
L2036 #20	Olivine	1	9.4	2.0	8.2	1.2	3.3	1.1
L2036 #20	Olivine	2	7.4	2.0	7.2	1.2	3.4	1.1
L2036 #20	Olivine	3	5.8	2.0	5.9	1.2	2.9	1.1
L2036 #20	High-Ca pyroxene	7	9.7	2.0	7.6	1.2	2.6	1.1
L2036 #20	High-Ca pyroxene	8	8.9	2.0	6.5	1.2	1.9	1.1
L2036 #20	Olivine	9	6.5	2.0	5.6	1.2	2.2	1.1
D05IB084	Spinel	1	-45.1	1.9	-46.3	1.4	-22.8	1.2
D05IB084	Spinel	2	-44.3	1.9	-45.0	1.4	-21.9	1.2
D05IB084	Spinel	3	-43.8	1.9	-44.8	1.4	-22.0	1.2
D05IB084	Spinel	4	-44.7	1.9	-46.8	1.4	-23.6	1.2

*Data are corrected for instrumental biases and a contribution of tailing from hydride (^{16}OH) peak on ^{17}O. The uncertainties of individual analyses are estimated from spot-to-spot reproducibility (2SD) of standard olivine analyses (n=6) in the same epoxy disk, though those associated with hydride corrections are not included.

Table 4

The Al-Mg isotope analyses of hibonite and spinel in D05IB84.

Spot #	$^{27}Al/^{24}Al \pm 2\sigma$ (‰)		$\delta^{26}Mg^* \pm 2\sigma$ (‰)		Target
1	35.35	1.15	13.2	2.1	Hibonite
2	43.49	1.45	13.9	2.9	Hibonite
3	2.61	0.03	-0.1	1.0	Spinel
4	2.58	0.03	1.1	1.0	Spinel
5	2.62	0.03	0.4	1.1	Spinel

Figure Captions

Figure 1 Secondary electron (SE) images of three Antarctic micrometeorites (AMMs) and an interplanetary dust particle (IDP) investigated in this study. All the samples were placed on a Pt plate. All the samples seem to be solid and are coated by sub-µm-sized material. (a) D03IB64, (b) D05IB66, (c) L2036#20, (d) D05IB84.

Figure 2 Bright-field transmission electron microscope (BF-TEM) images of ultrathin sections of the AMMs and IDP investigated in this study. These ultrathin sections were selected from the beginning sections because they contain both projecting parts of a solid interior (chondrule-like objects or CAI) and a sub-µm-sized matrix. Because chondrule-like objects and a CAI are composed of coarse-grained minerals, they were shuttered into shards, and most shards were lost during ultramicrotomy. (a) D03IB64, (b) D05IB66, (c) L2036#20, (d) D05IB84.

Figure 3 Backscattered electron (BSE) images of two chondrule-like objects, a KOOL grain, and a CAI in 3 AMMs and an IDP. a) D03IB64, b) D05IB66, c) L2036 #20, d) D05IB84. Ol: olivine, px: pyroxene, Pyh: pyrrhotite, Chr: chromite, Spl: spinel, Hbn: hibonite, Pv:

perovskite, Fe-Ni slf: Fe-Ni sulfide, Alt: alteration product (enclosed by a dotted curve).

Figure 4 BSE image and the corresponding electron backscattered diffraction (EBSD) map with pole figures. The common crystallographic orientation of olivine (blue) confirms the chondrule-like object in D03IB64 shares a common characteristic with typical meteoritic BO chondrules.

Figure 5 (a) Silicon and CI chondrite normalized bulk elemental abundances of the chondrule-like objects (CLOs) in D03IB64 and D05IB66 and the KOOL grain in L2036#20 and the Si and CI chondrite normalized elemental abundances of glass in these objects. (b) The ranges of the Si and CI chondrite normalized elemental abundances of glass in these chondrules and the KOOL grain are represented by the bars with the same colors as those in (a). Data of the MET 00526 L/LL3.05 and MET 00426 CR3.0 meteorites, those of the PRE 95404 R3 meteorite, and those of the KOOL grains are from Berlin (2009; Berlin et al., 2011), Miller et al. (2017), and Joswiak et al. (2009), respectively. The bulk elemental abundances of the CLOs and the KOOL grain were weighted averages of minerals and glass obtained by FE-EPMA. Elemental abundances

of chondrules glass were obtained by FE-EPMA. For comparison, (a) the ranges of the Si and CI chondrite normalized bulk elemental abundances and (b) the ranges of the Si and CI chondrite normalized elemental abundances of glass in type I and type II chondrules in L/LL3.05, CR3.0, and R3 chondrites, and those of the kosmochloric Ca-rich pyroxene and FeO-rich olivine-bearing objects (KOOL grain) Coki-A in a Stardust sample recovered from 81P/Wild2 comet are plotted as orange, pale orange, green, light green, purple, and light blue.

Figure 6 Chemical compositions of olivine and pyroxene in the two CLOs, one KOOL grain, and the fine-grained matrices including D05IB84. (a) Histogram of Fa mol% in olivine. (b) Histogram of Fs mol% in low-Ca pyroxene. Olivine and pyroxene in CLOs and a KOOL grain appear as hatched bins in (a) and (b). (c) Pyroxene chemical compositions are plotted on a quadrilateral diagram. Chemical compositions of olivine in a chondrule-like object in D05IB66 and the KOOL grain in L2036 #20 were obtained by FE-EPMA. Chemical compositions of olivine and pyroxene in the chondrule-like object in D03IB64 the fine-grained matrices were measured by EDS equipped on (S)TEM due to their small sizes. (d) Chemical compositions of high-Ca pyroxene in the KOOL grain are plotted on

a Ca-Na-Cr atomic ternary diagram. This diagram shows that the high-Ca pyroxene is enriched in the kosmochlor component. The compositional field of high-Ca pyroxene in KOOL grains in both Stardust samples and IDPs is shown as a green area (Joswiak et al., 2009).

Figure 7 MnO and Cr_2O_3 contents vs. FeO contents of olivine and low-Ca pyroxene in two CLOs, a grain, and the fine-grained matrices including D05IB84. (a) MnO vs. FeO diagram and (b) Cr_2O_3 vs FeO diagram. The dashed lines indicate the detection limits of MnO and Cr_2O_3 using EDS equipped on (S)TEM. Thin solid lines indicate the solar ratio between FeO and MnO, and FeO and Cr_2O_3, respectively. Gray color areas in the diagrams are compositional fields of olivine in CP and CS IDPs, the fine-grained matrices of primitive chondrites, and the Wild2 samples (Klöck et al., 1989; Zolensky et al., 2008; Frank et al., 2014).

Figure 8 Molar Fe/Mn vs. molar Fe/Mg diagram of olivine in the two chondrule-like objects and the KOOL grain investigated. Olivines in the CLOs called Torajiro (Nakamura et al., 2008) and Iris (Gainsforth et al. 2015), the KOOL grain Puki recovered from comet

81P/Wild 2, olivine in CLOs and mineral fragments (MFs) in a giant cluster IDP U2-20GCA (Zhang et al. 2021), and the CLO captured at the international space station (ISS) (Noguchi et al. 2010) were also plotted. In addition, olivine compositions in chondrules in CM2, CR2, and L/LL3 chondrites (Schrader et al., 2015; Schrader and Davidson, 2017 and 2022) are plotted for comparison. The olivine crystals in the BO-like CLO and the two KOOL grains plot around the median value of that in L/LL3 chondrites and near the lowest molar Fe/Mn end of the compositional field of CR chondrites. The POP CLO, Trajiro, and the CLO captured at the ISS are plotted near the lowest end of L/LL3. In contrast, Iris are plotted between the medians of L/LL3 and CR2, and the CLOs and MFs in IDP U2-20GCA are plotted from above the median of CM to the median of L/LL3.

Figure 9 Fe-Ni sulfides in the two CLOs, the KOOL grain, and the fine-grained matrices in all the investigated samples are plotted on Fe-Ni-S ternary diagrams. Chemical compositions of Fe-Ni sulfides were measured by EDS equipped on (S)TEM. Fe-Ni sulfides in the CLOs and the KOOL grain appear as red diamonds and those in the fine-grained matrix as yellow circles. Compositional fields of monosulfide solid solution (Mss), high-temperature pentlandite, and liquid (sulfide melt) at 800 ^{o}C are indicated in

the diagram of L20356 #20. These fields are from Kitakaze et al. (2011).

Figure 10 TEM images of phases in the fine-grained matrices in the three AMMs and an IDP: (a), (e), (h) D03IB64; (b) D05IB66; (c), (f), (i) L2036 #20, (d), (g), (j) D05IB84. (a) to (d) show GEMS. Panels (b), (e) to (g) show enstatite whiskers and platelets. (h) shows a solar flare track-rich high-Ca pyroxene, and (i) and (j) show solar flare track-rich olivine crystals. (h) Solar flare tracks appear thin white lines in the dark-field image. (i) and (j) Solar flare tracks appear as thin black lines indicated by arrowheads in the bright-field images.

Figure 11 HAADF-STEM images and corresponding Fe, Ni, S, and Si elemental maps of GEMS in the three AMMs and an IDP: (a) D03IB64, (b) D05IB66, (c) L2036 #20, (d) D05IB84. Comparing Fe, Ni, and S elemental maps, GEMS in D03IB64, D05IB66, and L2036 #20 contains both Fe-Ni metal and Fe(-Ni) sulfide although relative amounts of them are variable among samples. Comparing Fe and Si elemental maps, amorphous silicate in GEMS is very poor in Fe. In contrast, when comparing Fe, Ni, and S elemental maps, GEMS in D05IB84 does not contain Fe-Ni metal but Fe(-Ni) sulfide. In addition,

comparing Fe and Si elemental maps, amorphous silicate in GEMS in D05IB84 contains a detectable amount of Fe, indicated by an arrow in the Fe elemental map in (d).

Figure 12 Three oxygen isotopic plots of silicates and oxides in the two CLOs, one KOOL grain, and a SHIB fragment and the correspondence between the analyzed points and their isotopic ratios. Numbers on backscatter electron images of each sample correspond to those in (a), (b), (c), (e), (f) to the numbers in the four oxygen isotopic diagrams in (a) to (c) and in the Mg-Al isotopic systematics diagram in (e). (a) Oxygen isotopic compositions of the BO-like CLO in D03IB64 were obtained from a mixture of olivine and interstitial glass due to their small sizes. (b) Oxygen isotopic compositions of olivine and low-Ca pyroxene in the POP CLO in D05IB66 were measured. (c) Oxygen isotopic compositions of olivine and high-Ca pyroxene in the KOOL grain in L2036 #20 were measured. (d) A compilation of the oxygen isotopic compositions of olivine and pyroxenes in the following meteorites, 81P/Wild 2 comet samples, IDPs, and AMMs to compare them with the results obtained in this study. The data used to prepare this compilation are as follows: CH and CB chondrites (CH-CB), CR chondrites (CR), O and R chondrites (O-R), E and K chondrites (E-K), CV, CO, and CM chondrites with Acfer

094 ungrouped carbonaceous chondrite (CV-CO-CM-Acfer 094), Wild 2 cometary dust recovered by Stardust spacecraft (Wild 2), IDPs, and AMMs (Krot et al, 2010; Connolly and Huss, 2010; Schrader et al., 2013, 2014; Tenner et al., 2015; Hertwig et al., 2018; Tenner et al., 2013; Chaumard et al., 2018; Ushikubo et al., 2012; Kita et al., 2010; Miller et al., 2017; Nagashima et al., 2015; Weisberg et al., 2011; Nakashima et al., 2012; Defouilloy et al., 2017; Aléon et al., 2009; Zhang et al., 2021; Engrand et al., 1999; Gounelle et al., 2005). In (a) to (d), the terrestrial fractionation (TF) line, the primitive chondritic materials (PCM) line (Ushikubo et al., 2012), and the carbonaceous chondrite anhydrous minerals (CCAM) line (Clayton et al., 1977) are also plotted as reference lines. (e) Oxygen isotopic compositions of spinel in the SHIB fragment in D05IB84 were measured. (f) Mg-Al isotopic systematics of spinel and hibonite in the SHIB in D05IB84 were investigated. Mg and Al isotopes of spinel and hibonite were measured. Error bars in (a), (b), (c), and (f) represent 2σ. The numbers on the BSE images in (a), (b), (c), (e), and (f) correspond to those on the corresponding diagrams.

Figure 13 Relationship between Mg# and $\Delta^{17}O$ of olivine and pyroxene in the two CLOs and the KOOL grain investigated in this study. The data of Stardust samples (Defouilloy

et al., 2017) and olivine and pyroxene in chondrule-like objects and coarse mineral fragments in a giant cluster IDP (Zhang et al., 2021) are also plotted for comparison. Error bars are 2σ. Contours are mixing lines among the solar nebular gas with –28‰, anhydrous CI-like dust with −6‰, and H_2O ice with +5‰, according to Tenner et al. (2015).

Figure 14 NanoSIMS data on D03IB64. (a) Left: $\delta^{13}C$ and $\delta^{15}N$ values of bulk samples and isotopically anomalous hotspots. Right: $^{28}Si^-$ ion image (upper right) and $^{12}C^{15}N^-/^{12}C^{14}N^-$ ratio image (upper left) of an ultrathin section. Arrows show hotspots with significant ^{15}N enrichments. (b) Left: The O isotopic composition of a presolar silicate grain. Also shown are data on presolar silicate and oxide grains reported previously in the Presolar Grain Database (Hynes and Gyngard, 2009). Right: $^{17,18}O/^{16}O^-$ ratio images of another ultrathin section. The arrow shows a presolar grain with an ^{17}O enrichment and an ^{18}O depletion.

Figures

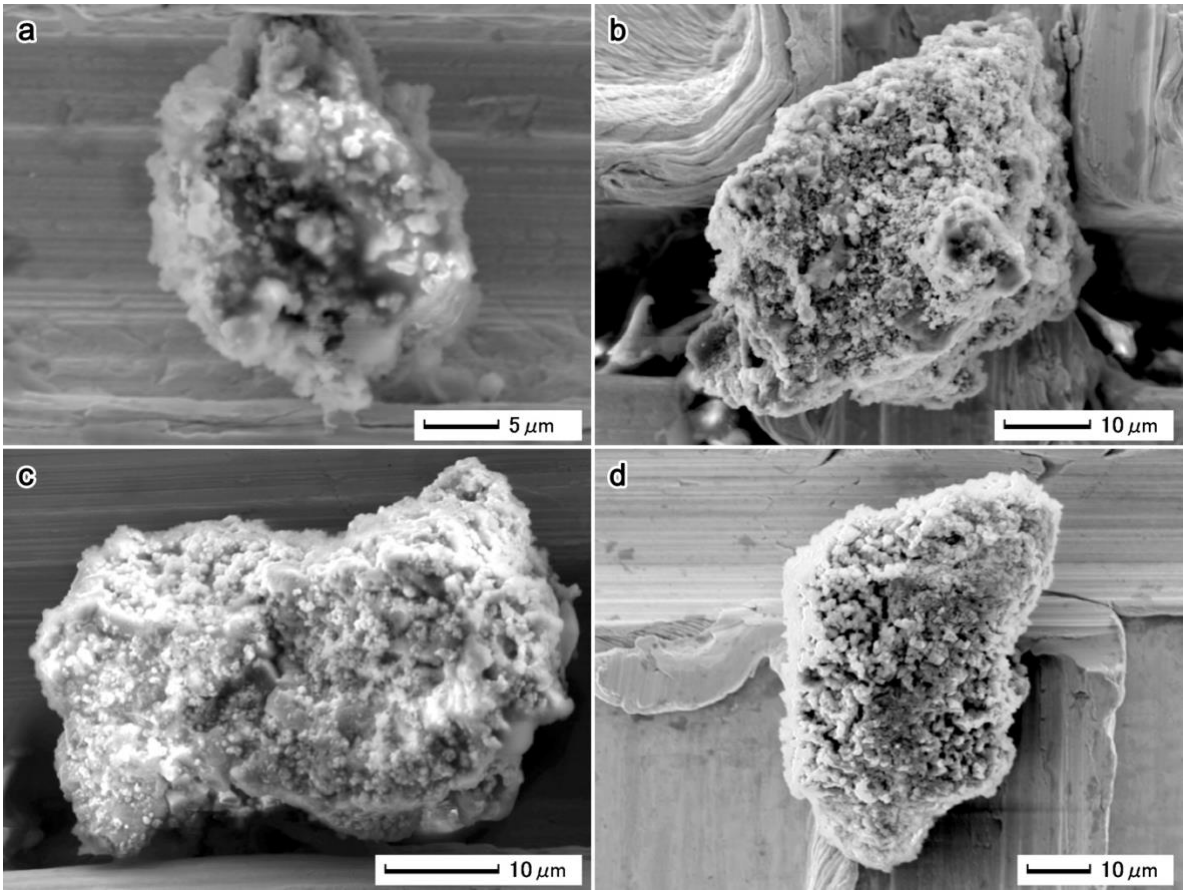

Figure 1

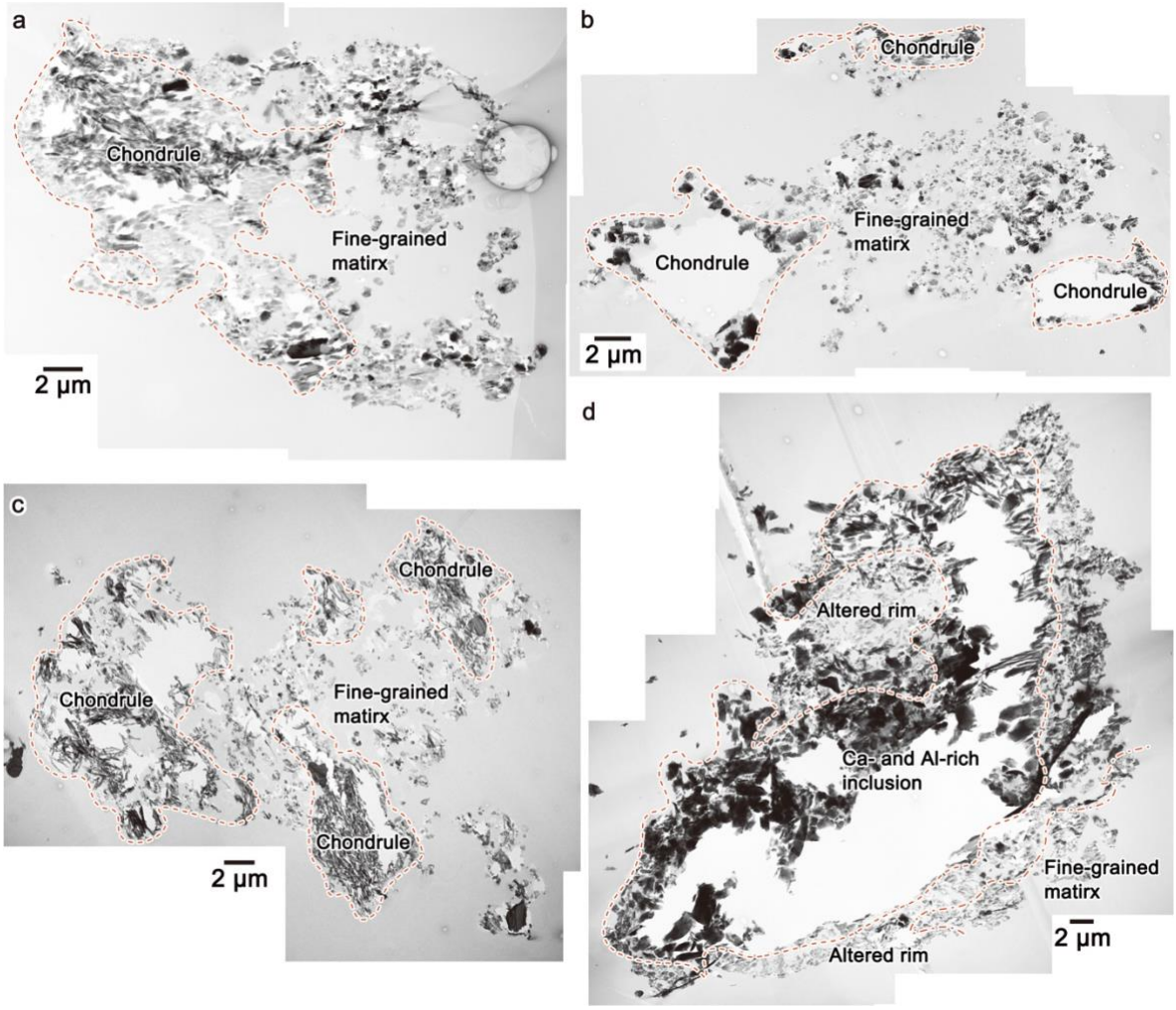
a
Chondrule
Fine-grained
matirx
2 μm
b
Chondrule
Fine-grained
matirx
Chondrule
Chondrule
2 μm
c
Chondrule
Chondrule
Fine-grained
matirx
Chondrule
2 μm
d
Altered rim
Ca- and Al-rich
inclusion
Fine-grained
matirx
Altered rim
2 μm

Figure 2

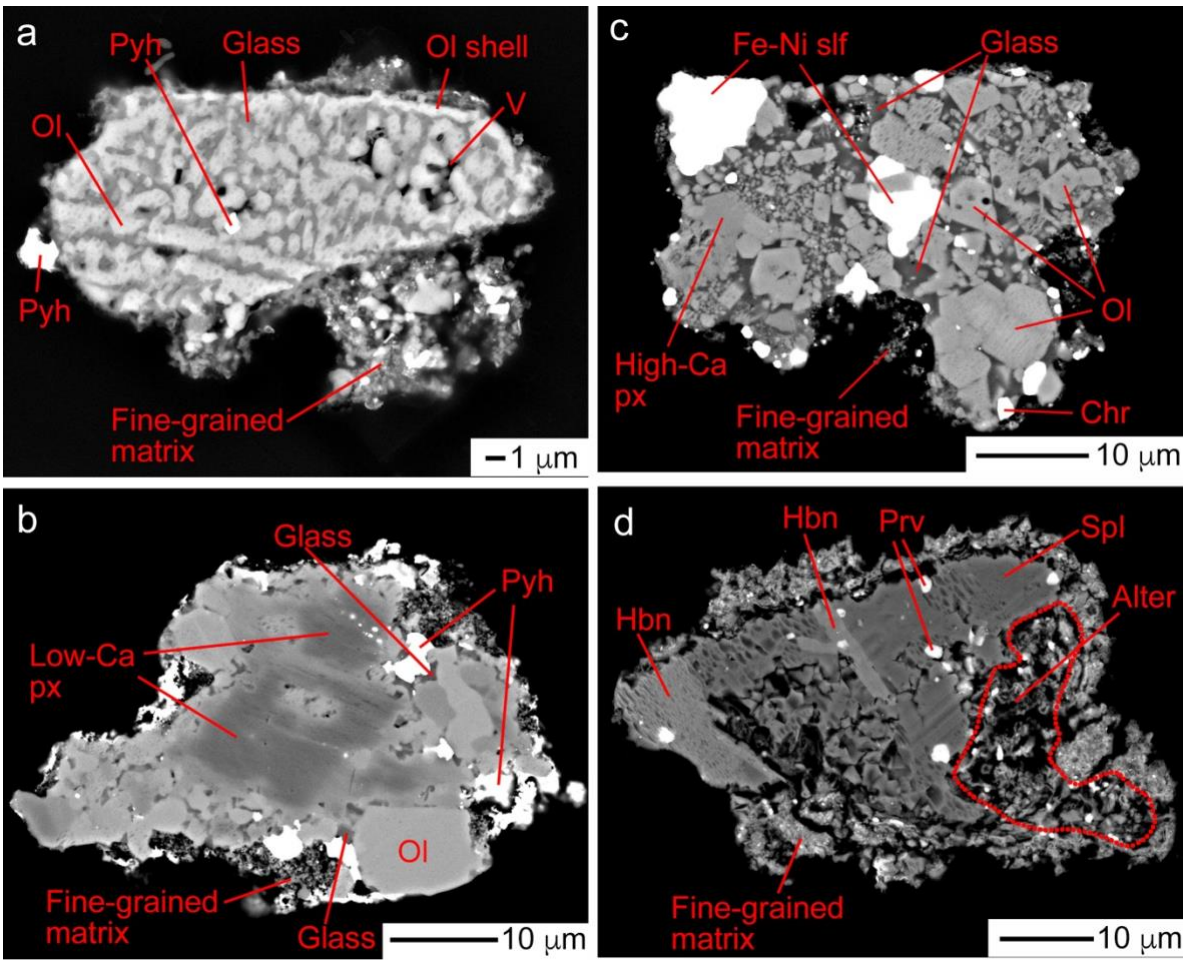
a
Pyh
Glass
Ol shell
V
Ol
Pyh
Fine-grained matrix
1 μm
c
Fe-Ni slf
Glass
Ol
High-Ca px
Fine-grained matrix
Chr
10 μm
b
Glass
Pyh
Low-Ca px
Ol
Fine-grained matrix
Glass
10 μm
d
Hbn
Prv
Spl
Alter
Hbn
Fine-grained matrix
10 μm

Figure 3

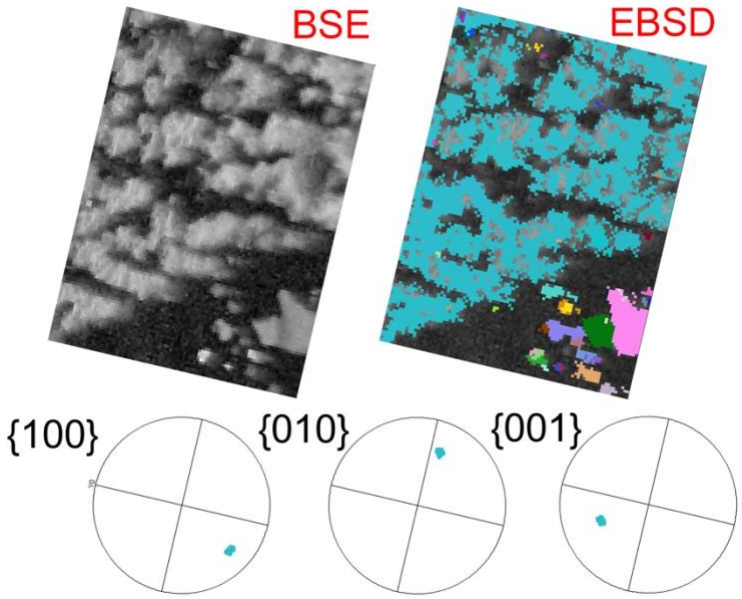

Figure 4

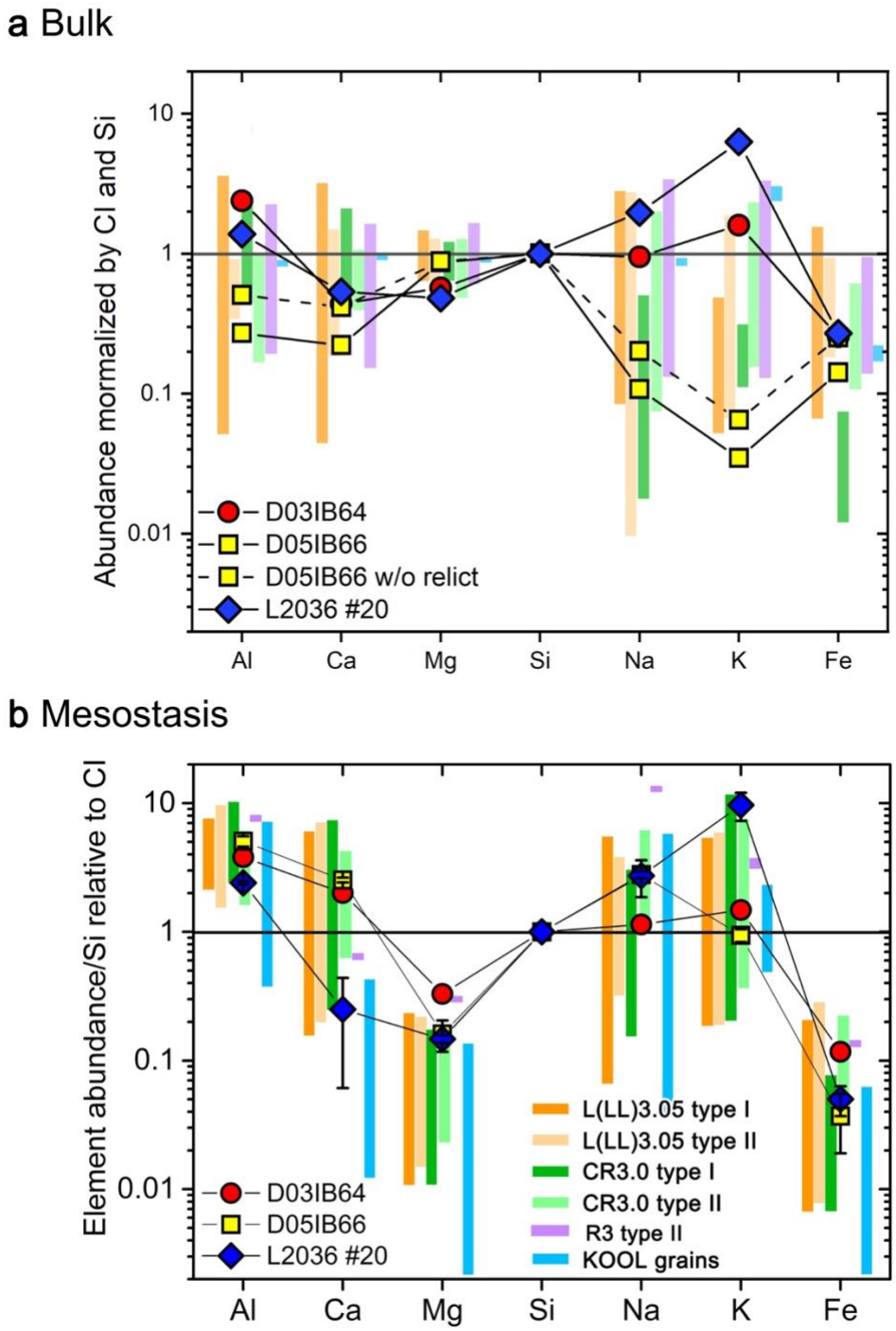
a Bulk
Abundance mormalized by CI and Si
10
1
0.1
0.01
D03IB64
D05IB66
D05IB66 w/o relict
L2036 #20
Al
Ca
Mg
Si
Na
K
Fe
b Mesostasis
Element abundance/Si relative to CI
10
1
0.1
0.01
D03IB64
D05IB66
L2036 #20
L(LL)3.05 type I
L(LL)3.05 type II
CR3.0 type I
CR3.0 type II
R3 type II
KOOL grains
Al
Ca
Mg
Si
Na
K
Fe

Figure 5

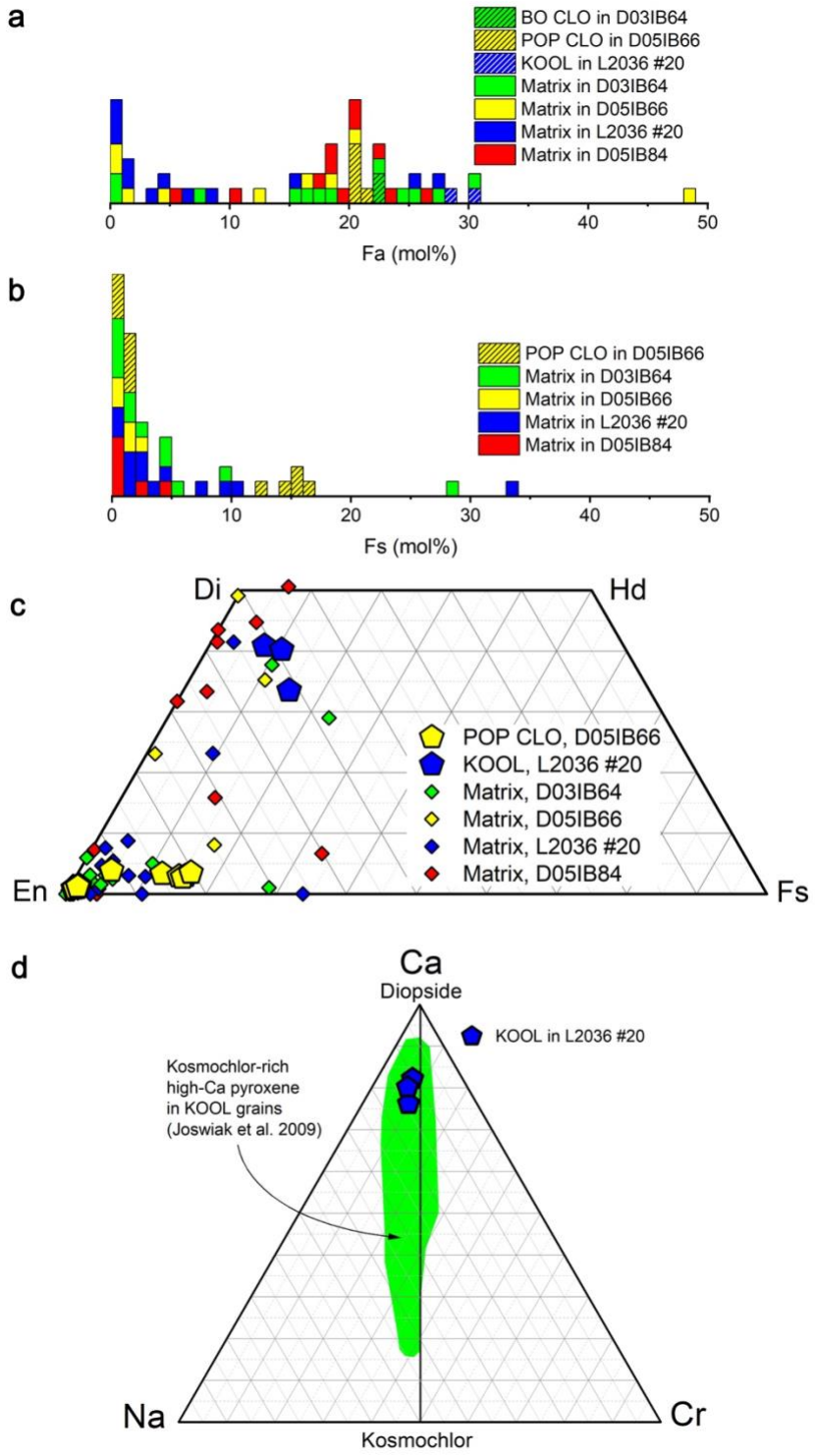
a
BO CLO in D03IB64
POP CLO in D05IB66
KOOL in L2036 #20
Matrix in D03IB64
Matrix in D05IB66
Matrix in L2036 #20
Matrix in D05IB84
0
10
20
30
40
50
Fa (mol%)
b
POP CLO in D05IB66
Matrix in D03IB64
Matrix in D05IB66
Matrix in L2036 #20
Matrix in D05IB84
0
10
20
30
40
50
Fs (mol%)
c
Di
Hd
En
Fs
POP CLO, D05IB66
KOOL, L2036 #20
Matrix, D03IB64
Matrix, D05IB66
Matrix, L2036 #20
Matrix, D05IB84
d
Ca
Diopside
KOOL in L2036 #20
Kosmochlor-rich
high-Ca pyroxene
in KOOL grains
(Joswiak et al. 2009)
Na
Cr
Kosmochlor

Figure 6

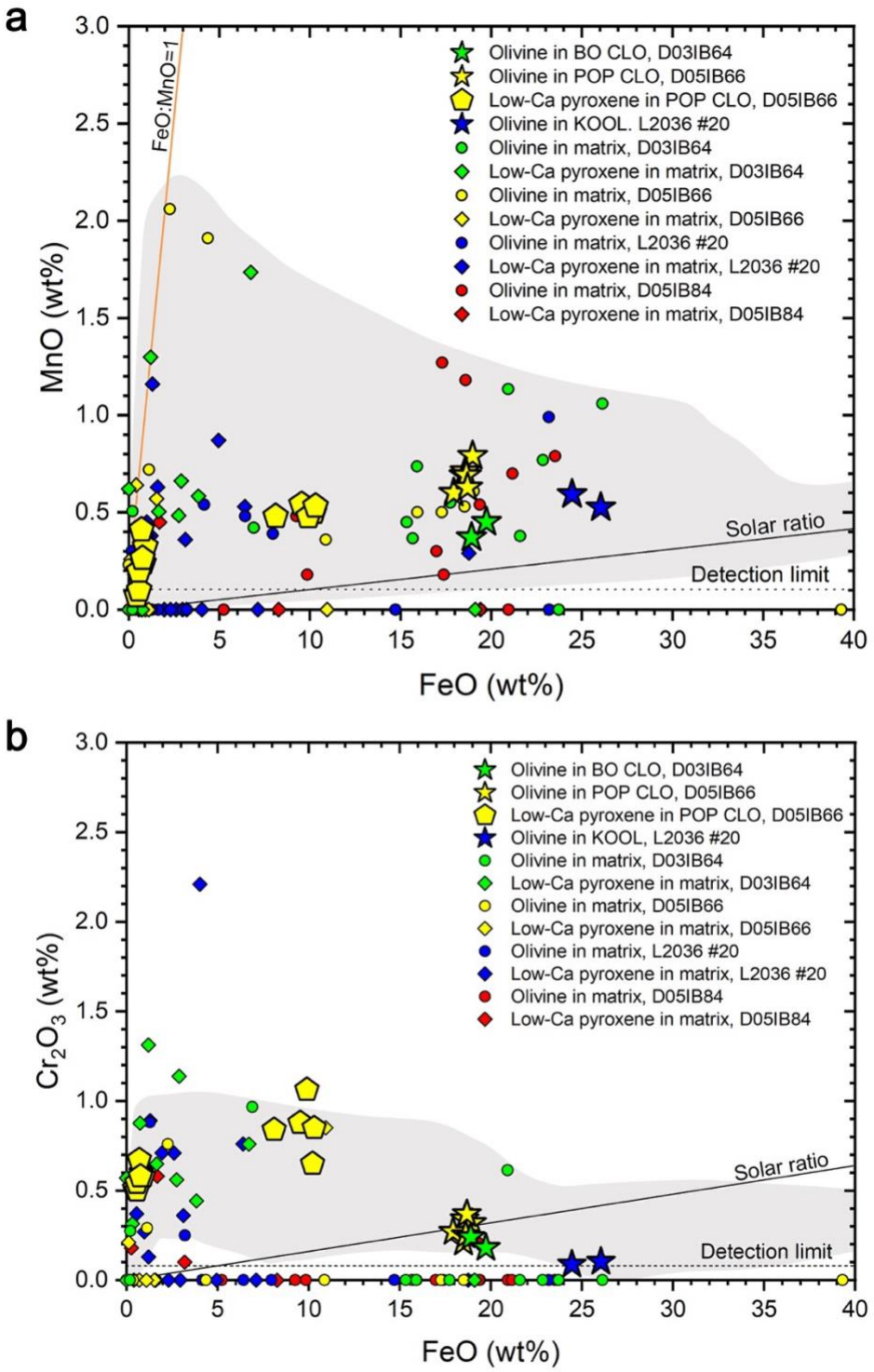
a
MnO (wt%)
FeO (wt%)
FeO:MnO=1
Solar ratio
Detection limit
Olivine in BO CLO, D03IB64
Olivine in POP CLO, D05IB66
Low-Ca pyroxene in POP CLO, D05IB66
Olivine in KOOL. L2036 #20
Olivine in matrix, D03IB64
Low-Ca pyroxene in matrix, D03IB64
Olivine in matrix, D05IB66
Low-Ca pyroxene in matrix, D05IB66
Olivine in matrix, L2036 #20
Low-Ca pyroxene in matrix, L2036 #20
Olivine in matrix, D05IB84
Low-Ca pyroxene in matrix, D05IB84
b
Cr_2O_3 (wt%)
FeO (wt%)
Solar ratio
Detection limit
Olivine in BO CLO, D03IB64
Olivine in POP CLO, D05IB66
Low-Ca pyroxene in POP CLO, D05IB66
Olivine in KOOL, L2036 #20
Olivine in matrix, D03IB64
Low-Ca pyroxene in matrix, D03IB64
Olivine in matrix, D05IB66
Low-Ca pyroxene in matrix, D05IB66
Olivine in matrix, L2036 #20
Low-Ca pyroxene in matrix, L2036 #20
Olivine in matrix, D05IB84
Low-Ca pyroxene in matrix, D05IB84

Figure 7

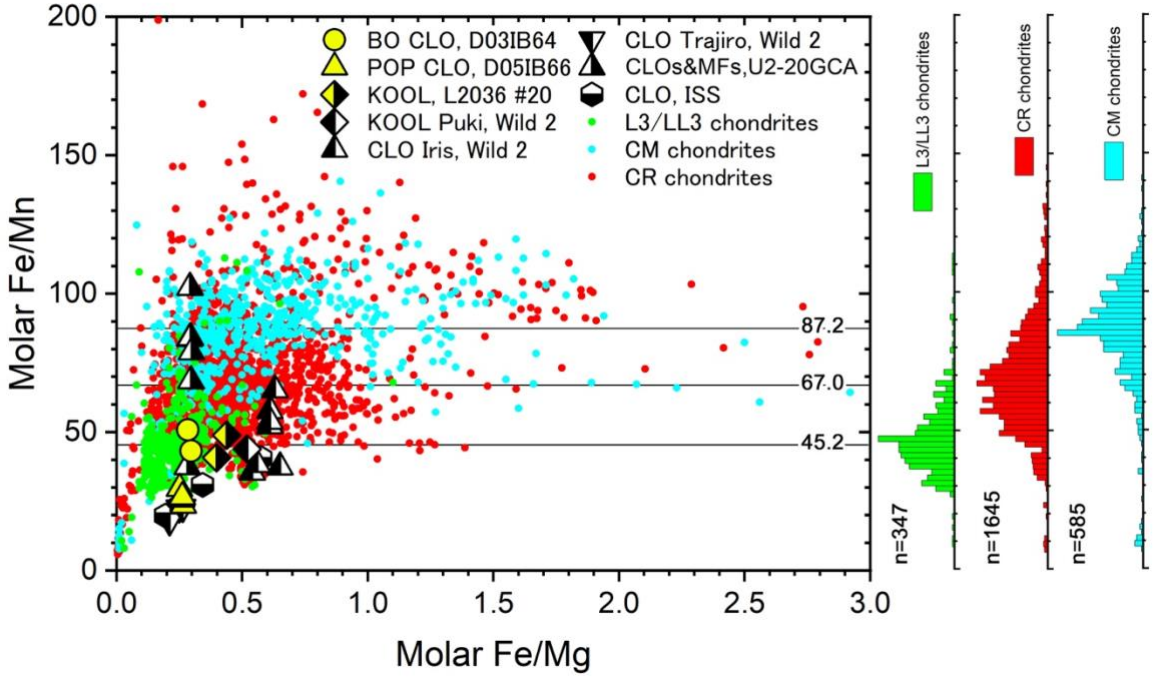
BO CLO, D03IB64
POP CLO, D05IB66
KOOL, L2036 #20
KOOL Puki, Wild 2
CLO Iris, Wild 2
CLO Trajiro, Wild 2
CLOs&MFs,U2-20GCA
CLO, ISS
L3/LL3 chondrites
CM chondrites
CR chondrites
Molar Fe/Mn
Molar Fe/Mg
87.2
67.0
45.2
n=347
n=1645
n=585

Figure 8

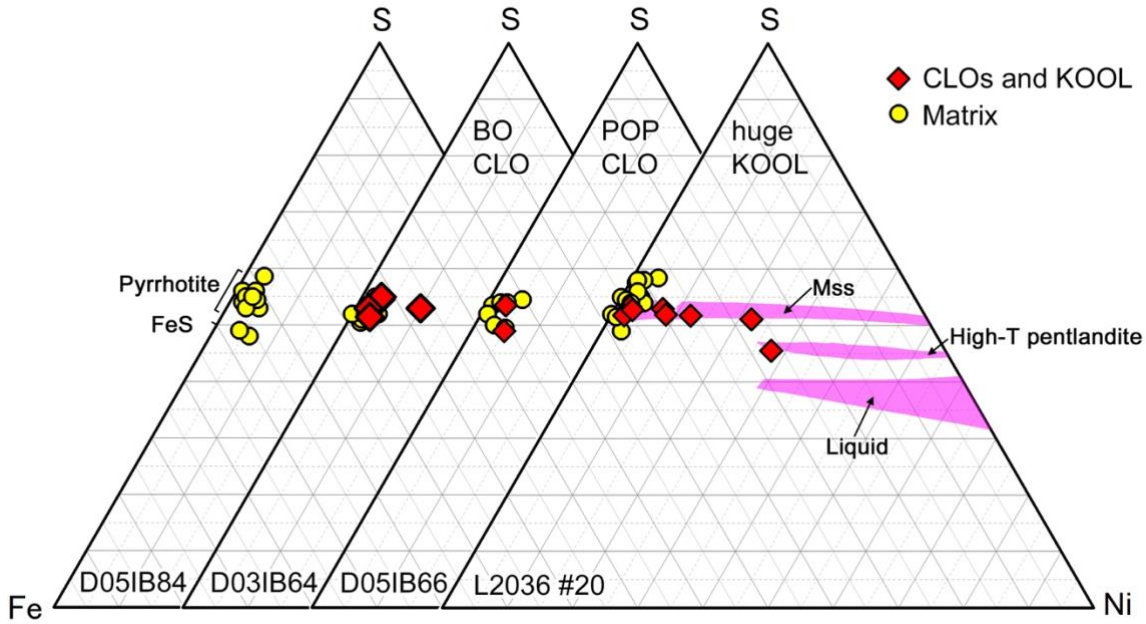
S
S
S
S
CLOs and KOOL
Matrix
BO
CLO
POP
CLO
huge
KOOL
Pyrrhotite
FeS
Mss
High-T pentlandite
Liquid
D05IB84
D03IB64
D05IB66
L2036 #20
Fe
Ni

Figure 9

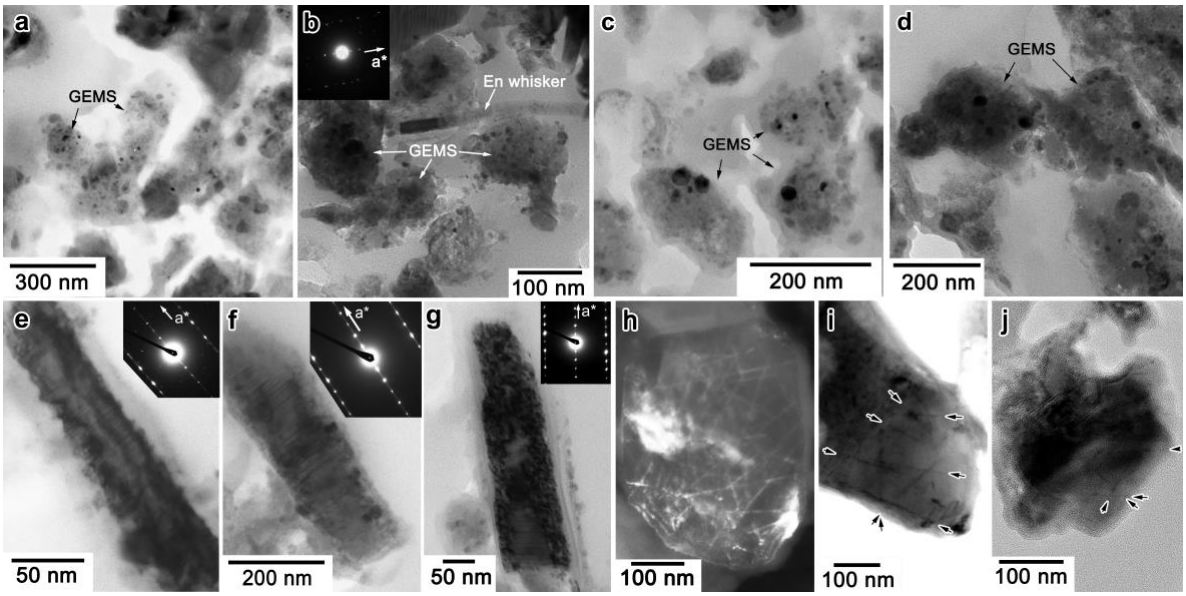
a
GEMS
300 nm
b
a*
En whisker
GEMS
100 nm
c
GEMS
200 nm
d
GEMS
200 nm
e
a*
50 nm
f
a*
200 nm
g
a*
50 nm
h
100 nm
i
100 nm
j
100 nm

Figure 10

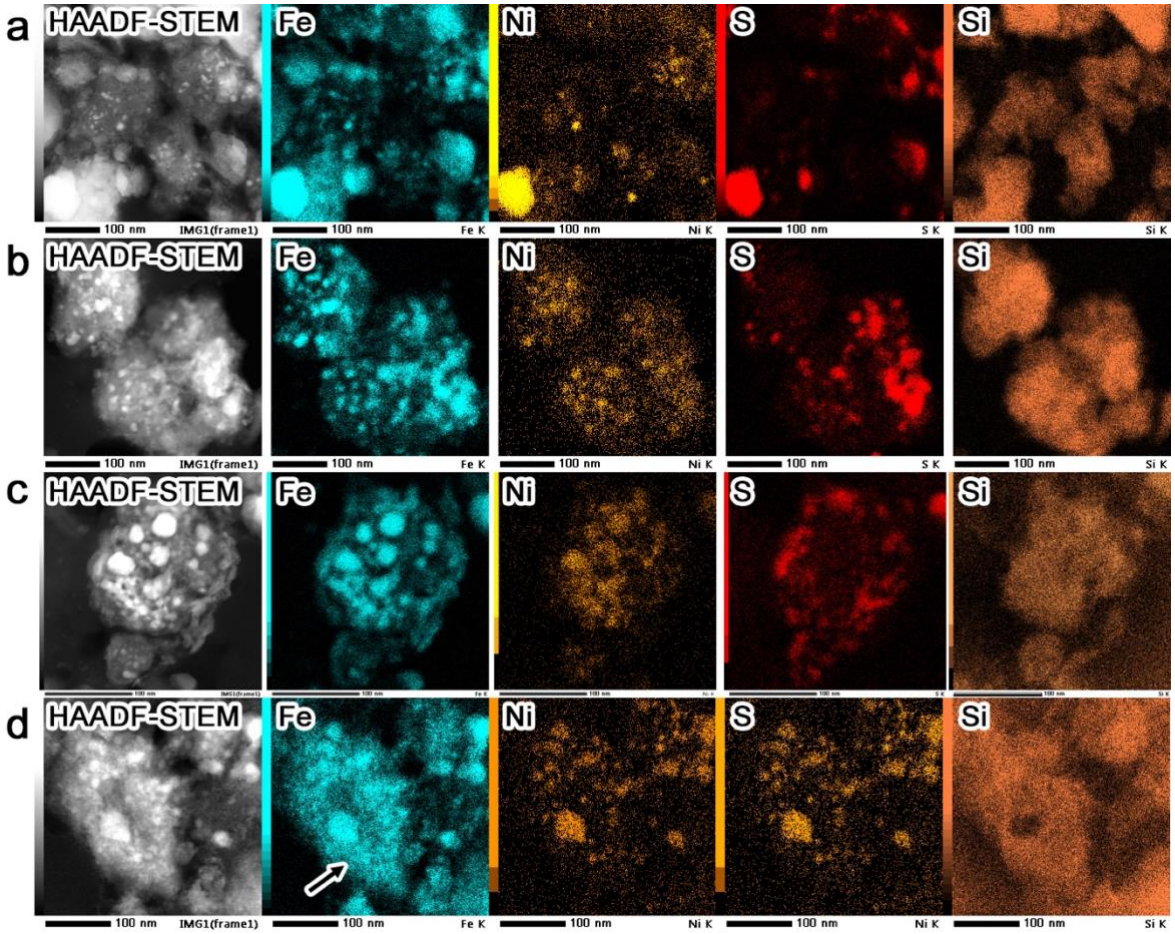

Figure 11

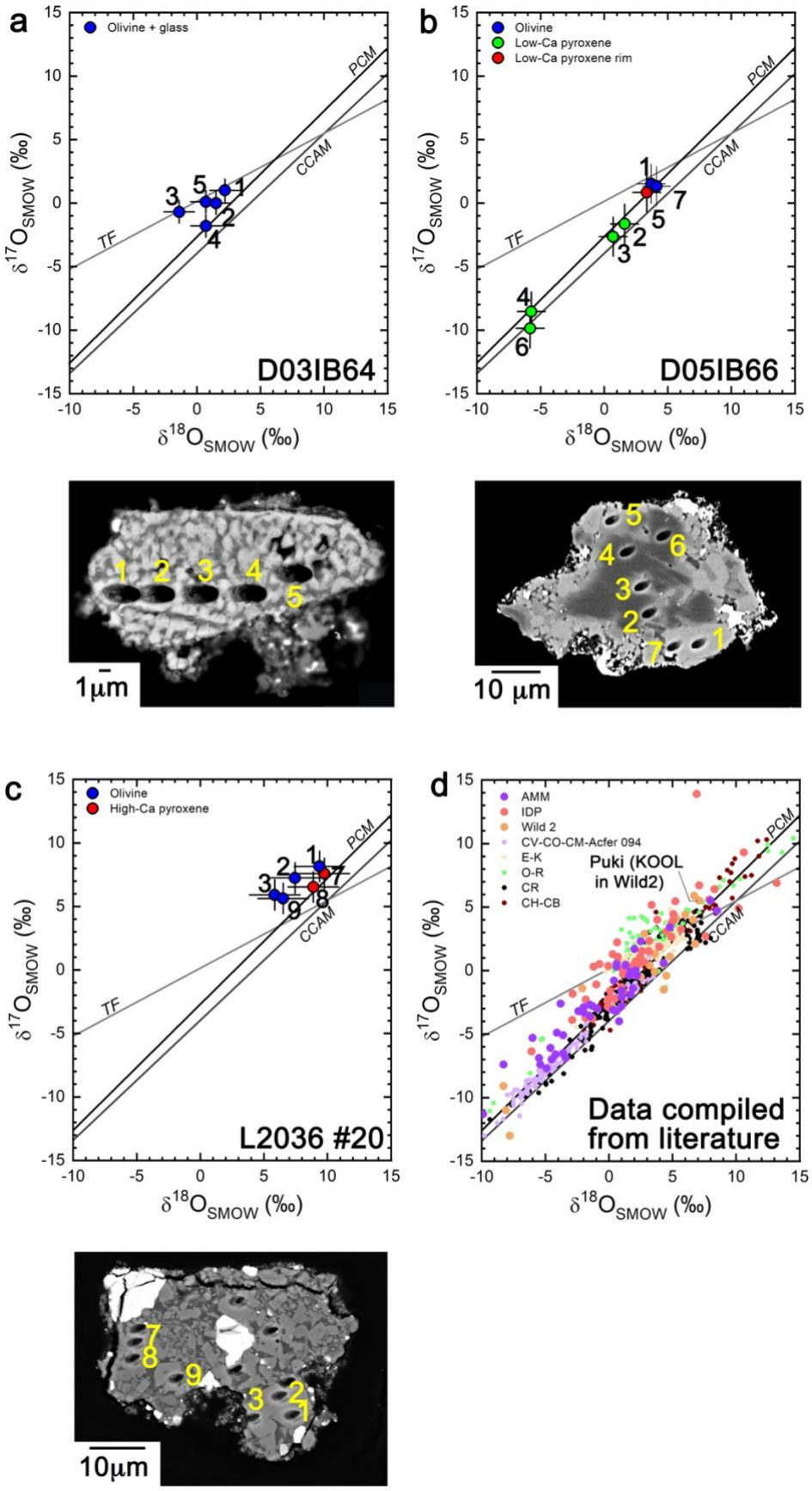

Figure 12 (Part 1)

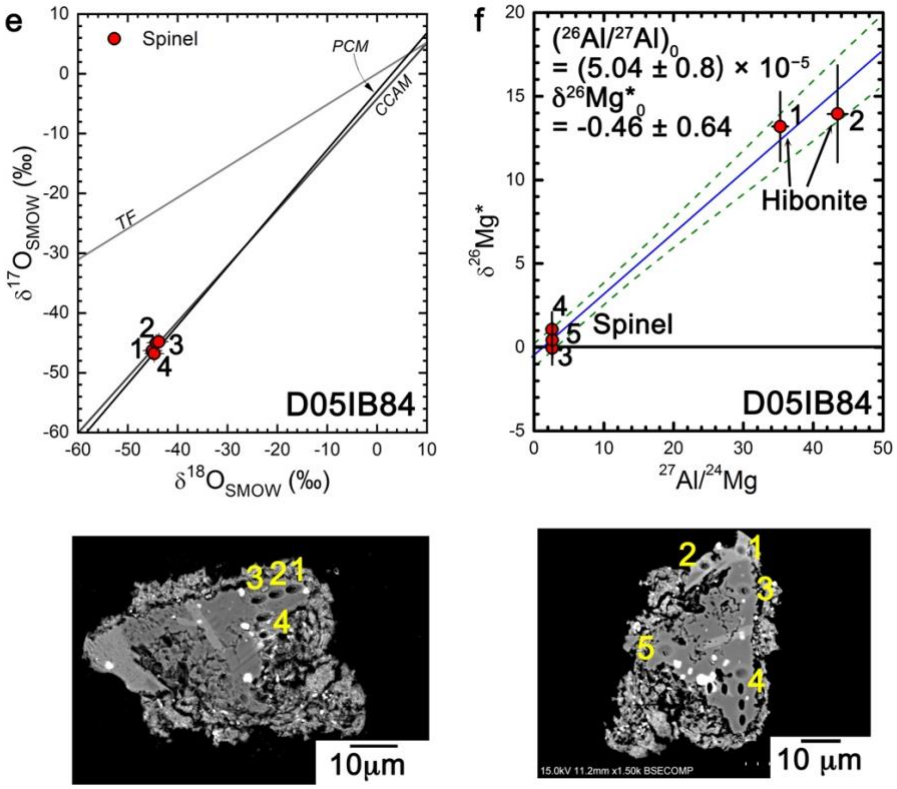
e
Spinel
PCM
CCAM
TF
D05IB84
δ17OSMOW (‰)
δ18OSMOW (‰)
f
(26Al/27Al)0
= (5.04 ± 0.8) × 10−5
δ26Mg*0
= -0.46 ± 0.64
Hibonite
Spinel
D05IB84
δ26Mg*
27Al/24Mg
10μm
10 μm

Fig. 12 (Part 2)

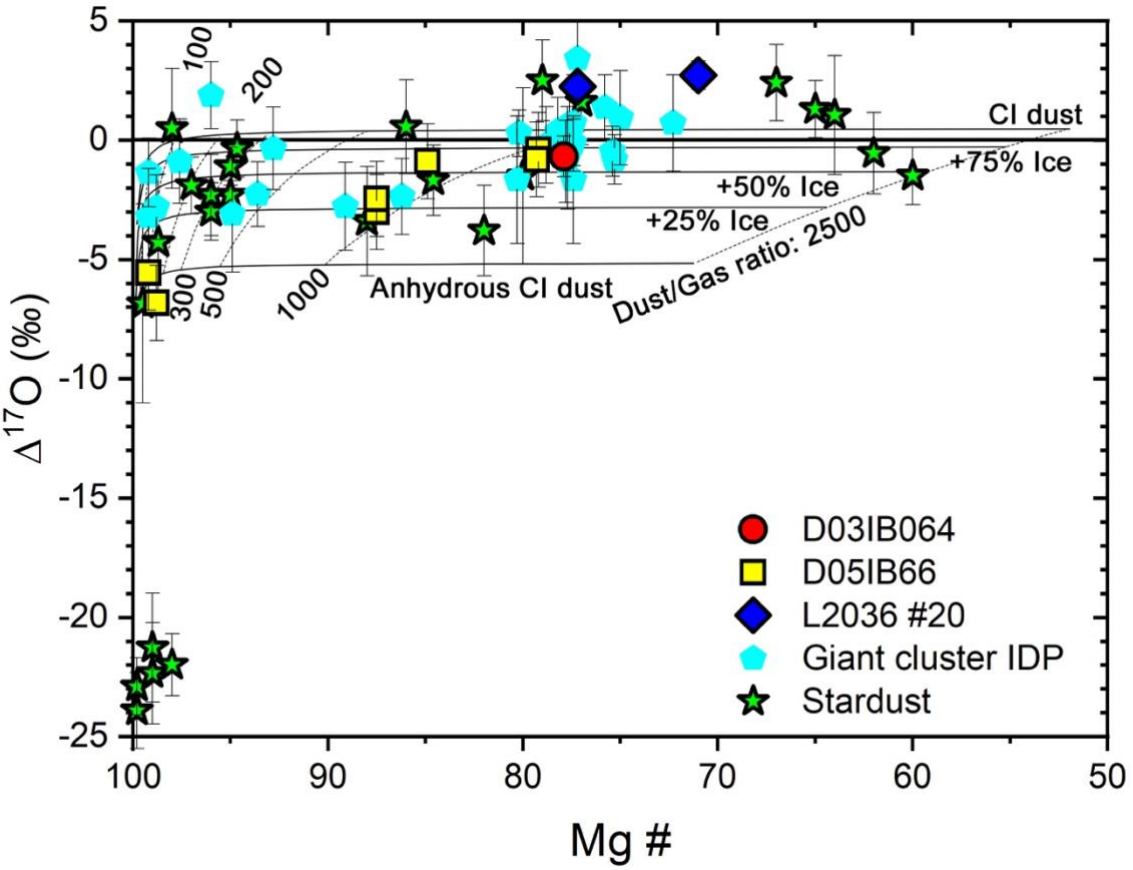
5
0
-5
-10
-15
-20
-25
100
90
80
70
60
50
Mg #
$\Delta^{17}O$ (‰)
100
200
300
500
1000
CI dust
+75% Ice
+50% Ice
+25% Ice
Anhydrous CI dust
Dust/Gas ratio: 2500
D03IB064
D05IB66
L2036 #20
Giant cluster IDP
Stardust

Figure 13

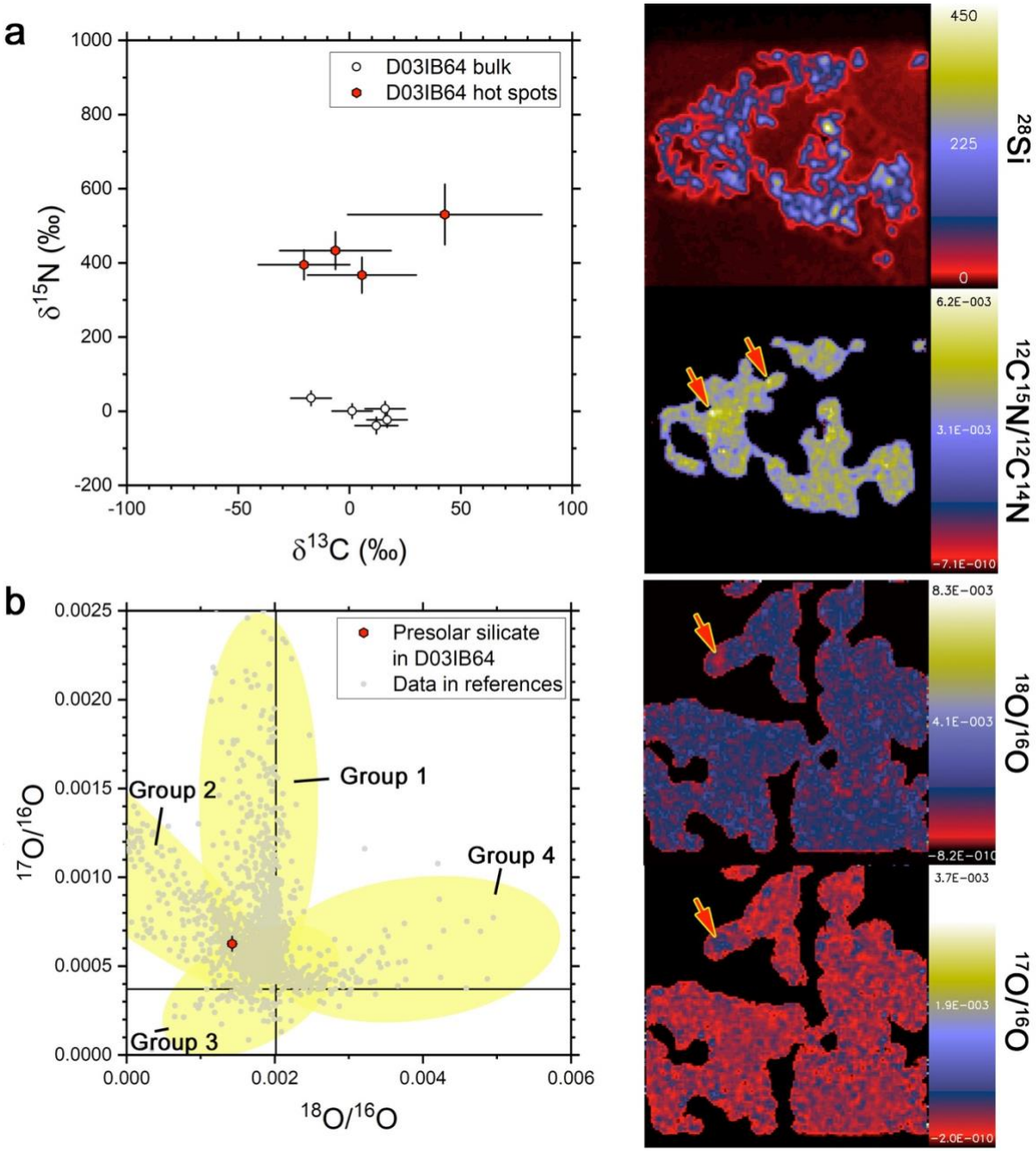
a
D03IB64 bulk
D03IB64 hot spots
δ15N (‰)
δ13C (‰)
b
Presolar silicate in D03IB64
Data in references
Group 1
Group 2
Group 3
Group 4
17O/16O
18O/16O
28Si
12C15N/12C14N
18O/16O
17O/16O

Figure 14

Supplementary material

Title

Chondrule-like objects and a Ca-Al-rich inclusion from comets or comet-like icy bodies

Authors

Takaaki Noguchi[a, *], Daisuke Nakashima[b,c], Takayuki Ushikubo[d,c], Wataru Fujiya[e], Noriaki Ohashi[f,e], John P. Bradley[g], Tomoki Nakamura[b], Noriko T. Kita[c], Peter Hoppe[h], Hidemi Ishibashi[i], Makoto Kimura[j], and Naoya Imae[j]

Affiliations

[a]Division of Earth and Planetary Science, Kyoto University, Kitashirakawaoiwake-cho, Sakyo-ku, Kyoto 606-8502, Japan

[b]Department of Earth Science, Tohoku University, 6-3 Aoba, Aramaki, Aoba-ku, Sendai 980-8578, Japan

[c]WiscSIMS, Department of Geoscience, University of Wisconsin-Madison, 1215 W Dayton St. Madison WI 53706, USA

[d]Kochi Institute for Core Sample Research, Japan Agency for Marine-Earth Science and Technology (JAMSTEC), 200 Monobe Otsu, Nankoku, Kochi 783-8502, Japan

[e]Earth Science Course, College of Science, Ibaraki University, 2-1-1 Bunkyo, Mito 310-8512, Japan

[f]NEC Networks and System Integration Corporation, Iidabashi First Tower, 2-6-1 Koraku, Bunkyo-ku, Tokyo 112-8560, Japan

[g]Hawaii Institute of Geophysics and Planetology, the University of Hawaii at Manoa, Honolulu, HI 96822, USA

[h]Particle Chemistry Department, Max Planck Institute for Chemistry, Hahn-Meitner-Weg 1, 55128 Mainz, Germany

[i]Department of Geoscience, Shizuoka University, 836, Ohya, Suruga-ku, Shizuoka 422-8529, Japan.

[j]National Institute of Polar Research, 10-3 Midori-cho, Tachikawa, Tokyo 190-8518, Japan.

Correction of the QSA effect

We suspect that a large mass-independent instrumental fractionation of the spinel standard is caused by the QSA effect (Slodzian et al., 2004) due to the high concentration of MgO (28wt.%). The QSA effect results from the simultaneous production of multiple secondary ions generated by a single primary ion, which arrive at the same time on the conversion dynode of an EM and are counted as one pulse. It is predominantly seen in the major isotope of an element with a high concentration in the target material. Therefore, the QSA effect on Mg isotopes results in count loss of the major isotope ^{24}Mg relative to the minor isotopes ^{25}Mg and ^{26}Mg (i.e., mass-independent fractionation). This results in putative, non-zero $\delta^{26}Mg^{*}$ values of the standard which are negatively biased.

The QSA effect is considered to be a function of K, the ratio of secondary ions ejected per primary ions (Slodzian et al., 2004), which is ~ 0.005 for the spinel analysis in this study, and the bias predicted for Mg isotope ratios is from ~2.5‰ to ~5‰ (= K/2 to K). This is similar to the biases observed for spinel analysis in this study. Although we kept both primary ion and secondary Mg ion intensities nearly constant over the course of analyses, the instrumental bias on the measured $\delta^{26}Mg^{*}$ values of the spinel standard was slightly more variable than analytical uncertainties. As mentioned earlier, the primary beam sizes became larger over

time and the measured $\delta^{26}Mg^{*}$ values of the spinel standard seem to correlate with the size of the primary beam. To quantify the correlation, the surface density of O^{-} primary ions (pA/μm^2) was estimated from intensities of the primary beam and surface areas of SIMS pits on the spinel standard and are compared with the corresponding $\delta^{26}Mg^{*}$ values (Fig. S1). The primary beam density varies by a factor of 3-4 and is negatively correlated with the $\delta^{26}Mg^{*}$ values, approximately by 1.5‰. Dependency of measured $\delta^{26}Mg^{*}$ values against primary beam size or density is not expected from the QSA effect. We suspect the observed correlation might be related to the size of the secondary ion spots exposed to the conversion dynode of the EM because the IMS-1280 mono-collector ion optics transfer ion images of the sample surface. When the intense secondary ions (~10^5 cps) are concentrated in a narrow region on the first dynode, this may change the pulse height distribution of the EM, though we did not identify any obvious differences. The $\delta^{26}Mg^{*}$ bias values for three individual spots in the spinel of CAI were calculated using the regression line between the $\delta^{26}Mg^{*}$ bias and surface density of O^{-} primary ions in Fig. S1 and were corrected for unknown samples (Table 2). The uncertainty associated with the corrected values was inferred from 2σ confidence lines accompanying the regression line (Fig. S1) and was propagated as uncertainty to those of $\delta^{26}Mg^{*}$ values of individual unknown sample analyses (Table 2).

Supplementary Tables

Table S1 Detailed data table of the Mg isotope analyses of spinel and hibonite on spinel and hibonite standards and D05IB84

				Raw data																			Bias-corrected data			
	Analysis number	Target	Remarks	^{24}Mg (cps)	δ^{25}Mg/^{24}Mg ± 2SE (‰)		δ^{26}Mg/^{24}Mg ± 2SE (‰)		δ^{26}Mg/^{25}Mg ± 2SE (‰)		^{27}Al/^{24}Mg	2SE (%)	δ^{26}Mg* ± 2SE (‰)		Ip-start (pA)[a]	Ip-end (pA)[b]	Ip-avr (pA)[c]	Pit size (μm^2)[d]	Density of primary beam (pA/μm^2)	Cor-δ^{26}Mg* ± 2SE (‰)[e]		**^{27}Al/^{24}Mg**	**2SE (%)**	**δ^{26}Mg* ± 2s (‰)**	
Spinel	20130801_1	FIB square		6.26E+04	-0.16	0.81	-5.18	1.06	-5.02	0.99	2.24	0.14	-4.83	1.42	3.21	3.37	3.29	4.88	0.67						
	20130801_7	FIB square		9.13E+04	-1.14	0.71	-5.91	0.73	-4.77	0.69	2.25	0.27	-3.66	1.16	4.20	4.64	4.42	21.80	0.20						
	20130801_12	FIB square		8.98E+04	1.96	1.11	-2.31	1.34	-4.24	1.15	2.25	0.29	-6.01	1.75	3.90	3.57	3.74	6.26	0.60						
	20130801_14	C-coated area		8.41E+04	-1.28	0.82	-7.03	0.93	-5.74	0.81	2.28	0.15	-4.49	1.30	3.85	4.70	4.27	7.74	0.55						
	20130801_17	SHIB Spinel 3		9.62E+04	0.08	0.52	-3.72	0.72	-3.80	0.62	2.24	0.17	-3.86	0.87	3.82	4.50	4.16	14.09	0.30	-3.80	0.49	**2.61**	**0.03**	**-0.05**	**1.00**
	20130801_18	SHIB Spinel 4		1.04E+05	-0.93	0.51	-4.49	0.61	-3.56	0.59	2.21	0.20	-2.66	0.90	3.99	4.67	4.33	15.83	0.27	-3.73	0.50	**2.58**	**0.03**	**1.07**	**1.03**
	20130801_19	SHIB Spinel 5		9.54E+04	-0.24	0.57	-3.67	0.68	-3.42	0.60	2.25	0.15	-3.17	0.92	3.94	4.47	4.21	17.95	0.23	-3.60	0.53	**2.62**	**0.03**	**0.42**	**1.06**
	20130801_21	C-coated area		8.43E+04	-2.20	0.66	-7.00	0.89	-4.81	0.68	2.31	0.24	-2.71	0.98	3.80	4.48	4.14	19.10	0.22						
	20130801_24	C-coated area		7.50E+04	-1.75	0.68	-7.45	0.84	-5.71	0.69	2.31	0.30	-4.03	1.05	3.80	4.11	3.96	26.71	0.15						
	Average std ± 2SD (n = 6)										**2.28**	**0.06**													
	RSF										**0.86**	**0.02**													
Hibonite	20130801_2+3	FIB square	Combined spots 2 & 3	1.03E+04	0.77	0.99	1.06	1.19	0.33	1.25	23.21	0.14	-0.29	1.87											
	20130801_13	FIB square	New 20 um aperture	1.17E+04	1.08	0.99	0.79	1.10	-0.25	1.10	23.56	0.15	-1.17	1.74											
	20130801_15	SHIB Hibonite 1		8.52E+03	-1.79	1.14	9.47	1.20	11.34	1.27	26.38	0.21	13.20	2.07								**35.35**	**1.15**	**13.20**	**2.07**
	20130801_16	SHIB Hibonite 2	142 cycles	7.92E+03	-0.89	1.62	12.01	1.61	12.96	1.72	32.45	0.71	13.95	2.90								**43.49**	**1.45**	**13.95**	**2.90**
	20130801_20	C-coated area		1.15E+04	-1.22	0.85	-2.21	1.00	-0.97	0.95	23.64	0.32	0.25	1.47											
	20130801_22	C-coated area		1.13E+04	-0.67	1.07	-1.16	1.19	-0.44	1.19	23.73	0.40	0.31	1.87											
	20130801_23	FIB square		9.06E+03	0.15	1.05	0.19	1.15	0.09	1.18	24.21	0.33	0.06	1.87											
	20130801_25	C-coated area		1.12E+04	-0.40	1.00	-2.09	1.20	-1.66	1.18	23.99	0.46	-1.19	1.77											
	Average std ± 2SD (n = 6)										**23.72**	**0.70**	**-0.34**	**1.37**											
	RSF (Calibratuion of 27Al/24Mg ratio is uncertain by at least 1% from EPMA analyses)										**0.75**	**0.02**													

[a] O^- primary beam intensity just before spot analysis

[b] O^- primary beam intensity just after spot analysis

[c] Average of O^- primary beam intensity before/after spot analysis

[d] Surface area of SIMS pit estimated using SEM images

[e] δ^{26}Mg* value for instrumental bias (QSA effect) correction

Table S2. Modal abundances of silicates and oxide.

Name	Type	Olivine	Low-Ca pyroxene	High-Ca pyroxene	Glass	Chromite
D03IB64	BO-like CLO	0.67			0.33	
D05IB66	POP CLO including relict low-Ca pyroxene	0.26	0.70		0.04	
D05IB66	POP CLO excluding relict low-Ca pyroxene	0.45	0.48		0.07	
L2036#20	KOOL grain	0.48		0.05	0.47	
Torajiro	PO CLO	0.36	0.52		0.06	0.06

CLO: chondrule-like object

Table S3. 100% normalized calculated bulk chemical compositions for cyrstallization calculation using MELTS.

Name	D03IB64	D05IB66	L2036#20	Trajiro	Iris
Type	BO-ilke CLO	POP-like CLO excluding relict low-Ca pyroxene	KOOL grain	PO CLO	PO CLO
SiO_2	51.92	57.47	53.89	60.02	42.32
TiO_2	b. d.	b. d.	b. d.	b. d.	0.10
Al_2O_3	8.94	22.34	5.36	19.11	6.83
Cr_2O_3	b. d.	b. d.	0.16	0.48	3.00
V_2O_3	b. d.	b. d.	b. d.	b. d.	0.03
FeO	14.25	1.50	15.64	2.25	23.01
MnO	b. d.	b. d.	b. d.	b. d.	0.33
MgO	21.76	5.50	19.18	0.38	20.74
CaO	1.30	8.54	1.64	7.44	1.58
Na_2O	1.45	4.51	3.12	4.04	2.03
K_2O	0.38	0.15	1.01	6.29	0.04

Data sources: Torajoro from Nakamura et al. (2008) and Iris from Gainsforth et al. (2015)
CLO: chondrule-like object
b. d.: below detection limit

Supplementary Figures

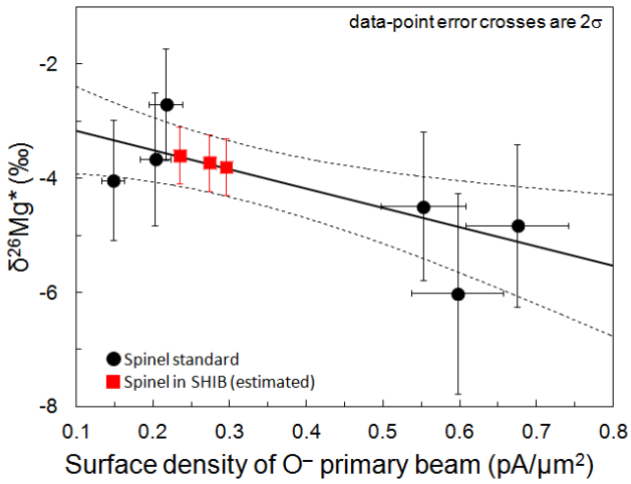

Figure S1 Comparison between $\delta^{26}Mg^{*}$ values and surface density of O^{-} primary beam on the spinel standard. The solid line represents the regression line, and the dashed lines represent the 2σ confidence lines. The $\delta^{26}Mg^{*}$ bias values for the three spots on the spinel of the CAI (SHIB: spinel-hibonite-perovskite inclusion), which are estimated using the regression line and surface density of O^{-} primary beam, are plotted as red squares.

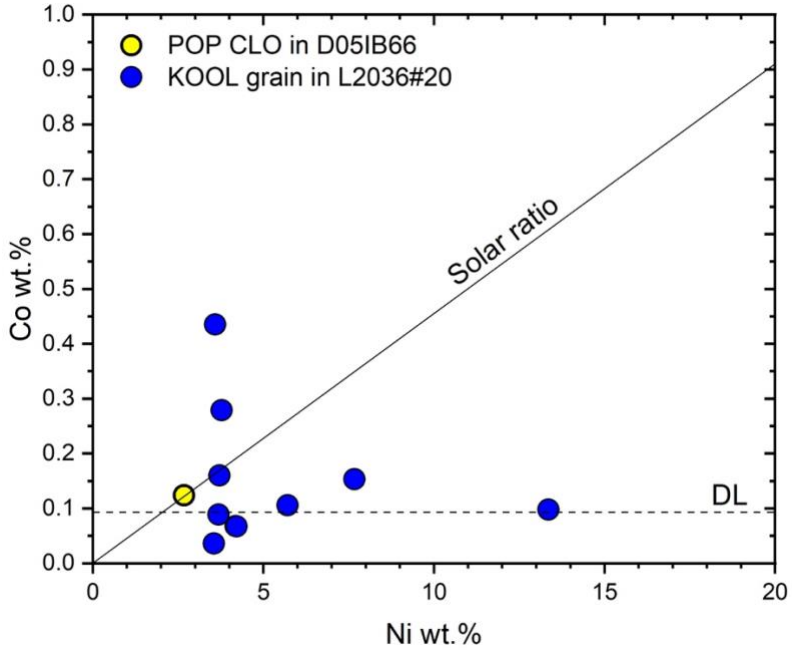

Figure S2 Ni and Co contents in sulfide in the POP chondrule-like object (CLO) and the KOOL grain. Chemical compositions were measured using field-emission electron microprobe analyzer (FE-EPMA). DL: detection limit.

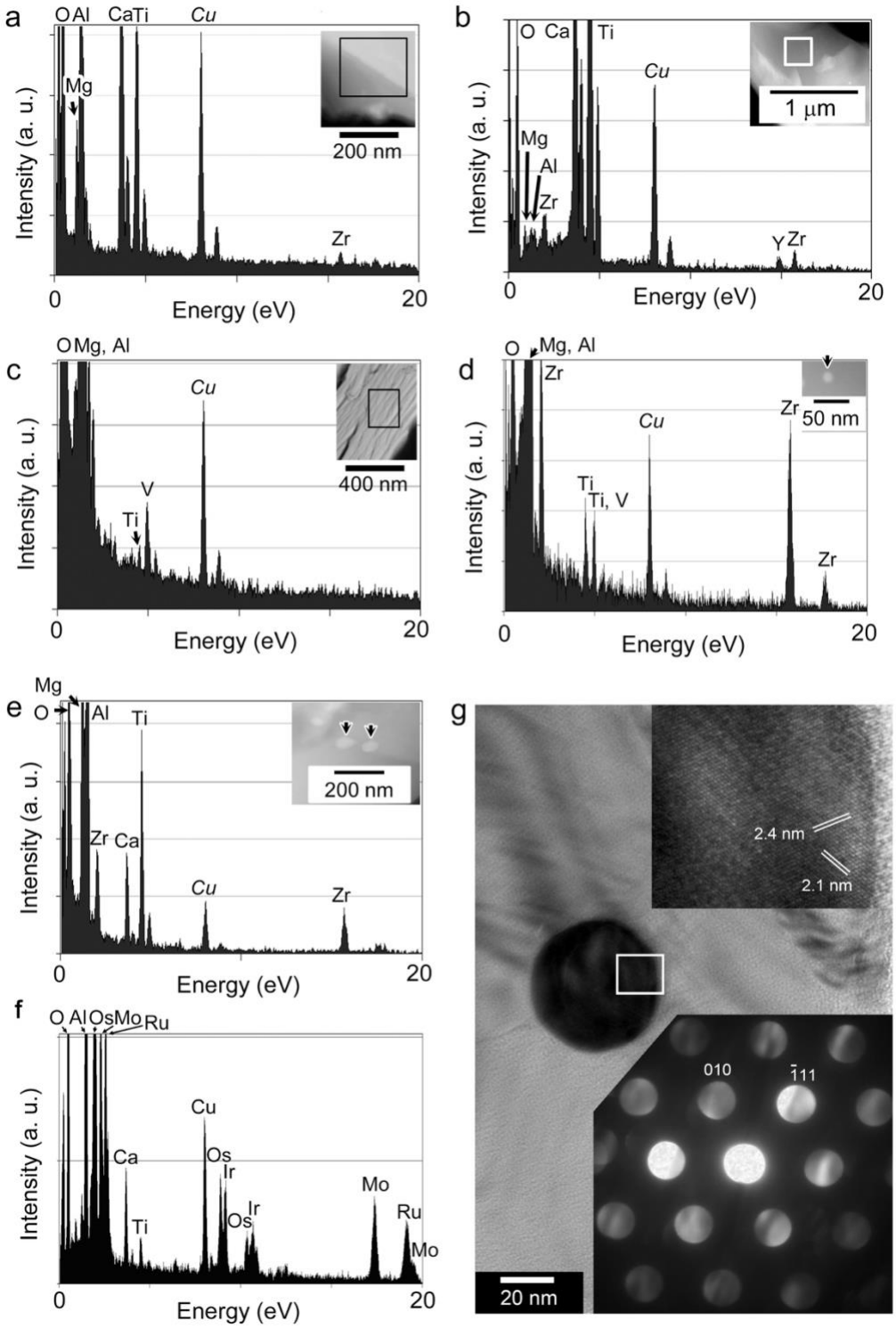

Figure S3 Ultra-refractory signatures of the SHIB fragment in D05IB84. (a) The EDS

spectrum of hibonite and a HAADF-STEM image showing an analyzed area as an open rectangle. The EDS spectra show it contains Zr. (b) The EDS spectrum of perovskite and a HAADF-STEM image showing an analyzed area as an open rectangle. The EDS spectra show it contains Zr and Y. (c) The EDS spectrum of spinel and a HAADF-STEM image showing an analyzed area as an open rectangle. The EDS spectrum shows it contains V. (d) The EDS spectrum of an inclusion in spinel and a HAADF-STEM image indicating the inclusion by an arrow. The EDS spectrum suggests that the inclusion is Ti-bearing Zr oxide. (e) The EDS spectrum of inclusions in perovskite and a HAADF-STEM image indicating the inclusions by arrows. The EDS spectrum of one of the inclusions suggests that the inclusion is Zr-bearing Ti oxide. (f) and (g) A refractory metal nugget (RMN) composed of Os, Ir, Mo, and Ru in hibonite. Oxygen, Mg, Al, Ca, and Ti in (f) are from embedding spinel and neighbor perovskite crystal and Cu from the TEM grid. The upper inset in (g) shows the lattice fringes of this RMN. The lower inset in (g) shows the nanobeam electron diffraction pattern. These two insets were taken from the same crystallographic direction.

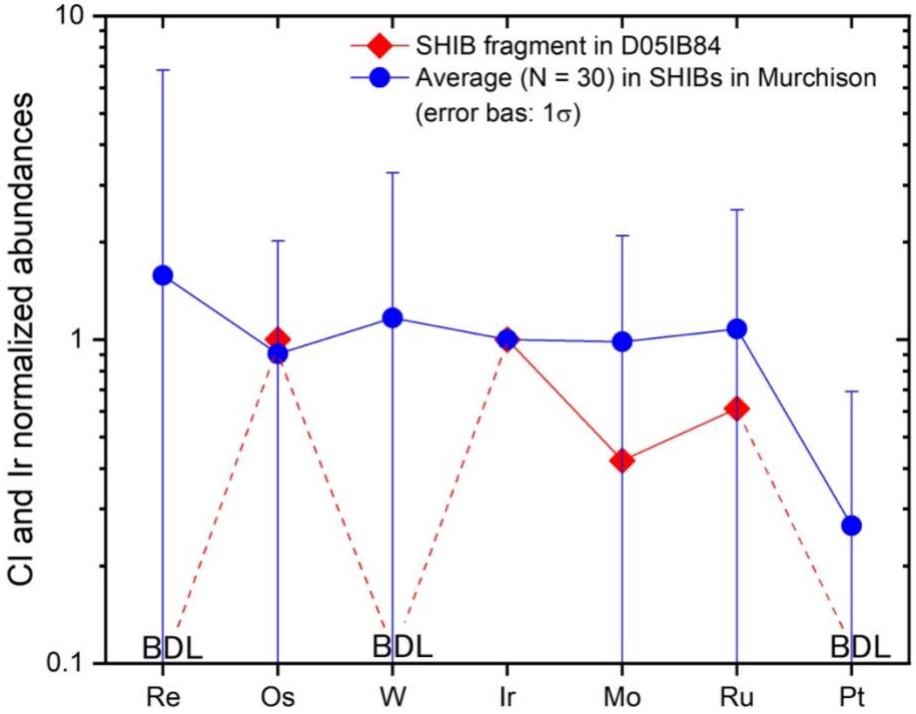

Figure S4 The CI and Ir normalized elemental abundances in an RMN in the SHIB fragment. The CI and Ir normalized average elemental abundances in 30 RMNs in SHIBs in Murchison (Schwanger et al., 2015) are also plotted for comparison.

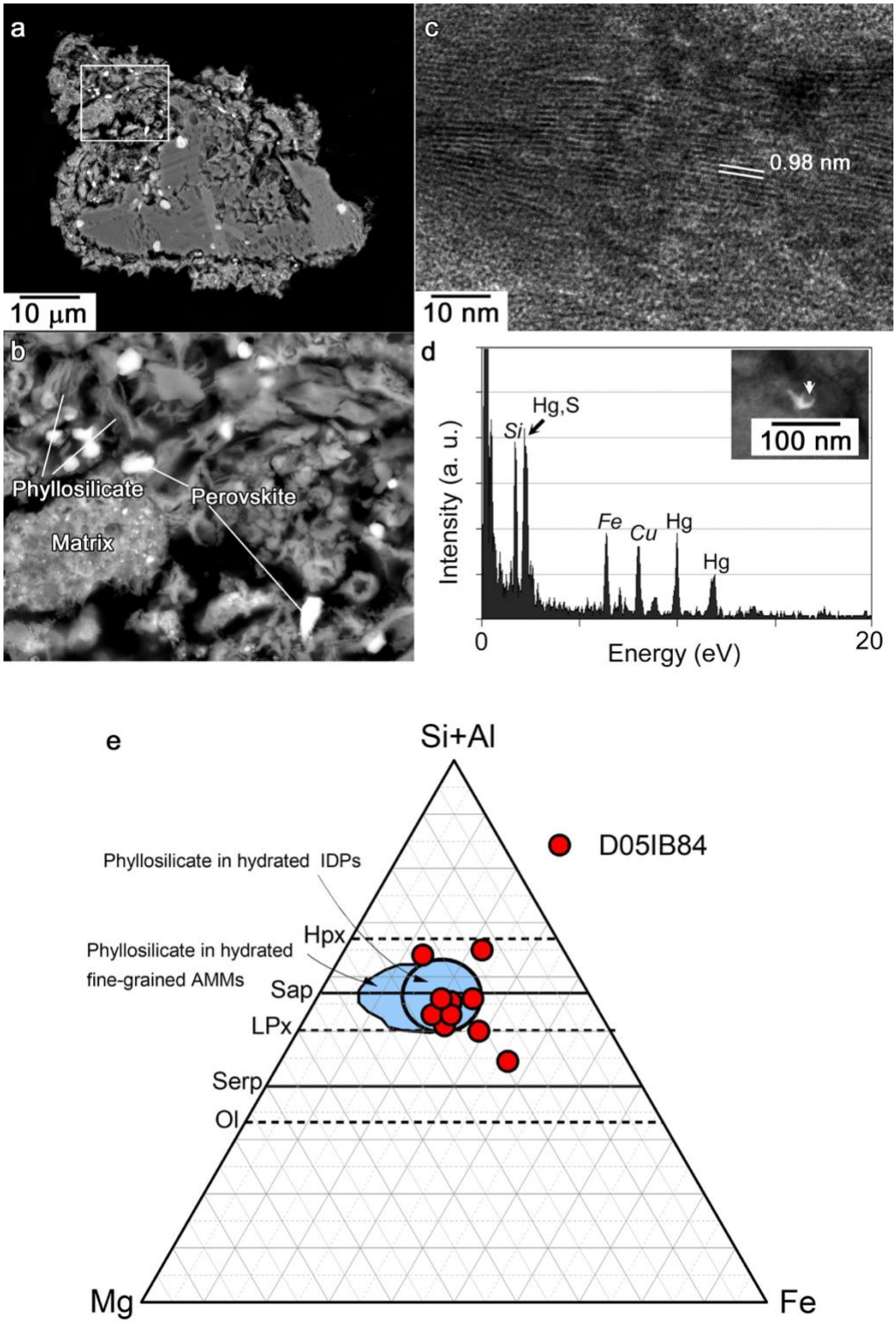

Figure S5 Phyllosilicate on the periphery of the SHIB fragment in AMM D05IB84. (a)

Backscattered electron (BSE) image of the rim of the SHIB fragment. (b) An enlarged BSE image at the rim of the CAI. Its rim was replaced by fibrous phyllosilicate, and perovskite crystals survived aqueous alteration. The enlarged area is indicated by an open rectangle in (a). (c) Lattice fringes of phyllosilicate in the rim of the SHIB fragment. 0.98 nm-wide lattice fringes indicate that this AMM experienced moderate heating during atmospheric entry. (d) HAADF-STEM image of a small (~100 nm across) HgS grain in the matrix and its EDS spectra. (e) Chemical compositions of phyllosilicate in the rim of the SHIB grain. Compositional fields of phyllosilicate in IDPs and hydrated fine-grained AMMs are from Nakamura et al. (2004), Noguchi et al. (2002), and Sakamoto et al. (2010), respectively.

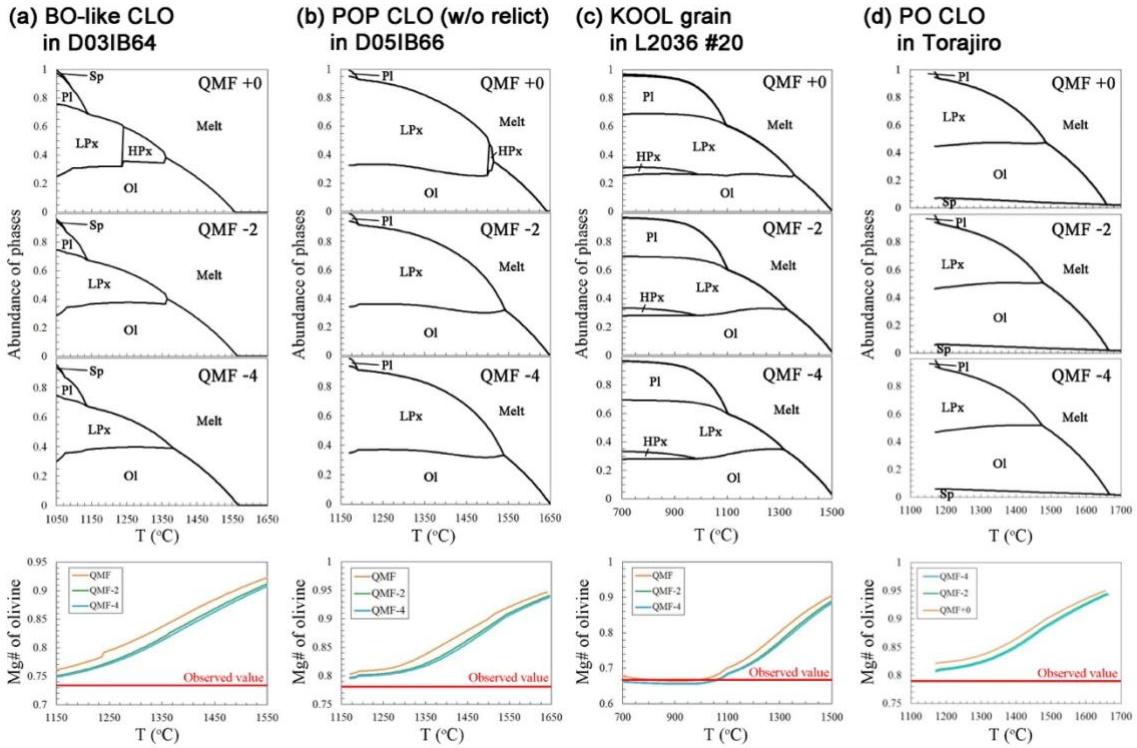

Figure S6 Equilibrium crystallization sequences of two CLOs and the KOOL grain. Phase abundances and Mg# of olivine in these objects were calculated using MELTS for three different oxygen fugacities of QMF ±0, QMF–2, and QMF–4. For comparison, equilibrium crystallization sequences of the PO CLO Trajiro were also calculated based on the data by Nakamura et al. (2008).

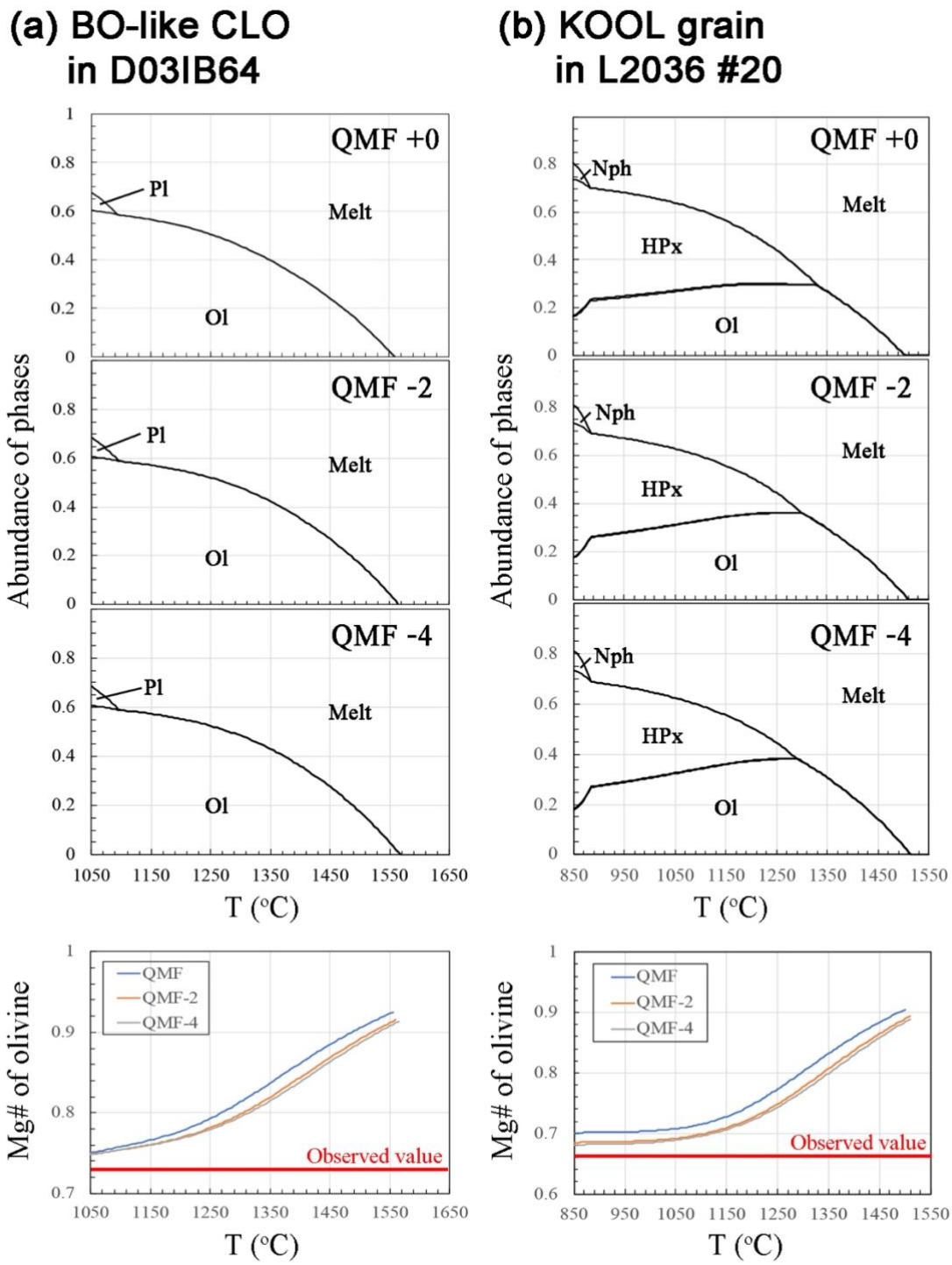

Figure S7 Crystallization sequences of the BO-like CLO and the KOOL grain. (a) The

crystallization process of the BO-like CLO with suppressed crystallization of low-Ca and high-Ca pyroxenes and plagioclase. (b) The crystallization process of the KOOL grain with suppressed crystallization of low-Ca pyroxene and plagioclase. These objects ' phase abundances and Mg# of olivine were calculated using MELTS for three different oxygen fugacities of QMF ±0, QMF–2, and QMF–4.

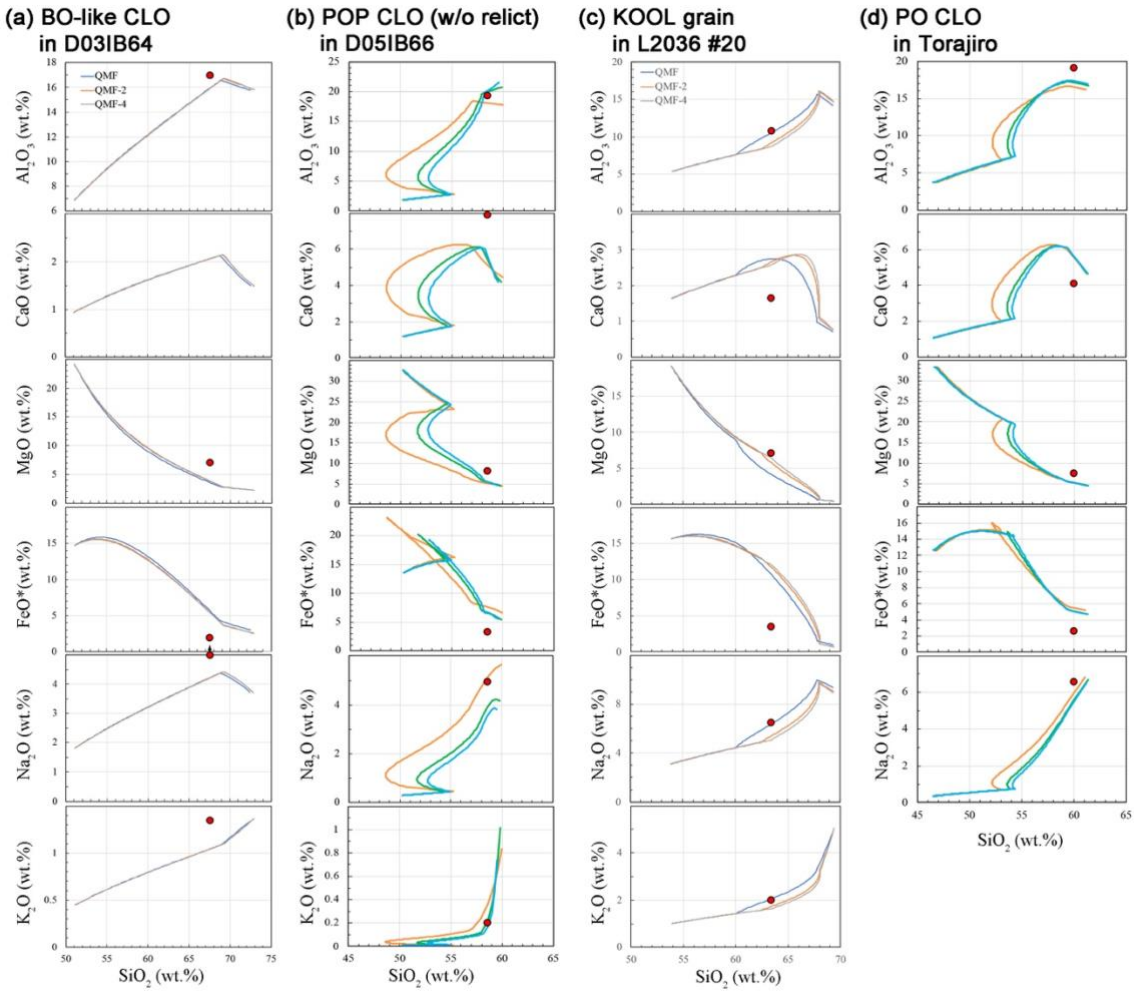

Figure S8 Trends of chemical compositions of melt in the two CLOs, the KOOL grain, and the CLO Trajiro, during crystallization. They were calculated using MELTS for three different oxygen fugacities of QMF ±0, QMF–2, and QMF–4. Crystallization of low-Ca and high-Ca pyroxenes and plagioclase was suppressed in (a), and crystallization of low-Ca pyroxene and plagioclase was suppressed in (b). Red circles represent the actual chemical composition of glass.